{FeST}
Hydrological Model

Reference Manual

Department of Civil and Environmental Engineering
Water Sciences and Engineering Division

POLITECNICO
MILANO 1863

September, 2023

Revision sheet

Release No.	Date	Revision Description
Rev. 0	1st/May/2023	FEST Reference original document

Table of contents

TABLE OF CONTENTS I

LIST OF FIGURES III

LIST OF BOXES VII

LIST OF TABLES VIII

INTRODUCTION 1

CHAPTER 1 FEST MODEL SCHEME 2

CHAPTER 2 METEOROLOGICAL DATA 5

- 2.1 SPATIAL INTERPOLATION METHODS 5
  - *2.1.1 Thiessen polygons* 5
  - *2.1.2 Inverse distance weighting* 6
  - *2.1.3 Kriging (ordinary)* 8
- 2.2 NET RADIATION OVER COMPLEX TOPOGRAPHY 17
  - *2.2.1 Shortwave radiation* 18
  - *2.2.2 Longwave radiation* 26
- 2.3 AIR TEMPERATURE WITH LAPSE RATE 27
- 2.4 PRECIPITATION WITH LAPSE RATE 32
- 2.5 WIND SPEED OVER COMPLEX TOPOGRAPHY 32
  - *2.5.1 The MicroMet model* 34
  - *2.5.2 The González-Longatt model* 38
- 2.6 MIXING METHODS 40
- 2.7 GRIDDED METEOROLOGICAL DATA 42

CHAPTER 3 CANOPY INTERCEPTION 45

CHAPTER 4 SNOW ACCUMULATION AND MELTING 47

CHAPTER 5 GLACIER ACCUMULATION AND ABLATION 51

CHAPTER 6 INFILTRATION AND RUNOFF 55

6.1 THE SCS CURVE NUMBER 57
6.2 PHILIP 60
6.3 GREEN AND AMPT 62

CHAPTER 7 EVAPOTRANSPIRATION 69

7.1 POTENTIAL EVAPOTRANSPIRATION 70
7.1.1 Hargreaves-Samani 72
7.1.2 Hargreaves-Samani-Ravazzani 73
7.1.3 Penman and Penman-Monteith 73
7.1.4 FAO Penman-Monteith 76
7.1.5 Priestley-Taylor 77
7.2 ACTUAL EVAPOTRANSPIRATION FROM POTENTIAL ONE 78
7.3 ACTUAL EVAPOTRANSPIRATION FROM THE ENERGY BALANCE 78

CHAPTER 8 SOIL WATER BALANCE 79

8.1 CELL ON HILLSLOPE 80
8.2 CELL IN LAND PLAIN 82
8.3 CELL IN A LAKE 84

CHAPTER 9 DISCHARGE ROUTING 85

9.1 CHANNEL ROUTING 85
9.2 LEVEL POOL ROUTING 90
9.2.1 Third order Runge-Kutta method 92
9.2.2 Fourth order Runge-Kutta method 93

CHAPTER 10 HYDRAULIC STRUCTURES 95

10.1 DAMS AND RESERVOIRS 95
10.2 ON-STREAM FLOOD DETENTION BASIN 95
10.3 OFF-STREAM FLOOD DETENTION BASIN 97
10.4 BYPASS AND DIVERSION CHANNELS 97

CHAPTER 11 GROUNDWATER 102

11.1 GROUNDWATER FLOW 102
11.2 RIVER-AQUIFER INTERACTION 106
11.3 BOUNDARY CONDITIONS 109

CHAPTER 12 IRRIGATION MANAGEMENT 112

CHAPTER 13 PLANTS GROWTH 116

REFERENCES 117

List of figures

Figure 1.1 Scheme of hydrological processes implemented within FeST model with main state variables and input data. 3
Figure 2.1 Interpolation of precipitation (mm) acquired by raingauges (circles) with Thiessen polygon method in the Toce river basin, Italy. 6
Figure 2.2 Interpolation of precipitation (mm) acquired by raingauges (circles) with IDW method in the Toce river basin, Italy. 8
Figure 2.3 Variogram graph. 10
Figure 2.4 Spherical semi-variogram model. 11
Figure 2.5 Exponential semi-variogram model. 11
Figure 2.6 Gaussian semi-variogram model. 12
Figure 2.7 A representation of geometric anisotropy in which the ellipse describes the range of a spherical variogram in two dimensions. The diameter A is the maximum range of the model, B is the minimum range, and φ is the direction of the maximum range (adapted from Webster e Oliver (2007). 13
Figure 2.8 Interpolation of precipitation (mm) acquired by raingauges (circles) with OK method in the Toce river basin, Italy. 15
Figure 2.9 Partitioning of solar radiation by the atmosphere. Source: (https://open.library.okstate.edu/rainorshine/chapter/11-3-net-radiation/) 17
Figure 2.10 Shortwave radiation affected by topography 18
Figure 2.11 A cross section of a valley to sketch the visible sky area from a slope in the valley. h(φ) is the maximum horizontal viewing angle of terrain obstruction in azimuth φ. ϑ(φ) is the zenith angle to the slope normal of terrain horizon on a sloped coordinate system in azimuth φ. Adapted from Zhang et al., 2017. 22
Figure 2.12 The sixteen directions along which shy view angle is computed for each cell: (0.0, 22.5, 45.0, 67.5, 90.0, 112.5, 135.0, 157.5, 180.0, 202.5, 225.0, 247.5, 270.0, 292.5, 315.0, 337.5 degree) 23

Figure 2.13 Traversed cells from the viewing point for 22.5° azimuth direction (green line), and 67.5° azimuth direction (red line). Points mark position of points computed as successive increment from the viewing point. 24

Figure 2.14 Shadow maps on the Toce river basin, Italy, for three different times: a) 2000-02-01T12:00:00+00:00, azimuth 180°, sun elevation 28°; b) 2000-02-01T08:00:00+00:00, azimuth 123°, sun elevation 7.6°; c) 2000-02-01T16:00:00+00:00, azimuth 233°, sun elevation 3°. 25

Figure 2.15 Shortwave radiation at 12:00 of 2000-02-01 on the Toce river, Italy, interpolated with inverse distance weighting without drift (left) and with elevation drift (right). Circles show stations where solar radiation was measured. 26

Figure 2.16 Schematic of the air temperature interpolation considering a vertical lapse rate and elevation drift. 29

Figure 2.17 Air temperature at 16:00 of 2017-06-14 on the Bolzano province, Italy, interpolated with inverse distance weighting without drift (IDW) and with elevation drift with lapse rate = -6.5 °C/km (IDW+lapse). Digital elevation model on the left. 29

Figure 2.18 Air temperature observations on the Bolzano province, Italy, plotted against station elevation, for two time step. Dotted line shows regression line. Linear regression equation and R2 metric are shown. The example on the left is of a time step where observations are strongly linearly correlated to elevation. The example on the right is of a time step where the correlation is very weak, due to thermal inversion phenomena very frequent in Alpine region during winter. 30

Figure 2.19 Wind speed at 12:00 of 2015-09-02 on the Toce river, Italy, interpolated with inverse distance weighting without drift (moddle) and with elevation drift (right). Digital elevation model on the left. 37

Figure 2.20 Schematic showing the horizontal discretization around an arbitrary grid point (i, j) at height h(i, j) whose velocity components v_x(i, j) and v_y(i, j) is calculated using the orographic correction. (*source*: González-Longatt et al. (2015)) 39

Figure 2.21 Example of interpolation of precipitation measurements on the Toce river basin, Italy, assigning two different zones (left) with id values 1 and 2 that corresponds to Thiessen and IDW interpolation methods, respectively. Final interpolated map is shown on the right. 41

Figure 2.22 Example of interpolation of wind speed data on the Toce river basin, Italy, using two methods: the IDW in zone with elevation lower than 2000 m a.s.l., and the Micromet method where elevation is greater than 2000 m a.s.l.. left map is obtained using only IDW, map in the middle is obtained using Micromet only, the right map is obtained with a mixing of the two methods. 41

Figure 2.23 Example of spatial reprojection of temperature data from geodetic reference system to UTM 32N. 42

Figure 2.24 Grid data resampling with nearest neighbour method. Source: https://www.brockmann-consult.de/beam/doc/help/general/ResamplingMethods.html 43

Figure 3.1 Rainfall is stored in the canopy until the maximum value at a given time, Ct, is reached (left). When Ct is reached, the excess rain reaches the ground as throughfall, T (right). 46

Figure 4.1 Coefficient of precipitation partitioning, αp, in liquid and solid phase 48

Figure 4.2 Snow accumulation and melting contribute to the updating of snow water equivalent (*SWE*) and water stored within snowpack. 49

Figure 4.3 Cells are connected by a lateral flux that transfers water accumulated within snowpack following the flow direction derived from digital elevation model. Flux magnitude is computed with *Darcy* equation and depends from actual water amount and local terrain slope. When lateral fluxes meets a cell not covered with snow (D), it is treated as a source term in the soil water balance. 50

Figure 5.1 Vertical and lateral fluxes interconnection scheme on cells covered by snow and ice (A,B), only covered by ice (C), and free from snow and ice (D). 53

Figure 6.1 Infiltration profile for the Green-Ampt model. Adapted from *Kale and Sahoo*, 2011. 63

Figure 6.2 Flow chart for determining infiltration and ponding time under variable rainfall intensity. (*Chow et al.*, 1988) 66

Figure 7.1 Vertical distribution of wind speed over a vegetated surface of height h. The profile follows the logarithmic distribution. The zero plane displacement d is about $0.7\ h$. The wind speed becomes zero at $d + zom$ (*Immerzeel et al.*, 2006) 76

Figure 8.1 Water balance for a soil volume with the fluxes Q_{in} entering the volume and Q_{out} exiting the volume. (*https://www.cambridge.org/core/books/climate-change-and-terrestrial-ecosystem-modeling/soil-moisture/94367F1E2A95F1B991C333BB0637409C*) 79

Figure 8.2 Water flows in a soil column extending from the ground surface to the water table. (*https://www.cambridge.org/core/books/climate-change-*

and-terrestrial-ecosystem-modeling/soil-moisture/94367F1E2A95F1B991C333BB0637409C) 80
Figure 8.3 Soil balance scheme of cell on hillslope. RZD = root zone depth, TZD = transmission zone depth, I = infiltration, ET = evapotranspiration, RSE = saturation excess from root zone, P = percolation, TSE = saturation excess from transmission zone, LF_{in} = input lateral flux, LF_{out} = output lateral flux, DP = deep percolation. 82
Figure 8.4 Soil balance scheme of cell in land plain. RZD = root zone depth, TZD = transmission zone depth, I = infiltration, ET = evapotranspiration, RSE = saturation excess from root zone, P = percolation, TSE = saturation excess from transmission zone, CR = capillary rise flux, DP = deep percolation 83
Figure 10.1 Bypass and diversion channel. Image Credit: *Schulte et al.*, 2018. 98
Figure 11.1 *Von Neumann* neighbourhood definition (left) that considers the group of four cells in the four cardinal directions from the central one, and (right) the *Moore* method that includes the adjacent cells along diagonals. 103
Figure 11.2 Scheme for the calculation of water fluxes between the central cell and the four adjacent cells. W_C is the volumetric flux representing source (entering the cell) or sink (exiting the cell). 104
Figure 11.3 Conceptual representation of river-aquifer interconnection: Q is the discharge, L is the stream length, W is the stream width, M is the streambed thickness, hw is the hydraulic head in the stream, and h is the hydraulic head in the aquifer. 107
Figure 11.4 Aquifer conceptual model: scheme of boundary conditions. In Neumann type boundary cells, the subsurface flow coming from hydrological simulation is transformed into a flux entering unconfined aquifer along the border. Dirichlet type boundary condition cells are set along the eastern border of the aquifer that continues downward into the Po valley. 110

List of boxes

Box 2.A Reliability of methods to interpolate precipitation 16
Box 2.B Using lapse rate improves temperature interpolation 31
Box 2.C Convention for wind speed direction 33
Box 2.D The Micromet method on the Upper Po river basin 37
Box 5.A Glaciers initial conditions 53
Box 6.A The ponding time 56
Box 6.B The *Brooks and Corey* water retention curve 57
Box 6.C The time compression approximation 61
Box 6.D Soil hydrological parameter estimates based on soil texture. 67
Box 7.A Potential and actual evapotranspiration 69
Box 7.B Reference evapotranspiration and the crop coefficient 70
Box 9.A The Newton-Raphson algorithm to derive the normal depth 86
Box 9.B Hydraulic properties for triangular, rectangular and trapezoidal cross sections 89
Box 9.C Idro lake simulation 91
Box 10.A The Gurone detention basin on the Olona river 96
Box 10.B The diversion channel on the Seveso river 98
Box 11.A Drawdown due to a constant pumping rate from a well 104
Box 11.B Aquifer response to stream-stage variation 108

List of tables

Table 6.1 The $CNII$ parameter values as a function of CORINE land cover class and hydrological class (A, B, C, and D) 59

INTRODUCTION

FeST is a spatially distributed hydrological model, developed at Politecnico di Milano (www.polimi.it) by the Real Time Hydrology Group (www.fest.polimi.it). *FeST* is the acronym of “flash–Flood Event–based Spatially distributed rainfall–runoff Transformation” that denotes how the first release of the model was initially developed by Mancini (1990), as a model oriented to the simulation of rainfall-runoff transformation of single flood events. Later the *FeST* model was merged with the soil water balance scheme from TOPLATS model (Famiglietti and Wood, 1994), transforming it into a continuous model (Montaldo et al., 2007). Then the FeST code was redesigned and rewritten from scratch while keeping the basic assumptions of the previous release (Rabuffetti et al., 2008). In 2011 the *FeST* was upgraded with a routine to solve the system of water mass and energy balance in order to better simulate the actual evapotranspiration and interface the model to remotely sensed data (Corbari et al., 2011; Corbari & Mancini, 2014). At the same year, 2011, a new module for simulating groundwater flux and river-groundwater interaction was developed and implemented in the *FeST* (Ravazzani et al., 2011). In 2013 a new version of the code was released built on top of the MOSAICO library (Ravazzani, 2013). In 2014 the *FeST* was upgraded with a module for glaciers modelling (Boscarello et al., 2014). In 2021 a forest growth component was implemented in the *FeST* (Feki et al., 2021).

FeST has been applied to a wide range of water resources applications such as discharge assessment for flood risk analysis (Ravazzani et al., 2014), flood forecasting (Amengual et al., 2017), soil moisture assessment and forecasting for irrigation scheduling (Ceppi et al., 2014; Ravazzani et al., 2017), impacts assessment of climate and land-use changes on water resources availability and flood severity (Ceppi et al., 2022; Ravazzani et al., 2015; Gaudard et al., 2014; Ravazzani et al., 2014).

This document provides documentation about the equations and algorithms implemented within the *FeST* model in order to simulated hydrological processes.

CHAPTER 1

FEST MODEL SCHEME

The FeST model is a spatially distributed model. The simulation domain is discretized into regular square cells (typical application range: 10-5000 m) within which equations that describe hydrological processes are solved with a time step according to the available meteorological input data, the simulated processes, and the characteristics of the simulation domain (area, slope, etc..) that is usually set in the range 1 hour - 1 day.

The FeST model is written in Fortran 90 with a modular approach so that only the dominant processes can be simulated for any specific studies (Figure 1.1). As an example, the snow module that simulates snow melt and accumulation is not relevant for simulating hydrological balance of a tropical river basin but it is fundamental when the simulation of snow melt is required for managing hydropower production over the Alpine mountains.

For running a simulation, the FeST model requires meteorological input data. These can be site measurements acquired by meteorological stations or multidimensional raster data coming from weather forecast or climatic mathematical models. Station site data are interpolated over the simulation domain using different algorithms such as, Thiessen (1911) polygons, inverse distance weighted, or kriging methods. Specific methods are implemented to account for topographic effect on air temperature, solar radiation, and wind speed. Gridded air temperature data that are usually at a coarser spatial resolution than spatial step of hydrological simulation, are downscaled to higher resolution considering actual elevation from the digital elevation model. The snow module gets precipitation data, both from rain gauges and gridded dataset, and simulate snow accumulation, as snow water equivalent, and melting. The glacier module simulates glacier melting and interacts with snow module for glacier accumulation. The soil balance module computed evapotranspiration, infiltration, runoff, percolation and updates soil moisture. Some state variables are shared with plants module such as soil moisture and leaf area index, so that there is a mutual interaction between soil balance and plants modules. Drainage from soil balance is used as groundwater recharge. Runoff is the source term of routing module that simulates flow discharge. The resulting discharge time series can be affected by natural or artificial regulated reservoirs or bypass channels.

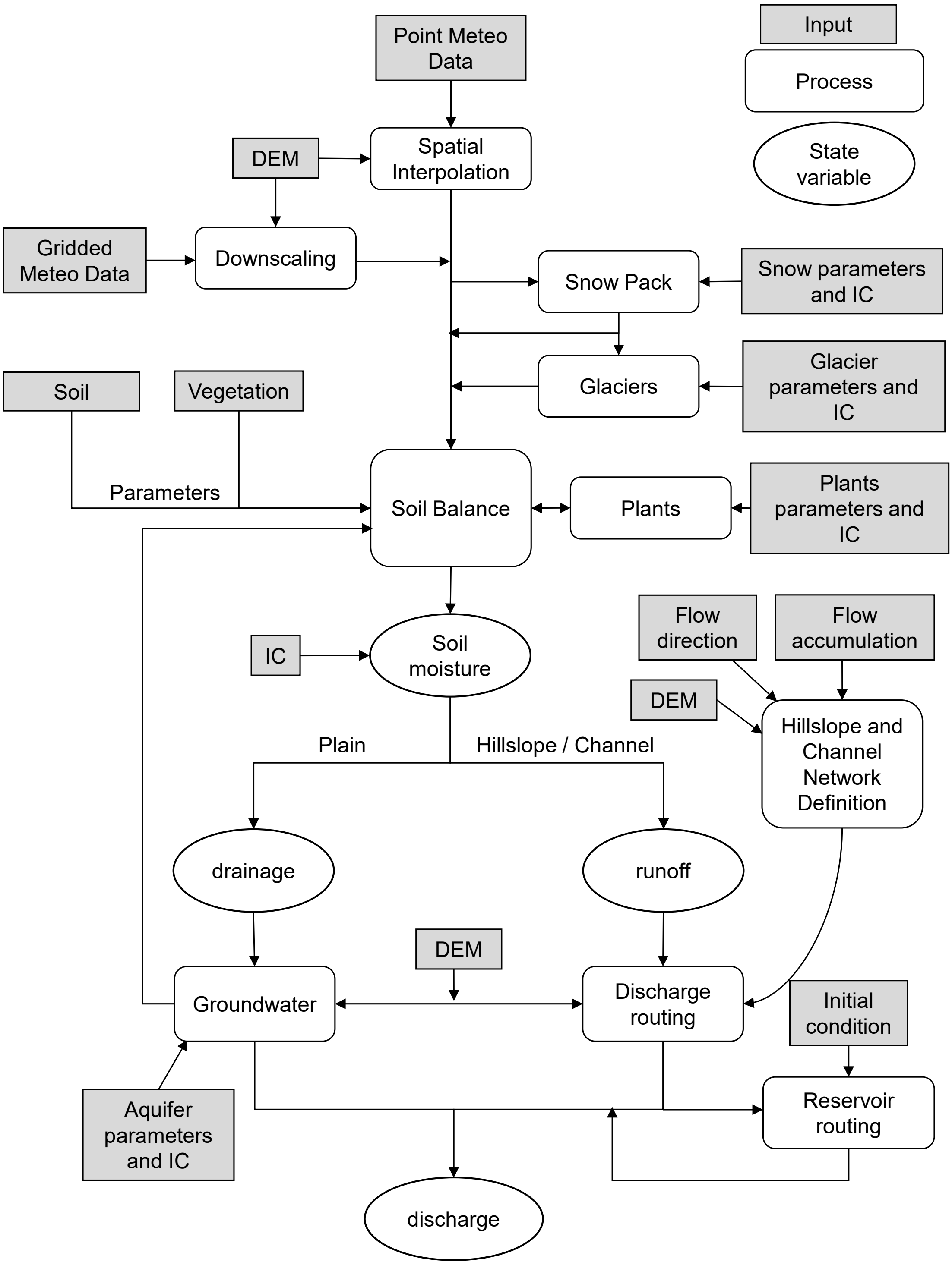
Input
Process
State variable
Point Meteo Data
DEM
Spatial Interpolation
Gridded Meteo Data
Downscaling
Snow Pack
Snow parameters and IC
Glaciers
Glacier parameters and IC
Soil
Vegetation
Parameters
Soil Balance
Plants
Plants parameters and IC
Flow direction
Flow accumulation
IC
Soil moisture
DEM
Hillslope and Channel Network Definition
Plain
Hillslope / Channel
drainage
runoff
DEM
Groundwater
Discharge routing
Initial condition
Reservoir routing
Aquifer parameters and IC
discharge

Figure 1.1 Scheme of hydrological processes implemented within FeST model with main state variables and input data.

CHAPTER 2

METEOROLOGICAL DATA

This section provides information about how meteorological data are processed before being used for hydrological simulation. Station measurements are interpolated according to one of the three available options, Thiessen polygons, inverse distance weighting, and kriging methods. Station coordinates are converted to the spatial reference system of the simulation domain, before interpolation takes place. For considering effect of topography on meteorological data, some specific algorithms are, optionally, applied for interpolating solar radiation, air temperature, precipitation, and wind speed. Gridded data are converted to the proper reference system and spatially downscaled to the simulation grid resolution with nearest neighbour resampling method.

2.1 Spatial interpolation methods

2.1.1 Thiessen polygons

The Thiessen polygon method (Thiessen, 1911) is one of the simplest techniques, still widely used in hydrological studies, also referred to as the nearest neighbour method or Voronoi tessellation. It predicts the attributes of unsampled points based on those of the nearest sampled point. Polygons are drawn according to the distribution of the sampled data points, with one polygon per data point, which is then located in the centre of the polygon (Hartkamp et al., 1999). This method produces an abrupt transition between boundaries.

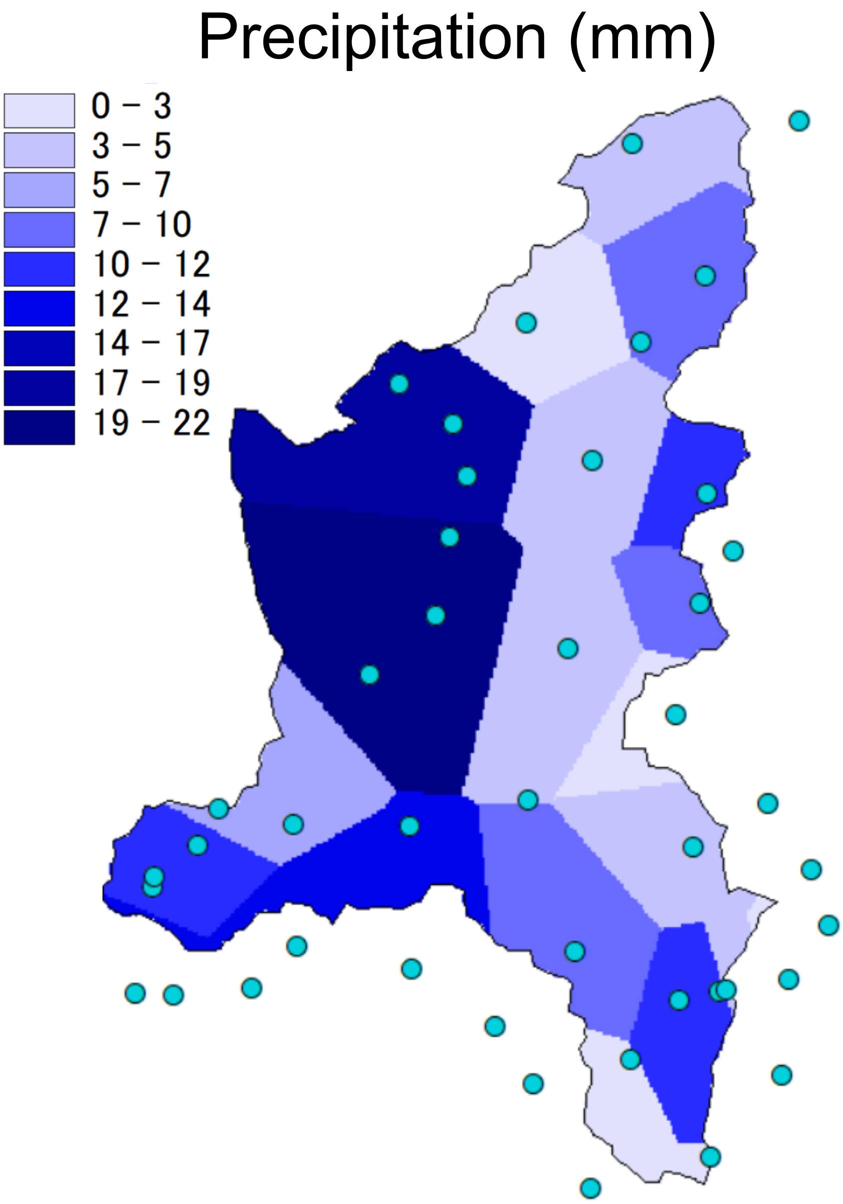
Precipitation (mm)
0 – 3
3 – 5
5 – 7
7 – 10
10 – 12
12 – 14
14 – 17
17 – 19
19 – 22

Figure 2.1 Interpolation of precipitation (mm) acquired by raingauges (circles) with Thiessen polygon method in the Toce river basin, Italy.

2.1.2 Inverse distance weighting

The inverse distance weighting (IDW) is a deterministic estimation method whereby values at unsampled points are determined by a combination of values at known sampled points. Weighting of nearby points is strictly a function of distance (Shepard, 1968). The assumption is that values closer to the unsampled location are more representative of the value to be estimated. This method produces a gradual change of interpolated surface. The weight, λ, of the i^{th} unsampled point is computed as:

$$\lambda_i = \frac{1/d_i^p}{\sum_{i=1}^{n} 1/d_i^p} \qquad \text{2-1}$$

where d_i is the distance from the known point to the unsampled point, n is the total number of known points used in interpolation and p is a positive real number, called the power parameter.

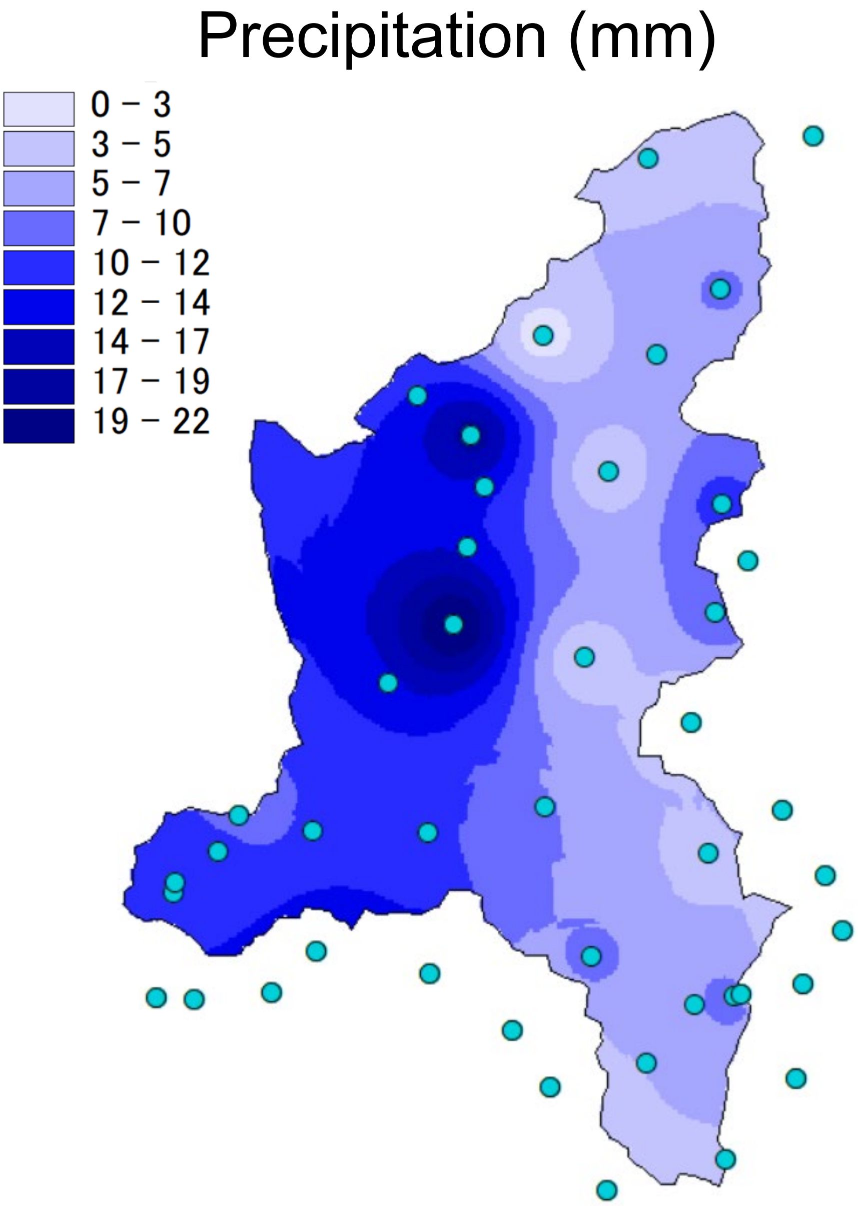

Figure 2.2 Interpolation of precipitation (mm) acquired by raingauges (circles) with IDW method in the Toce river basin, Italy.

2.1.3 Kriging (ordinary)

The main assumption at the base of geostatistical methods is to consider variables of interest as random variables, and the observed reality as the result of random processes. The most popular geostatistical method is the Kriging method, which defines the interpolated value as a linear combination of weighted known values. The theoretical basis for the method was developed by the French mathematician Georges Matheron in 1960, based on the master's thesis of Danie G. Krige, the pioneering engineer who developed the stochastic approach to compute the accuracy of the estimated gold concentration in mining engineering in the 1950s. Kriging is a weighted mean in which weights are chosen so that the error associated with the estimator is as small as possible. Weights depend on the position of the points used for the interpolation and on the covariance that is reflected in the variogram (Pari and Nofziger, 1987).

The most commonly used kriging method is the ordinary kriging, from now on pointed as OK. The aim of OK is to estimate the value of a random variable $z(x)$ at a point x_0 (so $z(x_0)$), using data $z(x_i)$ in the neighbourhood of the estimation location as reported in equation 2-2 where λ_i are the OK weights and n is the number of data closest to the location x_0 to be estimated (Pellicone et al., 2018)

$$z_0^* = z^*(x_0) = \sum_{i=1}^{n} \lambda_{0_i} z(x_i) = \sum_{i=1}^{n} \lambda_{0_i} z_i \qquad 2\text{-}2$$

In particular, λ_i values must be evaluated in order to obtain an unbiased estimation and to minimize the variance (equation 2-5). By imposing that the interpolated value has to be unbiased we obtain that the weights sum must be equal to 1 (equation 2-4).

$$\in_0 = z^*(x_0) - z(x_0) = z_0^* - z_0 \qquad 2\text{-}3$$

$$\overline{\in_0} = E[z_0^* - z_0] = 0\; z_0^* - z_0 => \sum_{i=1}^{n} \lambda_{0_i} = 1 \qquad 2\text{-}4$$

$$Var(\in_0) = Var[z_0^* - z_0] = E[(z_0^* - z_0)^2] \rightarrow min \qquad 2\text{-}5$$

By substituting equation 2-2 in equation 2-5, and by taking into account the constraint expressed by equation 2-4, the following expression is obtained,

$$Var(\epsilon_0) = -\sum_{i=1}^{n}\sum_{j=1}^{n}\lambda_{0_i}\lambda_{0_j}\gamma(x_i - x_j) + 2\sum_{i=1}^{n}\lambda_{0_i}\gamma(x_i - x_0) \qquad \text{2-6}$$

where γ is the variogram, a growing monotone function representing the spatial correlation of points at increasing distance; it's closely related to the covariance function and it's defined by equation:

$$\gamma(h) = \frac{1}{2}E\left[\big(z(x) - z(x+h)\big)^2\right] = \sigma_z^2 - C(h) \qquad \text{2-7}$$

where h is called lag and it represents the distance between two points x and $x + h$, z is the value of the considered random variable measured in the two points, σ_z^2 is the variance of the random variable z and $C(h)$ is the covariance of $(z(x), z(x + h))$.

The variogram graph (Figure 2.3) shows on the horizontal axis the lag h, on the vertical axis the variogram and it's characterized by 3 parameters:

- sill (threshold): it's the value of the variogram for which $\gamma(h)$ becomes constant ($C(h) \approx 0$), corresponding to uncorrelated observations of the variable z (asymptote of the variogram) (here, $C_0 + C_1$);
- range (or lenght): it's the distance at which the observations are no longer correlated (it can be infinite or finite); usually is computed as the distance at which the 95% of the sill is reached;
- nugget: it's the discontinuity visible at the origin and it represents variations of very small scale and/or measurement errors (here C_0).

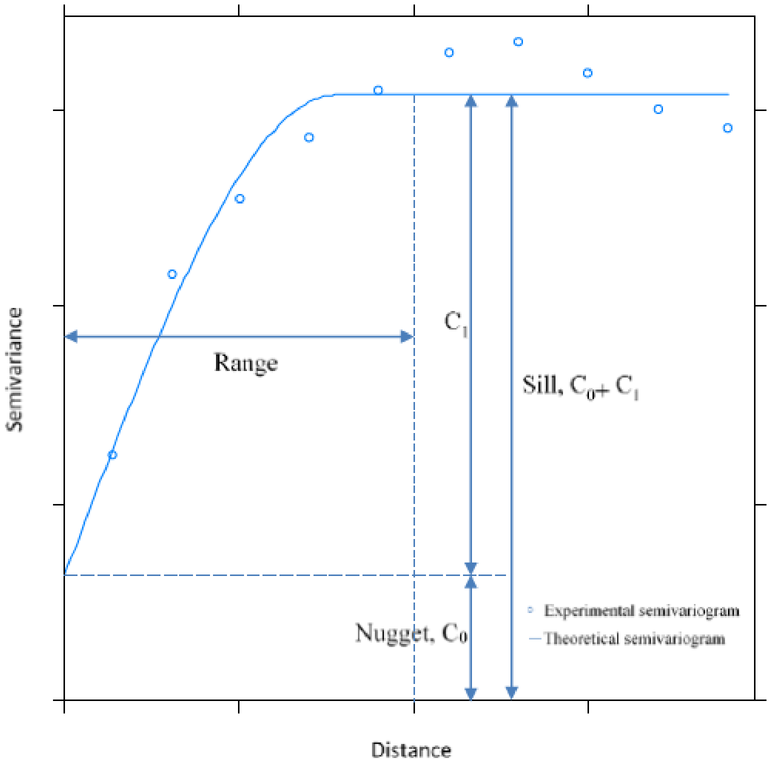

Figure 2.3 Variogram graph.

So, before starting to use the OK method, it's necessary to perform the variographic analysis, that means to compute an experimental variogram by using the available data, and then to fit a variogram model on the experimental one.

Several variogram models exist. Some of the most common are:

- Spherical $$\gamma(h) = \begin{cases} c\left(\frac{3h}{2a} - \frac{1}{2}\left(\frac{h}{a}\right)^3\right), & h \leq a \\ c, & h > a \end{cases} \tag{2-8}$$
- Exponential $$\gamma(h) = c\left\{1 - \exp\left(-\frac{h}{r}\right)\right\} \tag{2-9}$$
- Gaussian $$\gamma(h) = c\left\{1 - \exp\left(-\frac{h}{r}\right)\right\} \tag{2-10}$$

where c is the sill and a is the range.

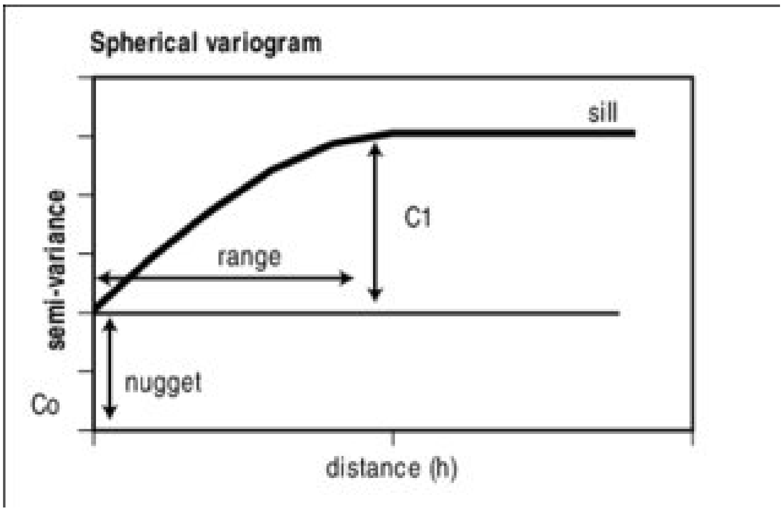
Spherical variogram
sill
C1
range
semi-variance
nugget
Co
distance (h)

Figure 2.4 Spherical semi-variogram model.

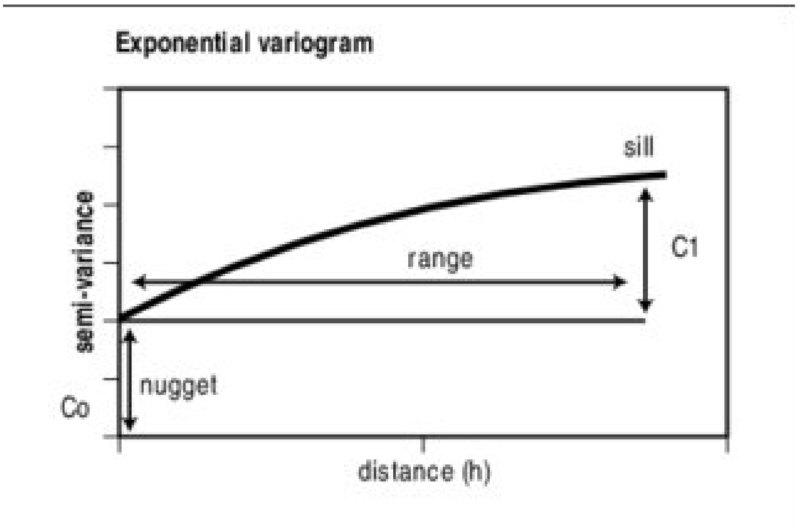
Exponential variogram
sill
C1
range
semi-variance
nugget
Co
distance (h)

Figure 2.5 Exponential semi-variogram model.

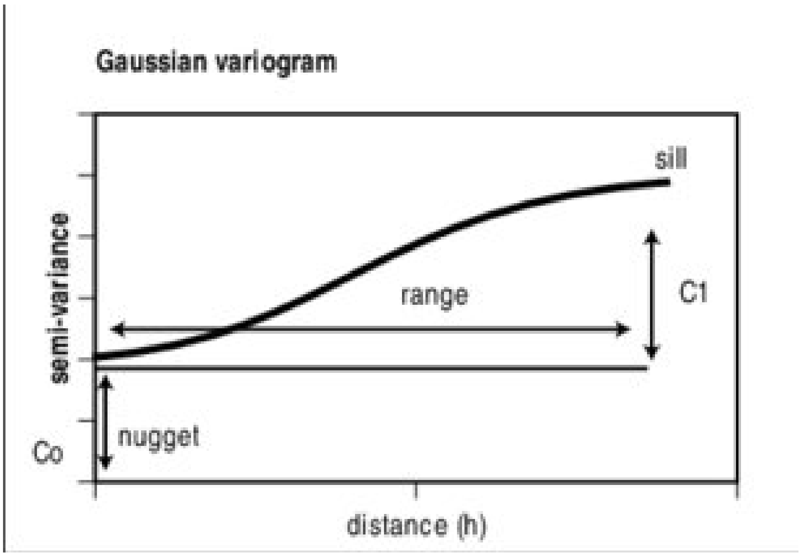

Figure 2.6 Gaussian semi-variogram model.

The experimental variogram $\hat{\gamma}(h)$ is a discrete function of the lag h computed by using the following equation between pairs of points [$z(x_i)$, $z(x_i+h)$] at various distances, where $n(h)$ is the number of data pairs for the specified lag vector h.

$$\hat{\gamma}(h) = \frac{1}{2n(h)}\sum_{i=1}^{n(h)}[z(x_i + h) - z(x_i)]^2 \qquad \text{2-11}$$

The procedure implemented in the FeST model implies that, firstly the semivariogram is generated from a given sample. The sample point pairs are ordered into even-width bin, separated by the euclidean distance of the point pairs. The semivariance in the bin is calculated by the Matheron estimator (eq. 2-10). If number of lags and lag max distance are not given they are automatically computed or set to default value, 15. The user can choose among spherical, exponential and gaussian semivariogram models or leave the program to automatically fit it to the best fitting model among the three, considering the nugget effect. Fitting algorithm is adapted from the VARFIT model by Pardo-Iguzquiza (1999). The VARFIT algorithm performs a nonlinear minimization of the weighed squared differences between the experimental variogram and the model.

$$F(\theta) = \sum_{i=1}^{NDIR}\sum_{j=1}^{NLAG(i)} w(i,j)[\hat{\gamma}(i,j) - \gamma(i,j;\theta)]^2 \qquad \text{2-12}$$

where *NDIR* is the number of directions. *NLAG*(i) is the number of lags in the ith direction, $\hat{\gamma}(i,j)$ is the experimental variogram for the ith direction and jth lag, $\gamma(i,j;\theta)$ is the variogram model with parameters vector θ.

By considering several directions in fitting the variogram, anisotropy can be accomplished. Indeed, variation can itself vary with direction. In this case the range, instead of being a constant, describes an ellipse in the plane of the lag. This is shown in Figure 5.13, where A is the maximum diameter of the ellipse, i.e. the range in the direction of greatest continuity (least change with separating distance), and B is the minimum diameter, perpendicular to the first, and is the range in the direction of least continuity (greatest change with separating distance). The angle φ is the direction in which the continuity is greatest.

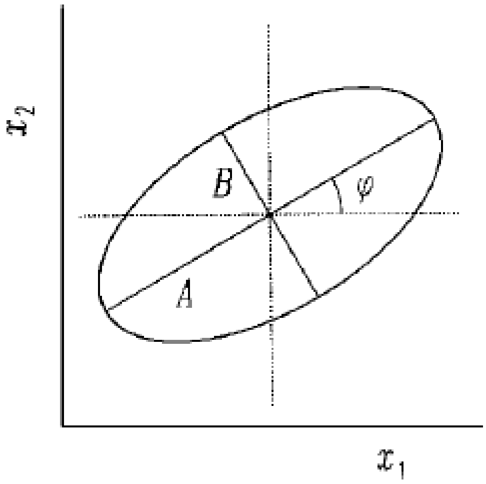

Figure 2.7 A representation of geometric anisotropy in which the ellipse describes the range of a spherical variogram in two dimensions. The diameter A is the maximum range of the model, B is the minimum range, and φ is the direction of the maximum range (adapted from Webster e Oliver (2007).

When anisotropy option is activated by the user, the FeST computes the empirical variogram in the four directions:

- East-South (0°)
- NorthEast-SouthWest (45°)
- North-Sout (90°)
- NorthWest-SoutEast (315°)

The weighting function, w is computed as:

$$w(i,j) = N(i,j)[\gamma(i,j);\theta]^{-2} \qquad 2\text{-}13$$

where $N(i,j)$ is the number of data pairs used to obtain the estimate $\hat{\gamma}(i,j)$.

The weighting function has an important statistical attraction. The uncertainty of the variogram estimate $\hat{\gamma}(i,j)$ is (Cressie, 1985):

$$Var[\hat{\gamma}(i,j)] \approx [\gamma(h)]^2/N(h) \qquad 2\text{-}14$$

where *Var* [*X*] is the variance of the random variable *X*, $\gamma(h)$ is the true variogram and *N*(h) is the number of data pairs used in the estimation of i $\hat{\gamma}(i,j)$.

Then it is logical to weigh each estimate $\hat{\gamma}(i,j)$ by the inverse of its estimation variance. These weights (the inverse of the estimation variance) are optimal when the different estimates are independent (Hoel, 1984). This is not the case for the experimental variogram where the different estimates ($\hat{\gamma}(i,j)$ for different h) are correlated; in this situation a generalized least squares method would be more appropriate; but the weighted least squares represent a good compromise of statistical efficiency and computability (Cressie, 1985). This weighting function seems to give good results in practice (Gotway, 1991; Zimmerman and Zimmerman, 1991).

VARFIT uses a non-linear minimisation method that does not require (explicit) initial values for the parameters in order to initialise the minimisation algorithm. Jian et al. (1996) report problems with convergence if the initial guess is poor. Solution is found with the simplex method of function minimization of Nelder and Mead (1965). This ingenious method is efficient for non-linear minimization in a multiparameter space but is still easy to program and only requires evaluations of the objective function. The program stops the iterations whenever one of the two following criteria is reached:

1. Convergence is reached
2. The maximum number of iterations is reached.
3. The best fitted semivariogram model is used

The best fitted semivariogram model is used to interpolate a regular grid of data. Code is adapted from the Geostats program written by Luke Spadavecchia, Biosphere Atmosphere Modelling Group, University of Edinburgh, November 2006. A number of closest points are used to build the covariance matrix used to predict value at location where value is unknown. Matrix inversion uses the the Gauss-Jordan method. An n*2,n work array is assembled, with the array of interest on the left half, and the identity matrix on the right half. A check is made to ensure the matrix is invertable, and the matrix inverse is returned, providing the matrix is not singular. The matrix is invertible if, after pivoting and row reduction, the identity matrix shifts to the left half of the work array.

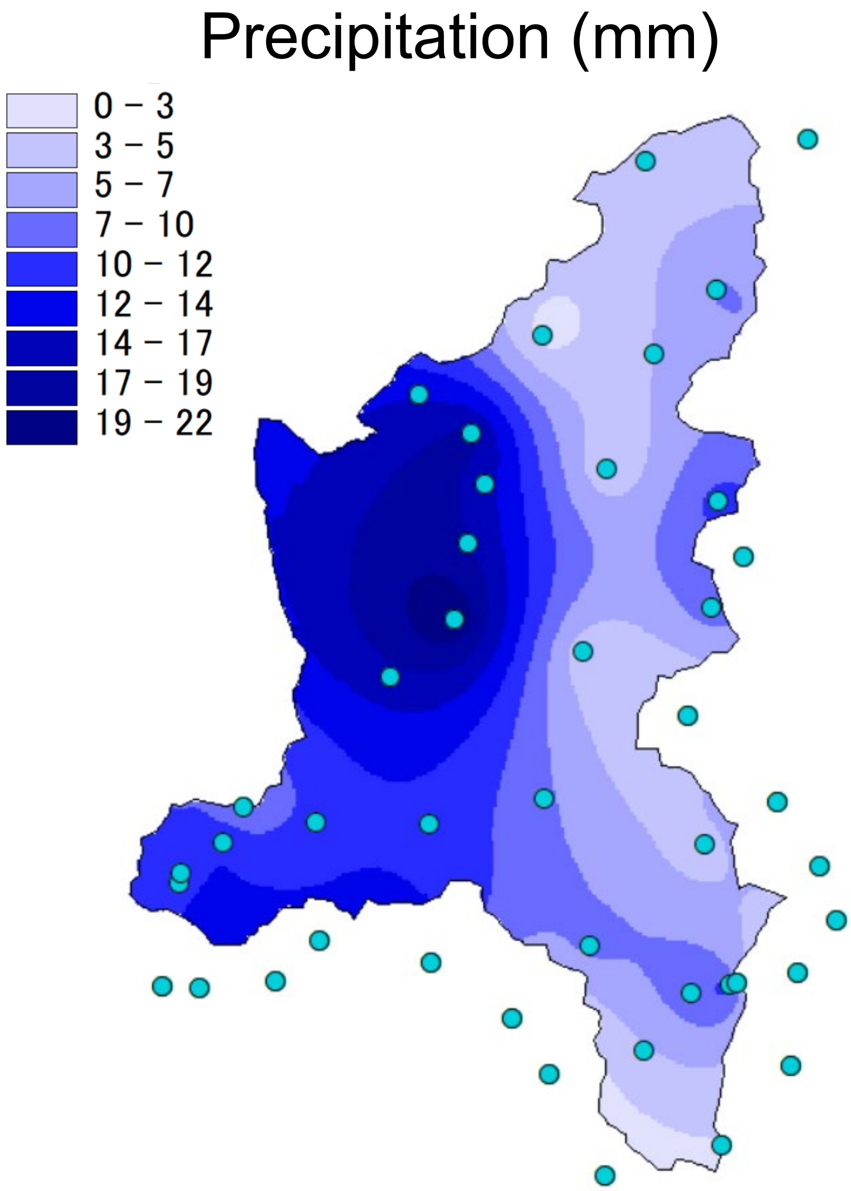
Precipitation (mm)
0 – 3
3 – 5
5 – 7
7 – 10
10 – 12
12 – 14
14 – 17
17 – 19
19 – 22

Figure 2.8 Interpolation of precipitation (mm) acquired by raingauges (circles) with OK method in the Toce river basin, Italy.

Box 2.A Reliability of methods to interpolate precipitation

Three techniques – Thiessen, IDW, and OK – are evaluated for interpolation of precipitation data available through the WegenerNet data portal (https://wegenernet.org/).

The WegenerNet site is located in the South-East of Austria, in the federal state of Stiria, close to Feldbach, in the Raab river's valley. It's a hilly area, with a range of elevation that goes from 257 to 609 m a:s:l. The University of Graz installed a net of 150 weather stations placed on a regular grid with a density of one station per 2 km^2 and 5-min interval data acquisition. Data are available since Jan 1, 2007. In this analysis data of 2016 were used.

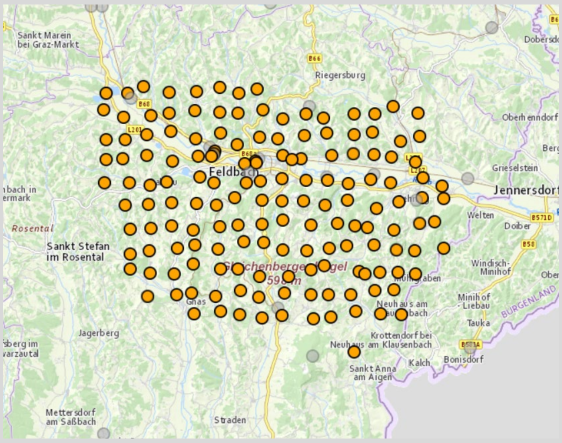
Sankt Marein bei Graz-Markt
Riegersburg
Feldbach
Sankt Stefan im Rosental
Rosental
Jagerberg
Gnas
Straden
Mettersdorf am Saßbach
Jennersdorf
Gritselstein
Oberhenndorf
Welten
Doiber
Windisch-Minihof
Minihof-Liebau
Tauka
BURGENLAND
Neuhaus am Klausenbach
Kalch
Bonisdorf
Sankt Anna am Aigen
Krottendorf bei Neuhaus am Klausenbach

Map of available stations in the WegenerNet data portal (https://wegenernet.org/).

In order to evaluate and compare the performance of interpolation methods, the *leave-one-out* statistical method is adopted. It checks the compatibility between the input data and the model by removing once at time each data point from the dataset and by using information from remaining data-points to predict the variable value in the point temporarily from the dataset. Performance indexes are computed at every time step (hour) and averaged over the whole period (2016).

Performance results in terms of root mean square error (*RMSE*) normalised RMSE (*NRMSE*), the coefficient of determination (*NSE*), and Pearson correlation coefficient (*PCC*) for Thiessen, IDW and OK with exponential semivariogram.

	RMSE	*NMRSE*	*NSE*	*PCC*
Thiessen	0.390	1.022	0.052	0.527
IDW	0.336	0.825	0.412	0.623
OK exponential	0.300	0.788	0.442	0.618

Results show that Thiessen is the worst method, while IDW and OK have comparable performance.

2.2 Net radiation over complex topography

When the direct and diffuse shortwave (solar) radiation reach the land surface, some of this radiation is reflected by the surface (Figure 2.9). The fraction of the incoming shortwave radiation that is reflected by the surface is called the albedo. In addition to the shortwave radiation, we need to account for the longwave radiation at the land surface. land surface emits longwave radiation to the atmosphere. But, we should not overlook the fact that the atmosphere emits longwave radiation both upward into space and downward toward the Earth's surface. The magnitude of this downward longwave radiation depends on the temperature and emissivity of the atmosphere. The presence of clouds significantly increases the emissivity of the atmosphere. The amount of water vapor in the atmosphere also has a strong effect on the atmospheric emissivity, with higher emissivity values for more humid conditions.

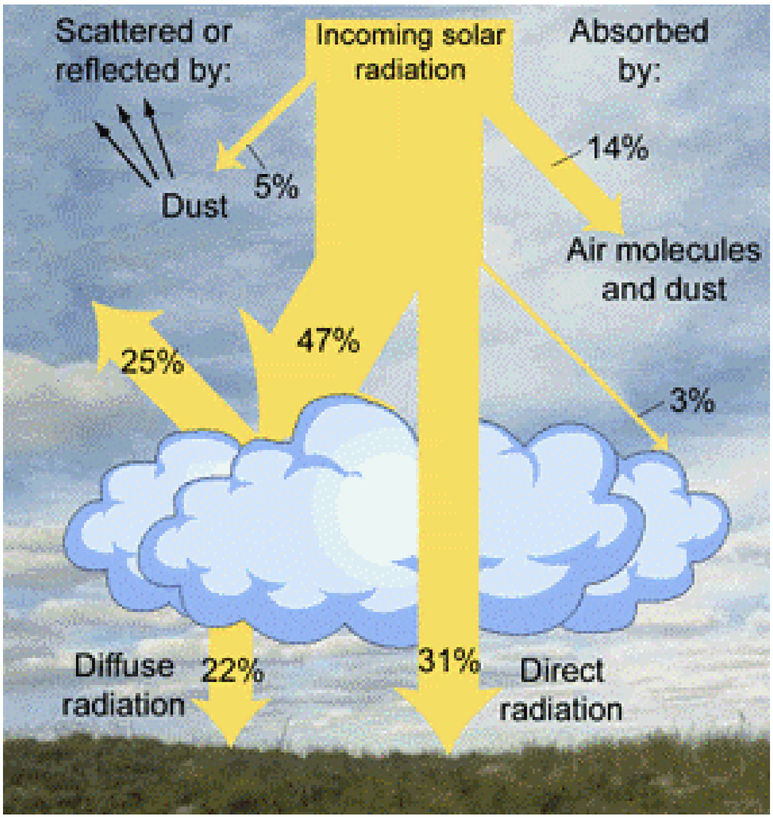
Scattered or reflected by:
Incoming solar radiation
Absorbed by:
Dust
5%
14%
Air molecules and dust
25%
47%
3%
Diffuse radiation
22%
31%
Direct radiation

Figure 2.9 Partitioning of solar radiation by the atmosphere. Source: (https://open.library.okstate.edu/rainorshine/chapter/11-3-net-radiation/)

Net radiation is simply the sum of all incoming and outgoing radiation fluxes at the land surface. Mathematically, net radiation, R_n, is given by:

$$R_n = S_{in} - S_{out} + L_{in} - L_{out} \tag{2-15}$$

with

$$S_{in} - S_{out} = (1 - r)S_{in} \qquad \text{2-16}$$

$$L_{in} - L_{out} = (1 - r)R_{ld} - R_{lu} \qquad \text{2-17}$$

where S denotes shortwave radiation, L longwave radiation, subscripts in and out denotes input and output to and from the ground, respectively, r is albedo, R_{ld} is longwave radiation emitted from ground, and R_{lu} is longwave radiation emitted from atmosphere.

2.2.1 Shortwave radiation

The radiation components can be highly modified by local and surrounding topography. In fact the topography affects the radiation field in three ways (Figure 2.10):

1. modulating the actual energy flux according to the relative position of the ground surface with respect to the sun;
2. reducing radiation because of shadowing effect of the higher crests of mountains;
3. increasing net radiation by the fraction reflected from neighbouring terrains.

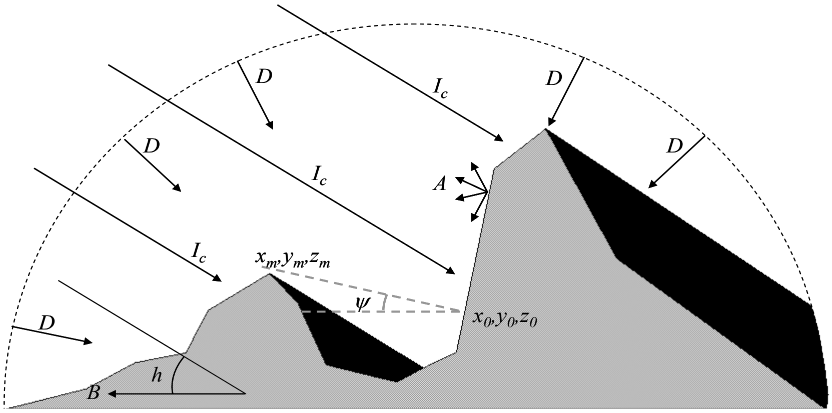

Figure 2.10 Shortwave radiation affected by topography

When option is set by user to account for topography effect, the *FeST* model adjusts incoming shortwave radiation before computing net radiation.
The incident short wave radiation can be expressed as:

$$S_{in} = Q_a + DF + A \qquad \text{2-18}$$

where Q_a is direct radiation component affected by topographic characteristics, such as slope and aspect, DF is the actual scattered radiation from sky, A is the radiation reflected from neighbour terrain.

The position of the Sun in the sky is expressed in terms of the solar altitude and the solar azimuth. The height of the Sun, the elevation of the Sun, is usually given in terms of the solar altitude h. This is the angular distance between the Sun's rays and the horizon (Gates, 1980). And the solar azimuth, B, is the horizontal angle with respect to north (Oke, 1987).

$$sin(h) = sin(\phi)\, sin(d) + cos(\phi)\, cos(d)\, cos(\eta) \tag{2-19}$$

$$cos(B) = [sin(d)\, cos(\phi) - cos(d)\, sin(\phi)\, cos(\eta)]/cos(h) \tag{2-20}$$

where ϕ is the local latitude and η is the solar hour angle (Iqbal, 1983)

$$\eta = 15(t - 12) \tag{2-21}$$

t is the hour of day.
Solar declination, d, is the angle between the Earth–Sun line and the equatorial plane (Iqbal, 1983).

$$d = \begin{pmatrix} 0.006918 - 0.399912\, cos(\Gamma) + 0.070257\, sin(\Gamma) - 0.006758\, cos(2\Gamma) \\ +0.000907\, sin(2\Gamma) - 0.002697\, cos(3\Gamma) + 0.00148\, sin(3\Gamma) \end{pmatrix} \tag{2-22}$$

Γ is the day angle:

$$\Gamma = \frac{2\pi(J-1)}{365} \tag{2-23}$$

where J is the Julian day, representing number of days after 1 January.
In clear sky conditions, the incoming solar radiation reaching the ground in the normal direction is:

$$I_c = I_0\, exp\left[{}^{-s}/_{sin(h)}\right] sin(h) \tag{2-24}$$

where I_0 is direct solar irradiance at the top of the atmosphere (solar constant =1367 W/m^2), s is the atmosphere optical depth (Kreider and Kreith, 1978):

$$s = s_0 \frac{P_z}{P_0} \tag{2-25}$$

with s_0 the atmospheric optical depth at sea level:

$$s_o = \sqrt{1229 + \left(614\, sin(h)\right)^2} - 614\, sin(h) \tag{2-26}$$

P_z/P_0 is a correction factor that takes into account the difference in atmospheric pressure between sea level (P_0) and actual elevation (P_z):

$$P_h/P_o = \left((288 - 0.0065\, z)/288\right)^{5.256} \tag{2-27}$$

where z is the altitude above sea level.

The scattered radiation for clear sky condition, D, is:

$$D = k_b(I_0 sin(h) - I_c) \tag{2-28}$$

where k_b varies from 0.2 to 0.6 according to the sky brightness (set to 0.4 in the *FeST* model).
In clear sky condition, the theoretical radiation observed at the ground level, R^*, is expressed by:

$$R^* = I_c + D \tag{2-29}$$

The presence of clouds or natural obstacles reduces the direct radiation I_c and modifies the scattered one so that R^* can be reduced to a minimum fraction, p, of R^* (usually $p = 0.22$ is referred to a transmissivity coefficient for 8/8 stratocumulus cloud cover; Male and Granger, 1981). When the observed radiation is less or equal to $p\ R^*$, radiation is considered totally scattered (sky totally covered with clouds). Otherwise, the fraction of scattered radiation, K_t, is computed as (Ranzi, 1989):

$$K_t = \frac{R^* - Rs}{[(1-p)R^*]} \tag{2-30}$$

Finally, the component of the actual scattered radiation, *DF*, can be computed as:

$$DF = min[R_s, D(1 - K_t) + R_s K_t] \qquad 2\text{-}31$$

and direct radiation component, *Q*, as:

$$Q = R_s - DF \qquad 2\text{-}32$$

Direct radiation component, *Q*, is affected by topographic characteristics, such as slope, α, and aspect, *E*. Actual direct radiation, Q_a, is related to the sun elevation as:

$$Q_a = \frac{Q\,cos(C)}{sin(h)} \qquad 2\text{-}33$$

The angle (Figure 2.10) between the sunbeam direction and the perpendicular to the ground is evaluated with:

$$cos(C) = cos(h)sin(\alpha)cos(B - E) + sin(h)cos(\alpha) \qquad 2\text{-}34$$

The radiation reflected from neighbour terrain is:

$$A = Q_a \cdot r \cdot (1 - f_\alpha) \qquad 2\text{-}35$$

where $f_\alpha = 1 - \alpha/180°$.

A module taking into account the shadow effect induced by topography was developed. Firstly, the algorithm determines for each cell the sky view angle, that is the maximum horizontal viewing angle of terrain obstruction in a given direction based on the elevations of traversed cells and their distances to the viewing point (Figure 2.11) (Zhang et al., 2017). The sky view angle is computed along 16 directions equally spaced by 22.5 degrees (Figure 2.12). To select the traversed cells by the solar beam direction, a finite number of points is considered, starting from the centre of the initial cell (viewing point) (Figure 2.13). The coordinate of points is computed by summing the increment along east direction, Δx, and north direction, Δy, as:

$$\Delta x = \delta\ sin(B) \tag{2-36}$$

$$\Delta y = \delta\ cos(B) \tag{2-37}$$

where B is the azimuth and δ is the half of domain cell size.

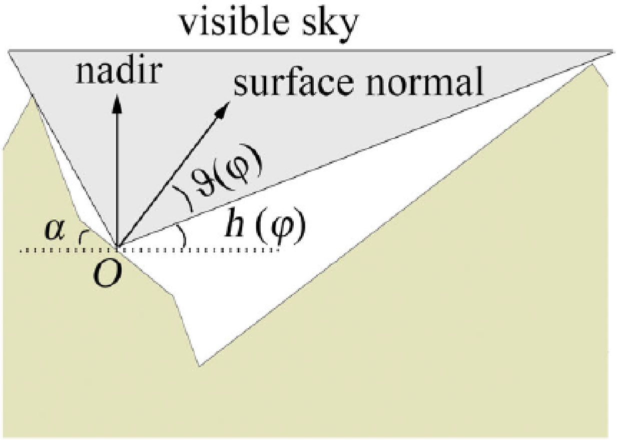

Figure 2.11 A cross section of a valley to sketch the visible sky area from a slope in the valley. h(φ) is the maximum horizontal viewing angle of terrain obstruction in azimuth φ. ϑ(φ) is the zenith angle to the slope normal of terrain horizon on a sloped coordinate system in azimuth φ. Adapted from Zhang et al., 2017.

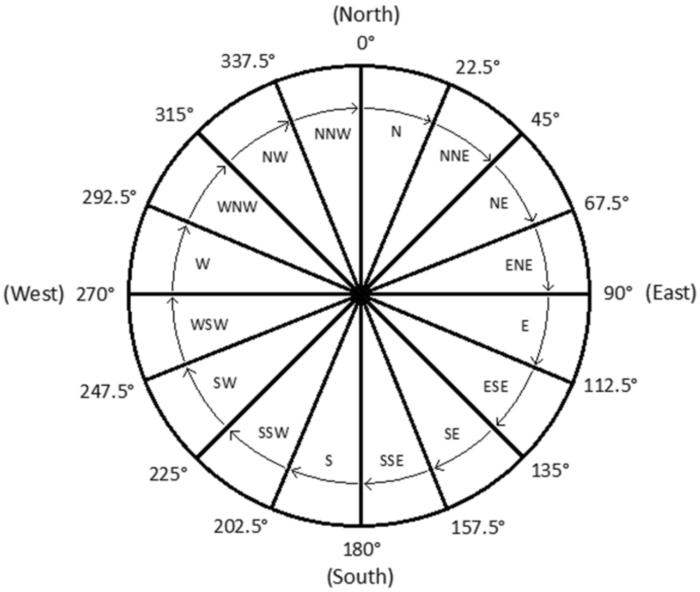
(North)
0°
22.5°
45°
67.5°
90° (East)
112.5°
135°
157.5°
180°
(South)
202.5°
225°
247.5°
(West) 270°
292.5°
315°
337.5°
N
NNE
NE
ENE
E
ESE
SE
SSE
S
SSW
SW
WSW
W
WNW
NW
NNW

Figure 2.12 The sixteen directions along which shy view angle is computed for each cell: (0.0, 22.5, 45.0, 67.5, 90.0, 112.5, 135.0, 157.5, 180.0, 202.5, 225.0, 247.5, 270.0, 292.5, 315.0, 337.5 degree)

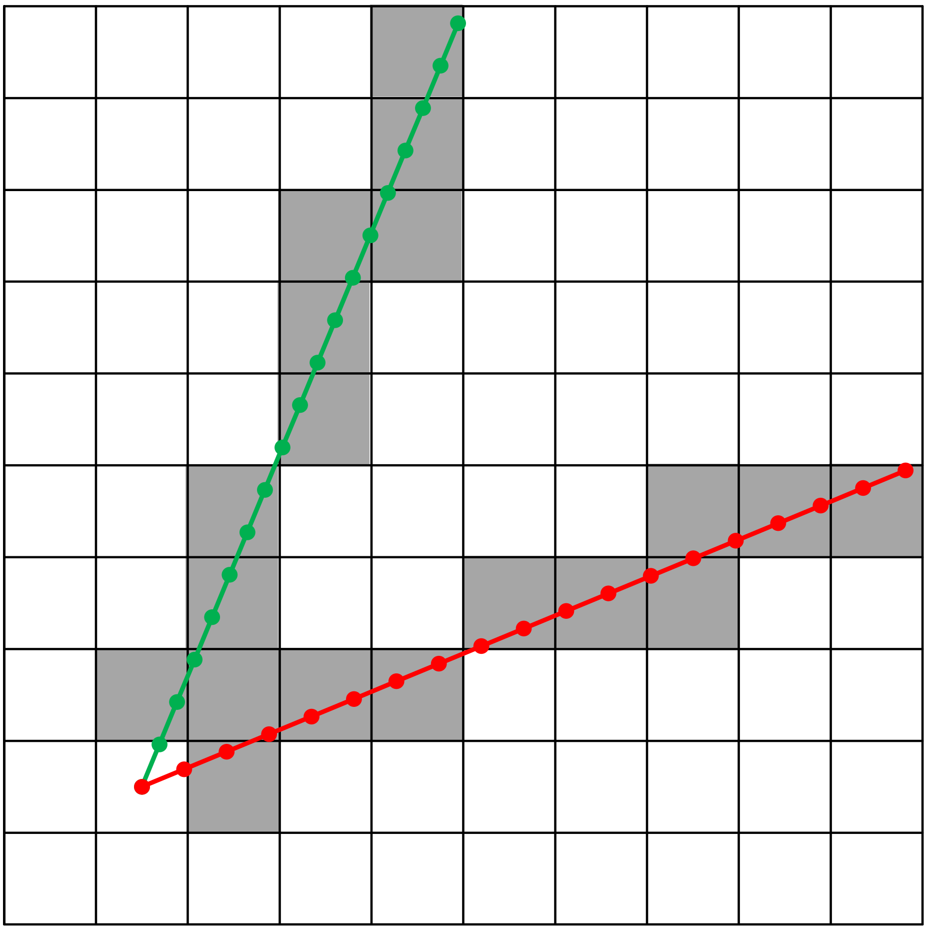

Figure 2.13 Traversed cells from the viewing point for 22.5° azimuth direction (green line), and 67.5° azimuth direction (red line). Points mark position of points computed as successive increment from the viewing point.

The angle, ω, between the point with maximum elevation in the direction of the solar beam, denoted by coordinates x_m, y_m, z_m, and the examined cell, denoted by coordinated x_0, y_0, z_0 (Figure 2.10):

$$\omega = arctg\left(\frac{z_m - z_0}{d_{m0}}\right) \tag{2-38}$$

where z_m and z_0 are terrain elevation (retrieved from digital elevation model) of the point with maximum elevation, *m*, and the viewing point, *0*, respectively, and d_{m0} is the distance between point *m* and point *0*.

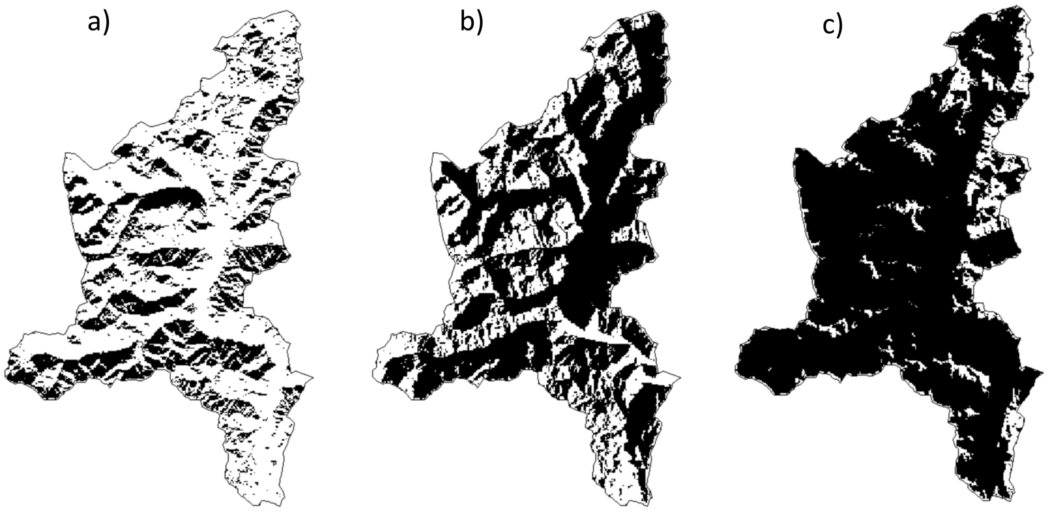

Figure 2.14 Shadow maps on the Toce river basin, Italy, for three different times: a) 2000-02-01T12:00:00+00:00, azimuth 180°, sun elevation 28°; b) 2000-02-01T08:00:00+00:00, azimuth 123°, sun elevation 7.6°; c) 2000-02-01T16:00:00+00:00, azimuth 233°, sun elevation 3°.

At every simulation time step, the current sun elevation and azimuth are computed as a function of the hour of day and day of year, and the closest direction out of the 16 ones is selectes. A map of shadowed pixels is computed comparing ω with sun elevation in each cell. If ω is higher than the sun elevation, the cell is shadowed and the incident short wave radiation is constituted by scattered and reflexed components only:

$$R_s = DF + A \tag{2-39}$$

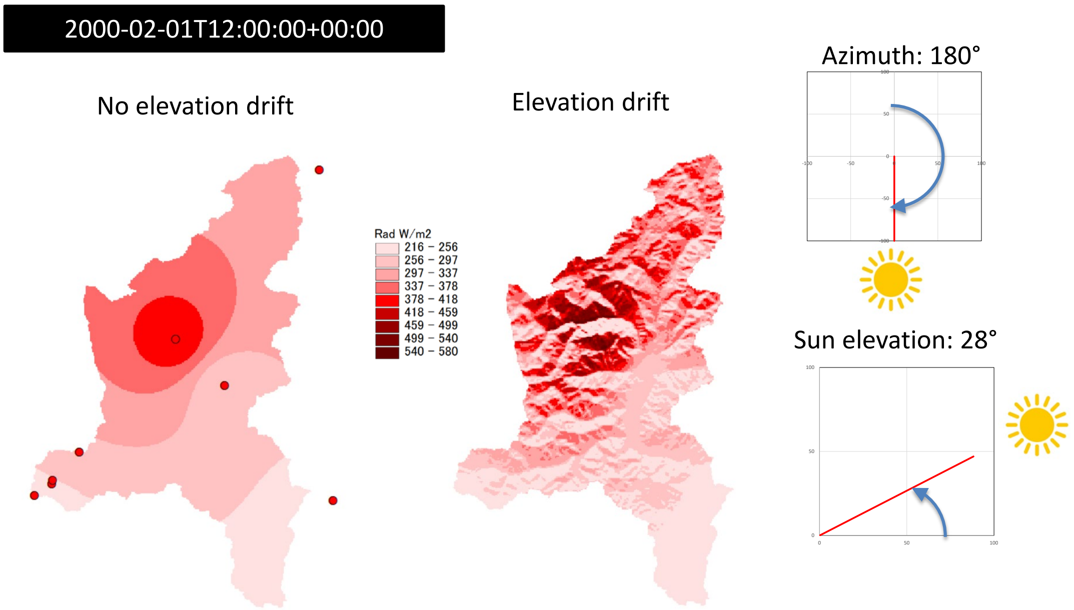
2000-02-01T12:00:00+00:00
No elevation drift
Elevation drift
Azimuth: 180°
Rad W/m2
216 – 256
256 – 297
297 – 337
337 – 378
378 – 418
418 – 459
459 – 499
499 – 540
540 – 580
Sun elevation: 28°

Figure 2.15 Shortwave radiation at 12:00 of 2000-02-01 on the Toce river, Italy, interpolated with inverse distance weighting without drift (left) and with elevation drift (right). Circles show stations where solar radiation was measured.

2.2.2 Longwave radiation

Bodies at terrestrial temperatures emit radiation with typically long wavelengths around 10 μm and in any case not exceeding 100 μm.

Although good instruments have become available for the measurement of longwave radiation, the measurement of this type of radiation is not simple and is rarely done; one reason for this is that any measuring instrument emits radiation of similar wavelengths and intensities to those it is supposed to measure.

To overcome the lack or the scarcity of longwave radiation measurements, it is necessary to estimate these data from proxy information. For this purpose, it is convenient to distinguish between long-wave radiation emitted by the earth's surface R_{ld} and long-wave radiation emitted by the atmosphere R_{lu}.

From the Stefan-Boltzmann equation, longwave radiation, R_l , can be written as:

$$R_l = \xi_s \, \sigma \, (T_s)^4 \qquad \text{2-40}$$

where:

ξ_s is emissivity of body surface

σ is the Stefan-Boltzmann constant ($5.67 * 10^{-8}$ $Wm^{-2}K^{-4}$)
T_s is the body surface temperature (K)

The Stefan-Boltzmann equation requires the temperature of the body's surface, a measure that is rarely available. Using the air temperature as alternative to surface body temperature can lead to a non-negligible error.
Alternatively the long-wave radiation can be estimate without measuring the surface temperature with an expression like (Wales-Smith, 1980):

$$R_{ld} - R_{ln} = -\sigma \left(T_a + 273.15\right)^4 \left(0.56 - 0.079\sqrt{e_a}\right) \left(0.1 + 0.9\, cl\right) \qquad 2\text{-}41$$

where
T_a is the air temperature (degree Celsius)
e_a is the actual vapor pressure (Kpa), computed as:

$$e_a = e_s(RH/100) \qquad 2\text{-}42$$

where RH (%) is the air relative humidity and e_s (Kpa) is the sature vapor pressure computed as a function of air temperature:

$$e_s = 0.6108\, exp\, \left(\frac{17.27\, T_a}{T_a + 237.3}\right) \qquad 2\text{-}43$$

cl is the shadow factor computed as the complement to clearness factor, k_t (Liu and Jordan, 1960):

$$cl = 1 - K_t \qquad 2\text{-}44$$

2.3 Air temperature with lapse rate

Air temperature is an important input to a variety of spatially distributed hydrological and ecological models. These models use air temperature to drive processes such as evapotranspiration, snowmelt, soil decomposition, and plant productivity (Dodson and Marks, 1997). Since most near-surface air temperature data are collected at irregularly spaced point locations rather than over continuous surfaces, the point-based temperatures must be accurately distributed over the landscape in order to be useful in spatially distributed modeling.

In mountainous terrain, the strong relationship between temperature and elevation precludes a simple interpolation of point-based temperature observations. Unless the effect of elevation on temperature is explicitly accounted for, an interpolation of temperature can produce grossly inaccurate results.

An additional problem with point-based temperature data is that the locations of meteorological stations tend to be biased toward lower elevations. Highelevation regions are represented poorly by the spatial distribution of most meteorological station networks (Robeson 1995).

The main difficulty in accurately interpolating temperature data in mountainous terrain is the effect of elevation on temperature. Mountains, acting as physical barriers, force air to move vertically, a process called *orographic uplift*. When an air parcel rises, it expands and cools. If no heat is exchanged with the outside system, this cooling is termed adiabatic. The rate at which air cools with elevation change, the lapse rate, varies from about -9.8°C km^{-1} for dry air (the dry adiabatic lapse rate) to about -4.0°C km^{-1} for very warm saturated air (the saturated adiabatic lapse rate) (Barry & Chorley 1987, p. 76). The lapse rate is seldom purely adiabatic due to outside heat exchange caused by radiational heating or cooling at the surface, horizontal mixing (advection) of air masses, and evaporation or condensation of moisture. The actual lapse rate at a given place and time is termed the environmental lapse rate. A typical value used for the global mean environmental lapse rate is -6.5°C km^{-1} (Barry & Chorley 1987, p. 56).

The FeST model implements an interpolation algorithm to account for air temperature vertical lapse rate (Figure 2.16):

(1) air temperature, T_m, measured at elevation z_m, is transformed to air temperature, T_r on a reference elevation, z_r, keeping into account a fixed thermal lapse rate, γ

$$T_r = T_m + (z_r - z_m)\,\gamma \qquad \text{2-45}$$

(2) data at reference elevation are interpolated using one of the methods implemented (Thiessen IDW, OK) to fill in all cells of the simulated domain

(3) in each cell of the simulation domain, air temperature at reference elevation is transformed back to air temperature, T_g , at elevation retrieved from digital elevation model, z_{dem}, keeping into account a fixed thermal lapse rate

$$T_g = T_r - (z_r - z_{dem})\,\gamma \qquad \text{2-46}$$

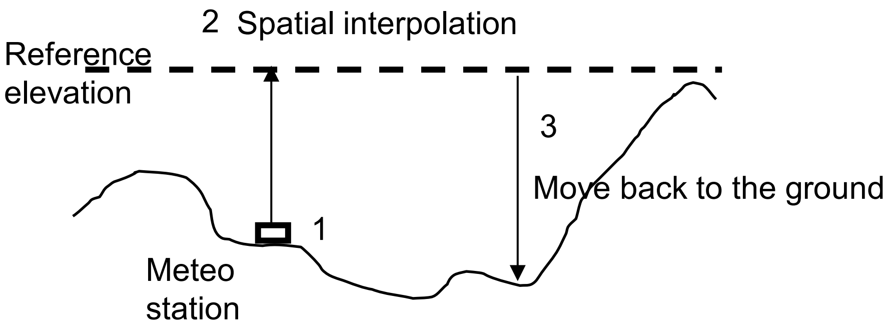
2 Spatial interpolation
Reference elevation
3
Move back to the ground
1
Meteo station

Figure 2.16 Schematic of the air temperature interpolation considering a vertical lapse rate and elevation drift.

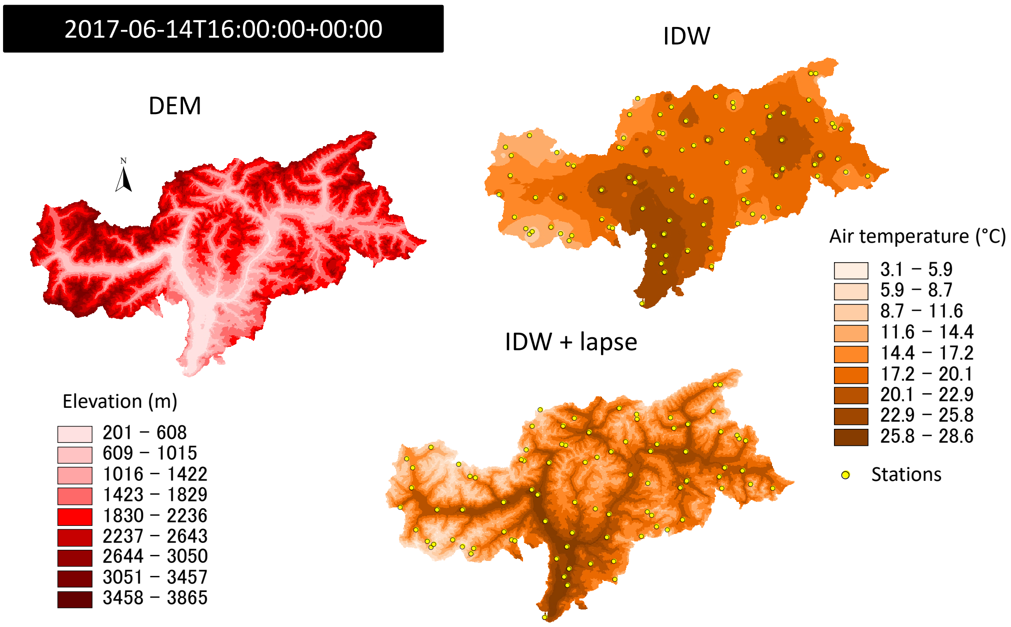
2017-06-14T16:00:00+00:00
DEM
N
IDW
IDW + lapse
Elevation (m)
201 – 608
609 – 1015
1016 – 1422
1423 – 1829
1830 – 2236
2237 – 2643
2644 – 3050
3051 – 3457
3458 – 3865
Air temperature (°C)
3.1 – 5.9
5.9 – 8.7
8.7 – 11.6
11.6 – 14.4
14.4 – 17.2
17.2 – 20.1
20.1 – 22.9
22.9 – 25.8
25.8 – 28.6
Stations

Figure 2.17 Air temperature at 16:00 of 2017-06-14 on the Bolzano province, Italy, interpolated with inverse distance weighting without drift (IDW) and with elevation drift with lapse rate = -6.5 °C/km (IDW+lapse). Digital elevation model on the left.

Air temperature vertical lapse rate is assigned as a constant value. It can be assigned as a fixed scalar constant in time and space for the whole domain or as a raster map that may vary with time (by assigning a netCDF multidimensional map).

Optionally the lapse rate can be automatically computed at every simulation time step by a linear regression between the vector of measured air temperature data and vector of station elevation.

$$\gamma = \frac{\sum_{i=1}^{n}\left(z_m^i - \overline{z_m}\right)\left(T_m^i - \overline{T_m}\right)}{\sum_{i=1}^{n}\left(z_m^i - \overline{z_m}\right)^2} \qquad \text{2-47}$$

where n is the total number of available stations, and the upper line denotes average operator. While air temperature lapse rate is computed, the square of the correlation coefficient, R^2, is computed as well

$$R^2 = \frac{\left[n\sum_{i=1}^{n}\left(z_m^i\, T_m^i\right) - \sum_{i=1}^{n}\left(z_m^i\right)\ \sum_{i=1}^{n}\left(T_m^i\right)\right]^2}{\left\{n\sum_{i=1}^{n}\left(z_m^i\right)^2 - \left[\sum_{i=1}^{n}\left(z_m^i\right)\right]^2\right\}\left\{n\sum_{i=1}^{n}\left(T_m^i\right)^2 - \left[\sum_{i=1}^{n}\left(T_m^i\right)\right]^2\right\}} \qquad \text{2-48}$$

A minimum value of R^2 can be set so that when actual value is below the threshold value, a fixed lapse rate value is used to interpolate air temperature. The following figure shows air temperature observations on the Bolzano province, Italy, plotted against station elevation, for two time step. The example on the left is of a time step where observations are strongly linearly correlated to elevation. The example on the right is of a time step where the correlation is very weak, due to thermal inversion phenomena very frequent in Alpine region during winter.

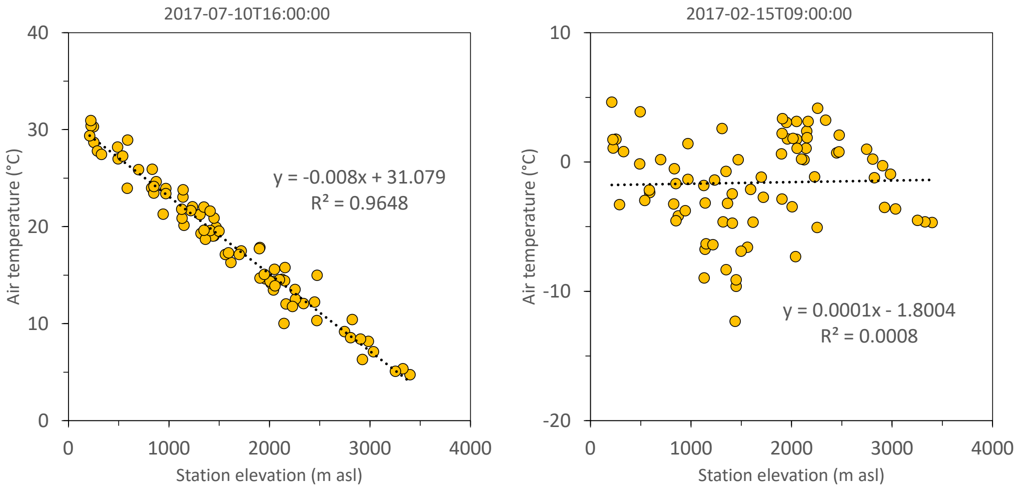

Figure 2.18 Air temperature observations on the Bolzano province, Italy, plotted against station elevation, for two time step. Dotted line shows regression line. Linear regression equation and R2 metric are shown. The example on the left is of a time step where observations are strongly linearly correlated to elevation. The example on the right is of a time step where the correlation is very weak, due to thermal inversion phenomena very frequent in Alpine region during winter.

Box 2.B Using lapse rate improves temperature interpolation

To verify the effect of the temperature lapse rate on the interpolation of the temperature data, a jackknife cross validation was applied considering the temperature measurements from 2016 to 2019 in the Bolzano province, Italy. At each hour, in turn, the data measured at a station was removed and the remaining measurements were interpolated to reconstruct the removed data, iteratively for all the available stations. For each hour the root mean square error was calculated between the observed data and those reconstructed with interpolation. The procedure was repeated considering: interpolation without lapse rate, interpolation with standard lapse rate (-0.0065 °C m^{-1}), and interpolation with lapse rate updated hourly from the linear regression of the observed data with respect to the altitude. Results are shown in the two figures on a monthly scale. It is noted that only in the period April-July the lapse rate calculated from data is comparable to the standard gradient, while the value of the calculated lapse rate decreases (in absolute value) significantly in the remaining months of the year with a minimum in December equal to - 0.0037 °C m^{-1}. The value of R^2 of the linear regression is relatively high (> 0.8) in the period between March and September, while it decreases in the rest of the year, due to the thermal inversion phenomenon, frequently occurring in autumn and winter, which causes a significant deviation from the linear trend of temperature with altitude. Figure (right) shows the monthly average results of the cross validation. We note how the interpolation that updates the lapse rate at each step shows a lower error in all months compared to considering the standard lapse rate or not considering a lapse rate in the interpolation.

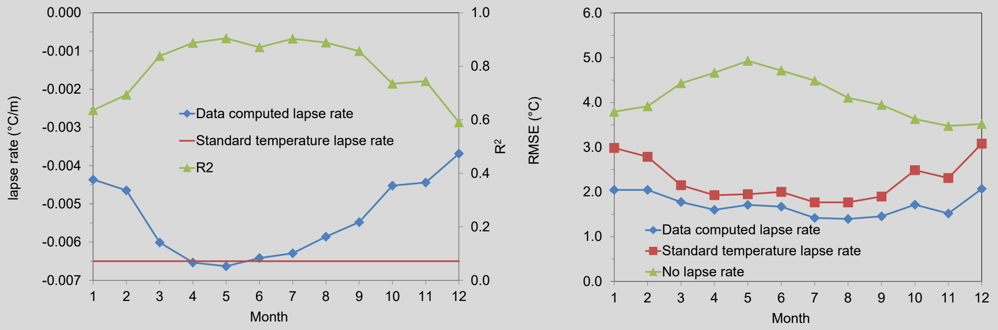

Monthly air temperature lapse rate computed from linear regression of observations and related R^2 compared to standard lapse rate (left), and monthly average root mean square error (*RMSE*) re-sulting from interpolation jackknife cross validation considering no lapse rate, standard lapse rate and lapse rate computed from data (right).

2.4 Precipitation with lapse rate

There is generally a limited number of rain gauges at high elevations due to the difficulties of installing and maintaining them. Even when there are stations, the precipitation measurement is often affected by significant errors, especially in the winter period caused by the presence of wind and by the malfunctioning of the heating system for snowfall melting. Precipitation in the Alps generally follows an increasing trend with elevation. Reconstructing a precipitation field considering only the measurements available at lower altitudes leads to an underestimation of the total precipitation volume (Avanzi et al., 2021). It is therefore crucial to evaluate the precipitation lapse rate to be used in spatial interpolation, including the measurements at the highest elevations (Corbari et al., 2022).

The FeST model implements an interpolation algorithm to account for precipitation vertical lapse rate that follows the same approach implemented for air temperature (Figure 2.16):

(1) Precipitation, P_m (mm), measured at elevation z_m (m), is transformed to precipitation, P_r (mm) on a reference elevation, z_r (m), keeping into account a lapse rate, γ (mm/h/m), integrated over a time step, Δt (h)

$$P_r = P_m + (z_r - z_m)\,\gamma\,\Delta t \qquad \text{2-49}$$

(2) data at reference elevation are interpolated using one of the methods implemented (Thiessen IDW, OK) to fill in all cells of the simulated domain

(3) in each cell of the simulation domain, precipitation at reference elevation is transformed back to precipitation, P_g , at elevation retrieved from digital elevation model, z_{dem}, keeping into account the lapse rate integrated in the time step, Δt (h)

$$P_g = P_r - (z_r - z_{dem})\,\gamma\,\Delta t \qquad \text{2-50}$$

Lapse rate can be assigned as a fixed scalar for the whole domain or as a raster map that may vary with time (by assigning a netCdf multidimensional map).

2.5 Wind speed over complex topography

Wind speed data are fundamental for evapotranspiration assessment in hydrological studies (Ravazzani et al., 2012). For application to large river basins, characterized by a limited number of available wind observation sites, data interpolation becomes necessary to estimate wind spatial variability (Cheng and Georgakakos, 2011). However, in complex topography areas, interpolation is made difficult because of spatial variation in wind velocity caused by slopes, canyons or valleys, and of the sheltering and diverting effects of terrain (Ryan, 1977; Rotach et al., 2015). Proposed methods for the wind field interpolation can be summarized as (Liston and Sturm, 1998): 1) applying a physically based numerical weather prediction model which satisfies all relevant momentum and continuity equations (Ercolani et al., 2015); 2) applying an atmospheric model in which only mass continuity is satisfied (Wagenbrenner et al., 2016); 3) interpolating wind-speed and direction observations in conjunction with empirical wind-topography relationships (Ryan, 1977).

Numerical weather prediction models have been run successfully for specific test cases that implies specialized model configurations and requires technical expertise and access to computing resources (Helbig et al., 2017).

Mass conserving models have been applied to small scale high spatial resolution domain and, even though less demanding than numerical weather models, they still require substantial resources when applied to larger scales (Forthofer et al., 2014).

For long-run simulations of hydrological processes in large river basins, simple empirical models are preferable in order to limit simulation time (Ravazzani et al., 2014).

In FeST models two options are implemented to constrain wind speed interpolation to topography:

- The MicroMet model by Liston and Elder (2006);
- The method presented by González-Longatt et al. (2015).

Box 2.C Convention for wind speed direction

Meteorologists and oceanographers describe the flow of wind differently. **Oceanographers** prefer to describe wind in terms of the “direction of mass flow” or in other words the direction **towards which** the wind is blowing. In the oceanographic convention, wind flowing from the south to the north is symbolized by an arrow pointing north. **Meteorologists** (and **hydrologists**) use an arrow or a special symbol called a wind barb to show the direction **from which** the wind is blowing. The head of the arrow or wind barb points in the direction from which the wind is blowing. In the meteorological convention, a wind blowing from west to east is symbolized by an arrow pointing west.

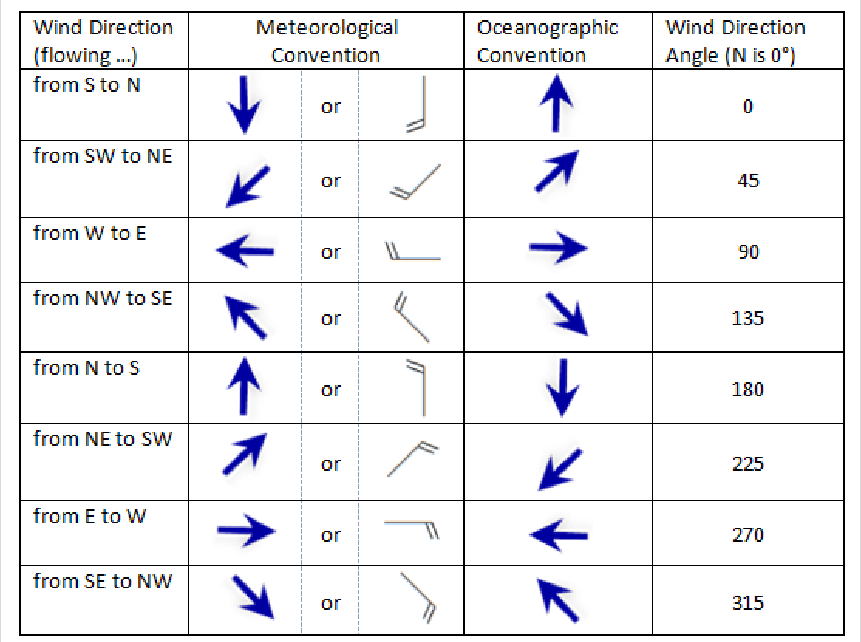

Wind Direction (flowing ...)	Meteorological Convention	Oceanographic Convention	Wind Direction Angle (N is 0°)
from S to N	↓ or	↑	0
from SW to NE	↙ or	↗	45
from W to E	← or	→	90
from NW to SE	↖ or	↘	135
from N to S	↑ or	↓	180
from NE to SW	↗ or	↙	225
from E to W	→ or	←	270
from SE to NW	↘ or	↖	315

Meteorological and oceanographic conventions to display wind direction. Source: https://www.esri.com/arcgis-blog/products/product/analytics/displaying-speed-and-direction-symbology-from-u-and-v-vectors/.

2.5.1 The MicroMet model

Observed values of wind speed W (m s^{-1}) and direction θ are first converted into zonal u (m s^{-1}) and meridional v (m s^{-1}) wind components using:

$$u = -W \sin\theta \qquad \text{2-51}$$

$$v = -W \cos\theta \qquad \text{2-52}$$

Then, u and v components are independently interpolated to a regular grid using the IDW. The resulting values are converted back to wind speed using:

$$W = \sqrt{u^2 + v^2} \qquad \text{2-53}$$

These gridded values are then modified to account for topographic variations, multiplying by an empirically based weighting factor, W_w,

$$W_w = 1 + \gamma_s \Omega_s + \gamma_c \Omega_c \tag{2-54}$$

where Ω_c is the topographic curvature:

where Ω_s is the topographic slope in the direction of the wind, Ω_c is the topographic curvature, and γ_s and γ_c are positive constants which weight the relative influence of Ω_s and Ω_c on modifying the wind speed.

The curvature, Ω_c, is computed at each model grid cell by first defining a curvature length scale or radius, $\boldsymbol{\eta}$ (m), that defines the topographic length scale to be used in the curvature calculation. This length scale is equal to approximately half the wavelength of the topographic features within the domain (e.g., the distance from a typical ridge to the nearest valley). Default value used by the FeST model for length scale is 5000 m.

For each model grid cell, the curvature is calculated by taking the difference between that grid cell elevation, and the average elevations of the two opposite grid cells a length scale distance from that grid cell. This difference is calculated for each of the opposite directions S–N, W–E, SW–NE, and NW–SE from the main grid cell (effectively obtaining a curvature for each of the four direction lines), and the resulting four values are averaged to obtain the curvature. Thus

$$\boldsymbol{\Omega_c} = \frac{1}{4}\begin{bmatrix} \dfrac{z-1/2(z_W+z_E)}{2\eta} + \dfrac{z-1/2(z_S+z_N)}{2\eta} + \\ \dfrac{z-1/2(z_{SW}+z_{NE})}{2\sqrt{2\eta}} + \dfrac{z-1/2(z_{NW}+z_{SE})}{2\sqrt{2\eta}} \end{bmatrix} \tag{2-55}$$

where z_W, z_{SE}, are the elevation values for the grid cell at approximately curvature length scale distance, η, in the corresponding direction from the main grid cell. The curvature is then scaled such that $-0.5 \leq \boldsymbol{\Omega_c} \leq < 0.5$ over the simulation domain.

The slope in the direction of the wind, Ω_s, is

$$\Omega_s = \beta \, cos(\theta - E) \qquad 2\text{-}56$$

This $\boldsymbol{\Omega_s}$ is also scaled such that $-0.5 \leq \boldsymbol{\Omega_s} \leq 0.5$ over the simulation domain.

The terrain slope, β, is given by

$$\beta = tan^{-1}\left[\left(\frac{\partial z}{\partial x}\right)^2 + \left(\frac{\partial z}{\partial y}\right)^2\right]^{1/2} \qquad 2\text{-}57$$

where z (m) is the topographic height, and x (m) and y (m) are the horizontal coordinates. The terrain slope azimuth, with north having zero azimuth, is

$$E = \frac{3\pi}{2} - tan^{-1}\left(\frac{\partial z/\partial y}{\partial z/\partial x}\right) \qquad 2\text{-}58$$

The terrain-modified wind speed, W_t (m s^{-1}), is calculated from:

$$W_t = W_w W \qquad 2\text{-}59$$

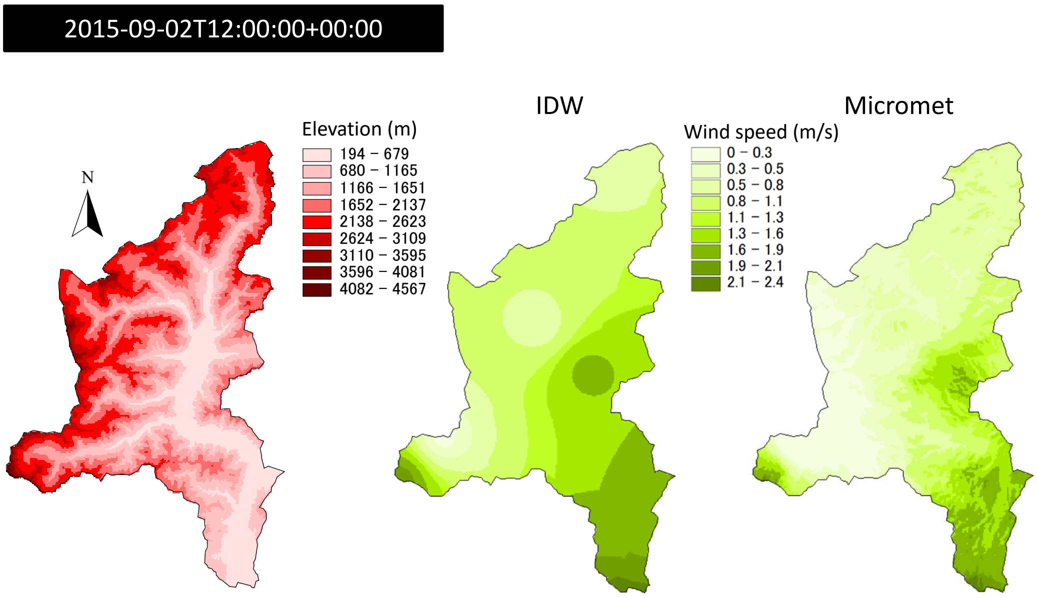
2015-09-02T12:00:00+00:00
N
Elevation (m)
194 – 679
680 – 1165
1166 – 1651
1652 – 2137
2138 – 2623
2624 – 3109
3110 – 3595
3596 – 4081
4082 – 4567
IDW
Micromet
Wind speed (m/s)
0 – 0.3
0.3 – 0.5
0.5 – 0.8
0.8 – 1.1
1.1 – 1.3
1.3 – 1.6
1.6 – 1.9
1.9 – 2.1
2.1 – 2.4

Figure 2.19 Wind speed at 12:00 of 2015-09-02 on the Toce river, Italy, interpolated with inverse distance weighting without drift (moddle) and with elevation drift (right). Digital elevation model on the left.

Box 2.D The Micromet method on the Upper Po river basin

Three spatial interpolation techniques – Thiessen, IDW, and Micromet – are evaluated on the upper Po river basin, in northern Italy. It covers 37200 km², of which 13700 km² (36.8%) have elevation higher than 1000 m (mountain), 10800 km² (29%) have elevation in the range 300 - 1000 m (hilly), and 12700 km2 (34.2%) lies below 300 m (flat).

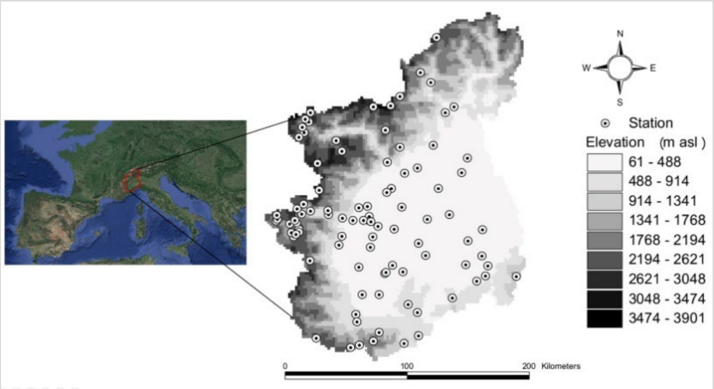
N
W
E
S
Station
Elevation (m asl)
61 - 488
488 - 914
914 - 1341
1341 - 1768
1768 - 2194
2194 - 2621
2621 - 3048
3048 - 3474
3474 - 3901
0
100
200 Kilometers

The Upper Po river basin elevation model and wind gauging stations.

Performance of methods to interpolate wind speed data was assessed in terms of ability to reproduce the output of the MOLOCH meteorological model (Malguzzi et al., 2006), considered as the benchmark solution. To this purpose, for each of the first 24 hours of daily MOLOCH run, the *u* and *v* wind components of all cells that include one monitoring station, were extracted and converted to wind speed and direction This procedure allowed to reconstruct a continuous time series of virtual wind speed and direction data for the 95 stations over the Upper Po river basin. When Micromet method was applied, the same elevation model implemented in the MOLOCH model was used. Therefore, an interpolation method perfectly performing should reproduce exactly the MOLOCH output.

Performance results in terms of normalised root mean square error (*NRMSE*) and the relative bias (*RB*) computed on three elevation ranges.

	whole basin		< 300 m		300-1000 m		>1000 m	
	NRMSE	*RB*	*NRMSE*	*RB*	*NRMSE*	*RB*	*NRMSE*	*RB*
THIESSEN	0.873	0.122	0.447	-0.027	0.748	0.076	1.151	0.290
IDW	0.669	0.060	0.390	-0.026	0.595	0.069	0.853	0.161
MICROMET	0.674	-0.093	0.414	-0.122	0.603	-0.104	0.842	-0.052

Results show that Micromet is able to increase the accuracy of wind speed interpolation only in the area where topography plays a relevant role (higher elevations). In other areas (as plain or hill), simple IDW is better than the other two methods. More details in Ravazzani et al., 2020.

2.5.2 The González-Longatt model

The orographic correction is used to modify the horizontal wind velocity components based on the elevation differences from the horizontally interpolated terrain elevations.

The orographic correction of both horizontal velocity components is determined by adding a correction calculated using the function f to the initially estimated velocity components u and v, see Eqs. (2-51) and (2-52), which result from the initial spatial interpolation of the measured wind speed datasets. The function f is consequently used in order to include a correction due to terrain orography and it can be justified based on both the conservation of mass and the conservation of momentum principles applied to a streamline (see Figure 2.20) where an increase in height Δh requires also an increase in velocity. The conservation of mass indicates that as the density decreases, as it is the case in atmospheric flows where all the state variables decrease with increasing altitude, the velocity must increase in order to maintain mass flow constant. Alternatively, the form adopted for the function f can be justified based on the conservation of momentum equation where the term $-\partial P/\partial x_i$ acts as a momentum sink if the pressure gradient increases in all spatial coordinates and as a source term if the pressure spatial gradient decreases as it is the case when the terrain altitude increases.

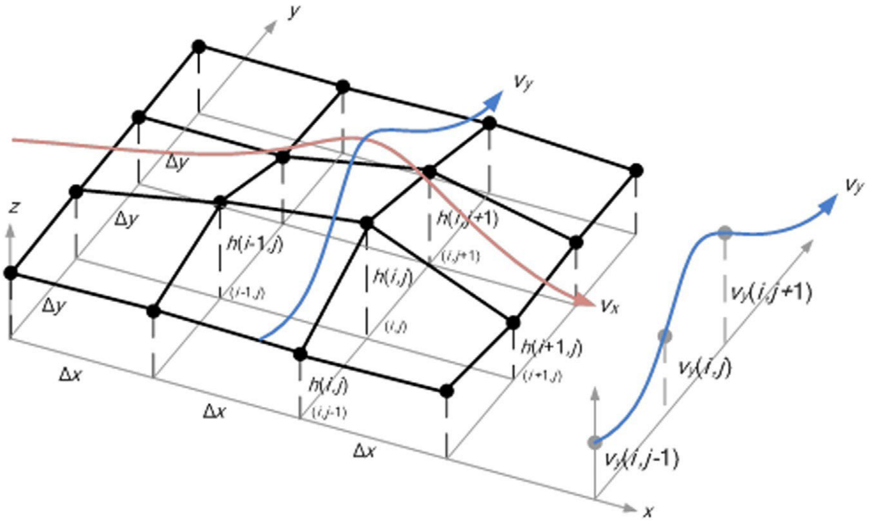

Figure 2.20 Schematic showing the horizontal discretization around an arbitrary grid point (i, j) at height h(i, j) whose velocity components v_x(i, j) and v_y(i, j) is calculated using the orographic correction. (*source*: González-Longatt et al. (2015))

However, for simplicity, the formulation of the function f assumes that pressure changes are linearly related to changes in height (Δh). Additionally, it is worth highlighting a favourable feature of the correction function f, that is, it is inversely proportional to the grid spacing (Δx). This has the effect of reducing the level of correction introduced by Eqs. (2-54) and (2-55) as the grid resolution is decreased which serves to minimise potential errors in the corrected wind velocity components for grids with insufficient or low density.

$$V_x^{calc} = V_x + f\left(\Delta h \frac{\Delta V_x}{\Delta x}\right) \qquad 2\text{-}60$$

$$V_y^{calc} = V_y + f\left(\Delta h \frac{\Delta V_y}{\Delta y}\right) \qquad 2\text{-}61$$

Finally, the orographic correction is implemented using a central difference calculation (see Figure 2.20) around the grid node for which the velocity is to be corrected and the corrected velocity components (V_x^{calc} and V_y^{calc}) are calculated using the equations

$$V_x^{calc} = V_x + \frac{1}{2}\left[\frac{\begin{array}{c}\left(h(i,j)-h(i-1,j)\right)\times\left(V_x(i-1,j)-V_x(i,j)\right)+\\ \left(h(i+1,j)-h(i,j)\right)\times\left(V_x(i,j)-V_x(i+1,j)\right)\end{array}}{\Delta x}\right] \qquad \text{2-62}$$

$$V_y^{calc} = V_y + \frac{1}{2}\left[\frac{\begin{array}{c}\left(h(i,j)-h(i,j-1)\right)\times\left(V_y(i,j-1)-V_y(i,j)\right)+\\ \left(h(i,j+1)-h(i,j)\right)\times\left(V_y(i,j)-V_y(i,j+1)\right)\end{array}}{\Delta y}\right] \qquad \text{2-63}$$

Wind vector components, V_x^{calc} and V_y^{calc} are composed to compute the final corrected wind speed value, $\boldsymbol{W}$

$$\boldsymbol{W} = \sqrt{(V_x^{calc})^2 + \left(V_y^{calc}\right)^2} \qquad \text{2-64}$$

2.6 Mixing methods

The usual method to interpolate station data relies on the same spatial interpolation method for the whole domain. As an option the *FeST* model implements a fully flexible system that allows to define zones of the simulation domain where different interpolation methods are applied.

Figure 2.21 shows an example of interpolation of precipitation measurements on the Toce river basin, Italy, assigning two different zones with *id* values 1 and 2 that corresponds to Thiessen and IDW interpolation methods, respectively. Figure 2.22 shows an example of spatial interpolation of wind speed data on the Toce river basin, Italy, using two methods: the IDW in zone with elevation lower than 2000 m a.s.l., and the Micromet method where elevation is greater than 2000 m a.s.l..

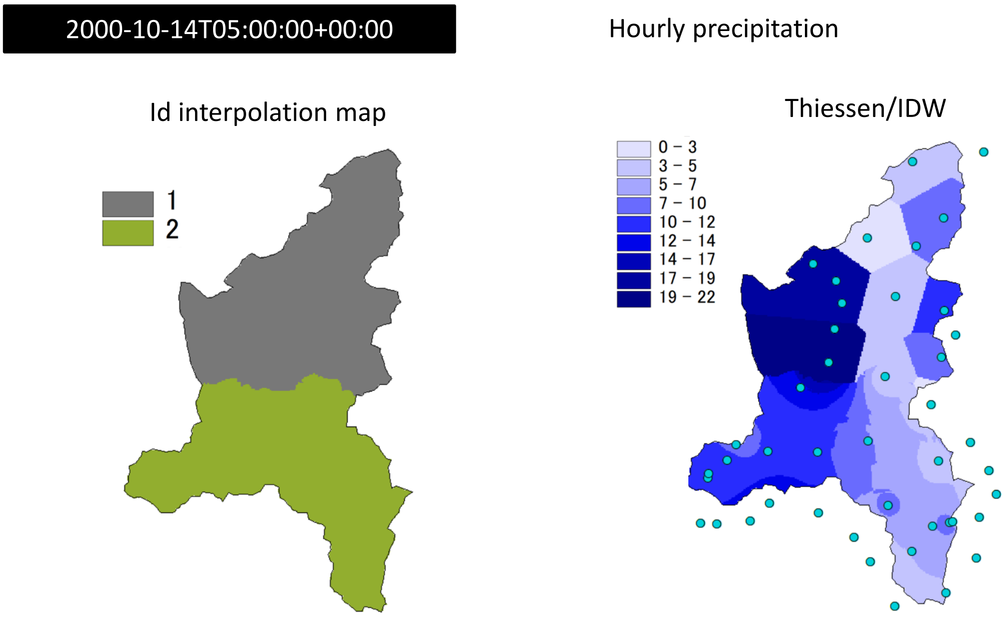
2000-10-14T05:00:00+00:00
Hourly precipitation
Id interpolation map
1
2
Thiessen/IDW
0 – 3
3 – 5
5 – 7
7 – 10
10 – 12
12 – 14
14 – 17
17 – 19
19 – 22

Figure 2.21 Example of interpolation of precipitation measurements on the Toce river basin, Italy, assigning two different zones (left) with id values 1 and 2 that corresponds to Thiessen and IDW interpolation methods, respectively. Final interpolated map is shown on the right.

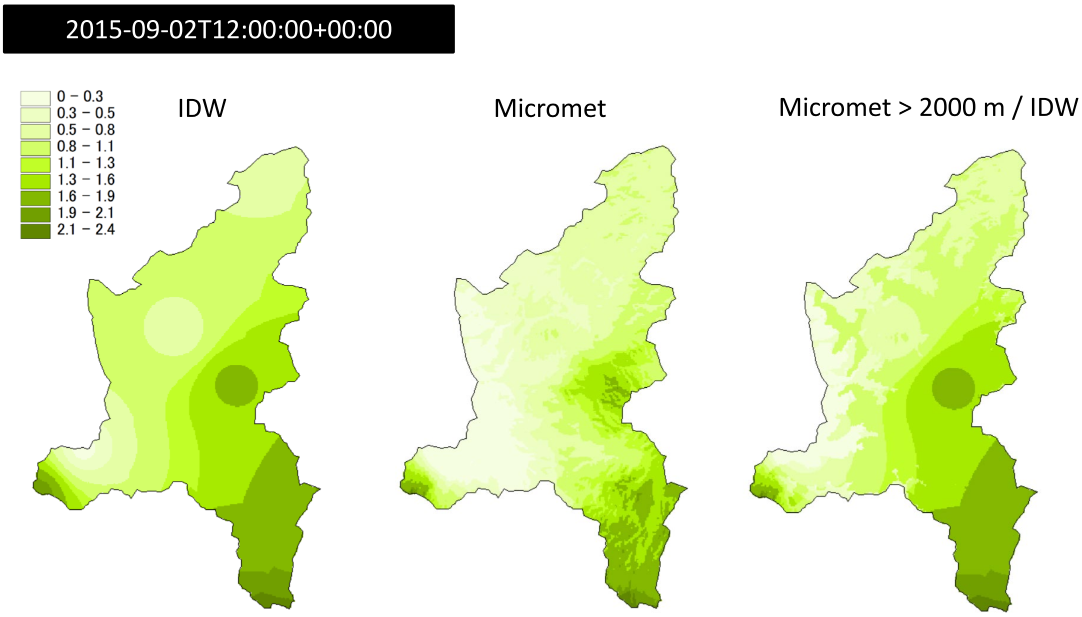
2015-09-02T12:00:00+00:00
0 – 0.3
0.3 – 0.5
0.5 – 0.8
0.8 – 1.1
1.1 – 1.3
1.3 – 1.6
1.6 – 1.9
1.9 – 2.1
2.1 – 2.4
IDW
Micromet
Micromet > 2000 m / IDW

Figure 2.22 Example of interpolation of wind speed data on the Toce river basin, Italy, using two methods: the IDW in zone with elevation lower than 2000 m a.s.l., and the Micromet method where elevation is greater than 2000 m a.s.l.. left map is obtained using only IDW, map in the middle is obtained using Micromet only, the right map is obtained with a mixing of the two methods.

2.7 Gridded meteorological data

When *FeST* is used for flood forecasting or climate change analysis purposes, the usual format of input data is multidimensional netCDF. Spatial reference system adopted by meteorological and climatic models that provide gridded datasets is usually geodetic (Figure 2.23). Spatial resolution is usually coarser than hydrological simulation resolution. Gridded data are converted to the proper reference system and spatially downscaled to the simulation grid resolution with nearest neighbour resampling method (Figure 2.24). This is a technique in which the value of each cell in an output raster is calculated using the value of the nearest cell in an input raster. Nearest neighbor assignment does not change any of the values of cells from the input layer. It preserves the original coarse grid structure, although the data is defined on a finer grid after resampling takes place.

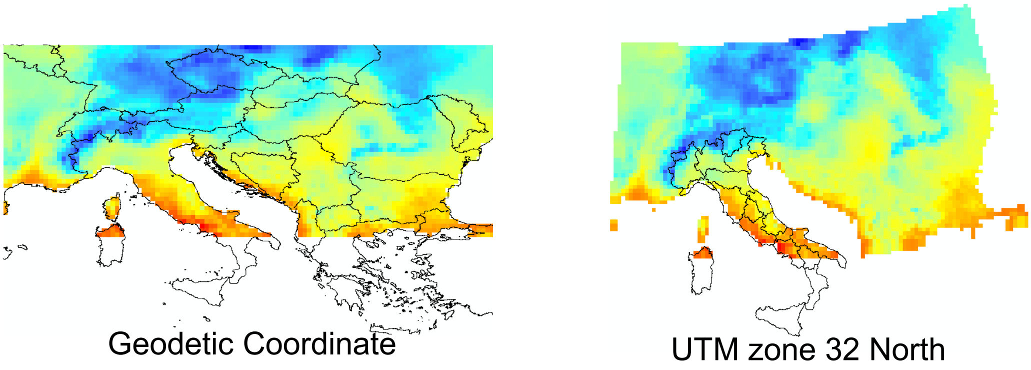

Figure 2.23 Example of spatial reprojection of temperature data from geodetic reference system to UTM 32N.

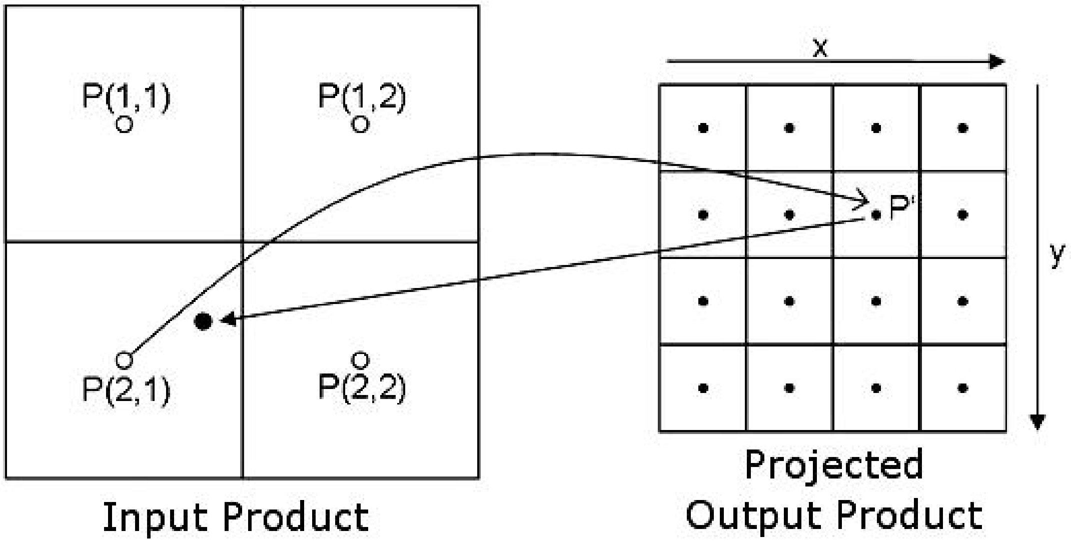
P(1,1)
P(1,2)
P(2,1)
P(2,2)
Input Product
x
y
P'
Projected
Output Product

Figure 2.24 Grid data resampling with nearest neighbour method. Source: https://www.brockmann-consult.de/beam/doc/help/general/ResamplingMethods.html

CHAPTER 3
CANOPY INTERCEPTION

Canopy interception is the rainfall that is intercepted by the canopy of a tree and successively evaporates from the leaves. Precipitation that is not intercepted will fall as throughfall or stemflow on the forest floor. Canopy interception can significantly affect infiltration, surface runoff, and evapotranspiration, and reduces the erosive energy of droplets.

The *FeST* model implements a model to simulate canopy interception that is derived from the *SWAT* model (*Gassman et al.*, 2007).

The amount of water that can be trapped in the canopy in a given time step, C_t, is given by:

$$C_t = C_{max} \frac{LAI}{LAI_{max}} \qquad 3\text{-}1$$

where C_{max} is the maximum amount of water that can be trapped in the canopy when the canopy is fully developed, LAI is the current leaf area index of a given day, and LAI_{max}, is the maximum leaf area index for the plant.

The actual amount of water stored in the canopy, C, is updated at each computational step, Δt, with the mass conservation equation:

$$C = C_i + (R - PE)\,\Delta t \qquad 3\text{-}2$$

Where C_i is the initial amount of water stored in the canopy, R is the rainfall rate, and PE is the potential evapotranspiration rate.

When canopy storage is filled to the maximum value, C_t, the excess rainfall amount is allowed to reach the ground as throughfall, T.

Canopy affects only fraction of ground surface covered by vegetation, so the effective rainfall that reach the ground, R_{eff}, is computed as:

$$R_{eff} = f_v\,T + (1 - f_v)\,R \qquad \text{3-3}$$

where f_v is the fraction of cell covered by vegetation.

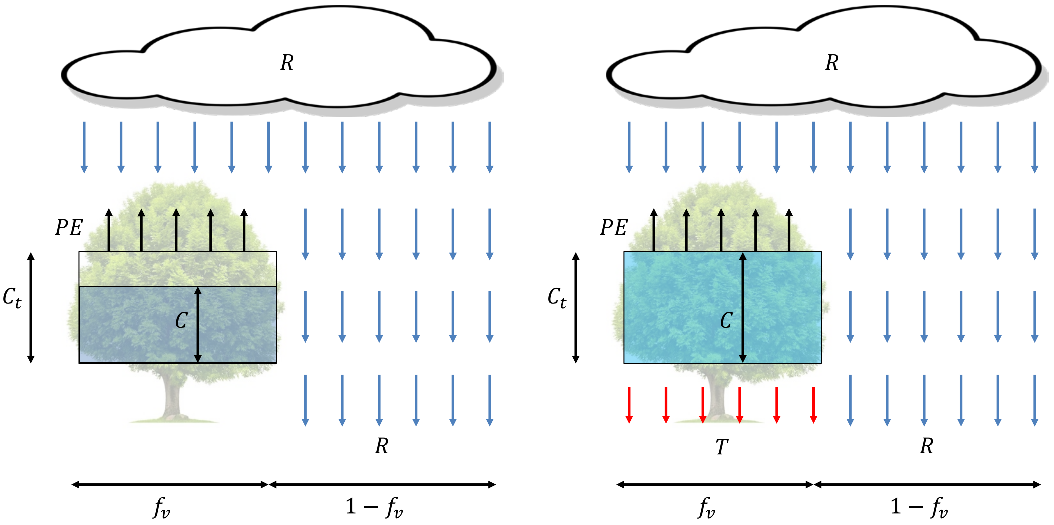

Figure 3.1 Rainfall is stored in the canopy until the maximum value at a given time, C_t, is reached (left). When C_t is reached, the excess rain reaches the ground as throughfall, T (right).

CHAPTER 4

SNOW ACCUMULATION AND MELTING

The snow module of *FeST* includes snow melt and snow accumulation simulation. The partitioning of total precipitation, P, in liquid, P_l, and solid, P_s, phase is a function of air temperature, T_a (Tarboton *et al.*, 1994):

$$P_l = \alpha_P P \tag{4-1}$$

$$P_s = (1 - \alpha_P)P \tag{4-2}$$

where α_P is computed by:

$$\alpha_p = \begin{cases} 0 & if \quad T_a \leq T_{low} \\ 1 & if \quad T_a \geq T_{up} \\ \frac{T_a - T_{low}}{T_{up} - T_{low}} & if \quad T_{low} < T_a < T_{up} \end{cases} \tag{4-3}$$

where T_{low} and T_{up} are air temperatures below/above which all precipitation falls as snow/rain, respectively.

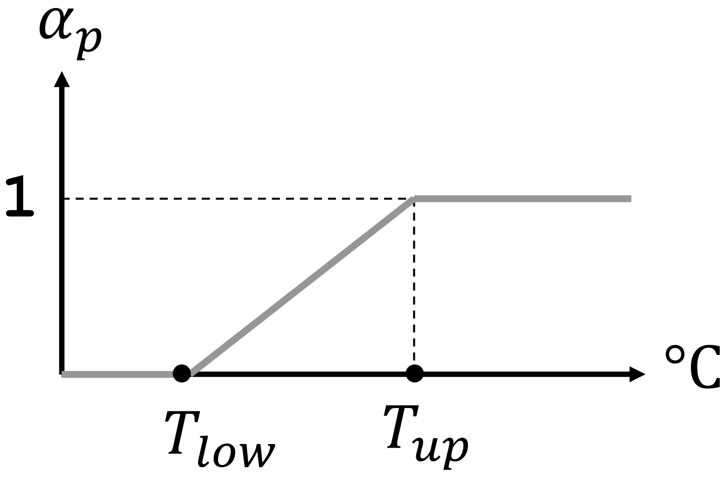

Figure 4.1 Coefficient of precipitation partitioning, α_p, in liquid and solid phase

The snow melt simulation is based on the degree day concept (Martinec *et al.*, 1960). The melt rate in m/s, M_s, is proportional to the difference between air temperature and a predefined threshold temperature, T_b:

$$M_s = \begin{cases} C_m(T_a - T_b) & if \quad T_a > T_b \\ 0 & if \quad T_a \le T_b \end{cases} \qquad 4\text{-}4$$

where C_m (m °C^{-1} s^{-1}) is an empirical coefficient depending on meteorological conditions and geographic location.

The mass conservation equation, integrated over duration Δt , defines the actual snow water equivalent, SWE, stored in each cell:

$$SWE = (P_s - M_s)\,\Delta t \qquad 4\text{-}5$$

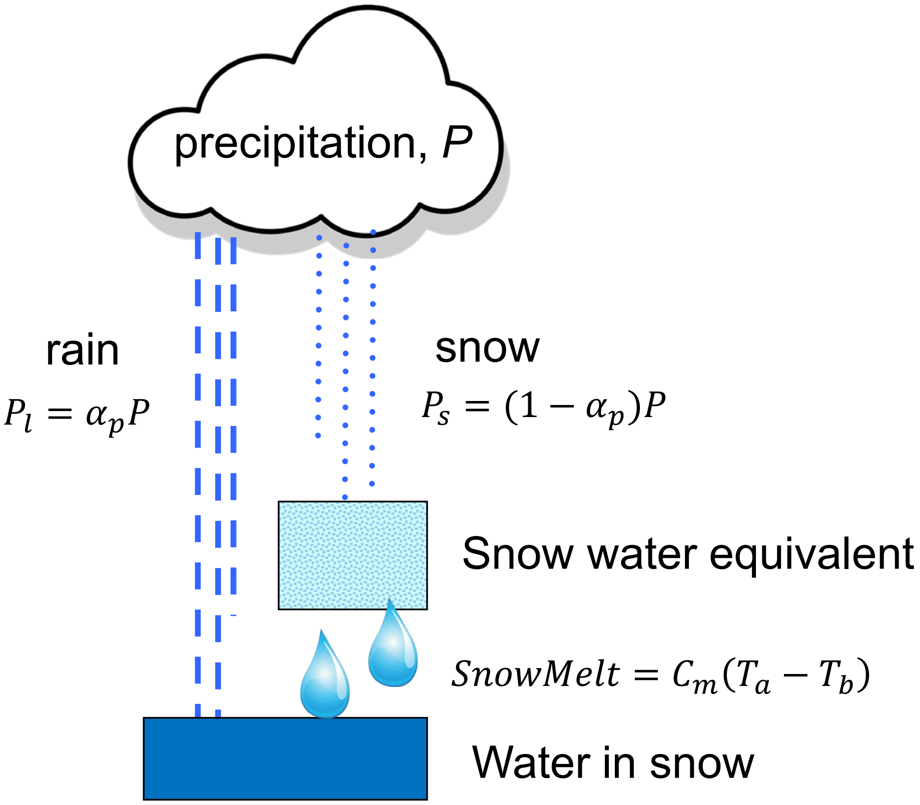
precipitation, P
rain
$P_l = \alpha_p P$
snow
$P_s = (1 - \alpha_p)P$
Snow water equivalent
$SnowMelt = C_m(T_a - T_b)$
Water in snow

Figure 4.2 Snow accumulation and melting contribute to the updating of snow water equivalent (*SWE*) and water stored within snowpack.

The terrain covered by snow is supposed to be frozen and hence the melted water is prevented from infiltrating into the soil. Conversely, the liquid fraction of snow water equivalent, R_s, sum of melted water and liquid precipitation, forms the second state variable computed by the snow module:

$$R_s = (P_l + M_s)\,\Delta t \qquad \text{4-6}$$

R_s is supposed to flow cell by cell through the snow pack with the *Darcy* equation, following the flow direction derived from digital elevation model, with a snow conductivity, k_{snow}, of 1.67 10^{-3} m/s (*Salandin et al.*, 2004).

$$Q_{snow} = k_{snow}\ R_s\,\Delta x\, i \qquad \text{4-7}$$

where Q_{snow} is the flux of R_s flowing from cell to cell, Δx is the cell size, and i is the local topographic slope.

When R_s reaches a cell not covered by snow, or snow melts totally in the time step, it is treated as an input term in the soil balance of that cell.

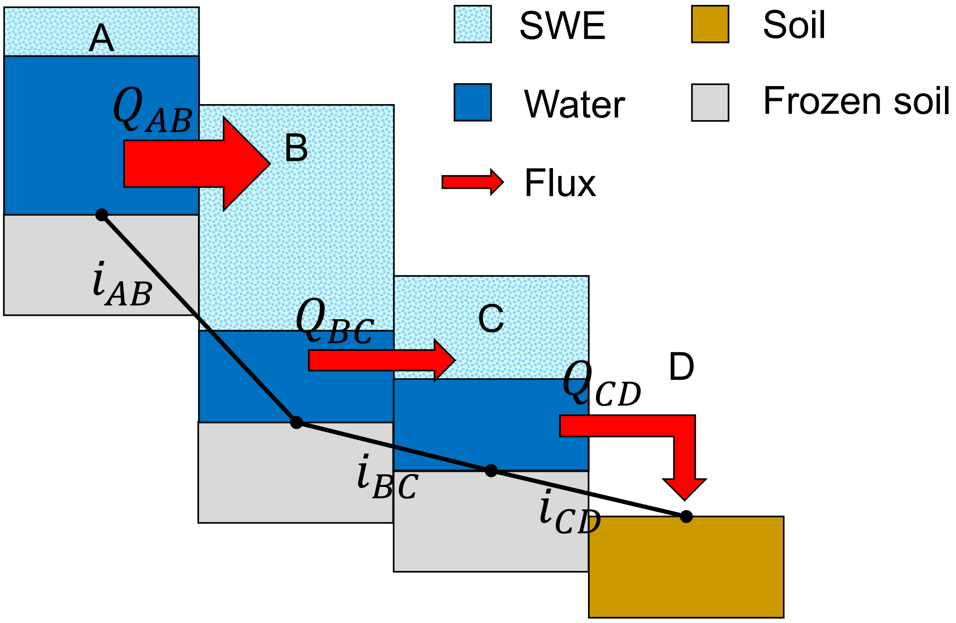

Figure 4.3 Cells are connected by a lateral flux that transfers water accumulated within snowpack following the flow direction derived from digital elevation model. Flux magnitude is computed with *Darcy* equation and depends from actual water amount and local terrain slope. When lateral fluxes meets a cell not covered with snow (D), it is treated as a source term in the soil water balance.

CHAPTER 5

GLACIER ACCUMULATION AND ABLATION

Glaciers are known to have a significant impact on stream flow runoff: they store water during winter season, while, during summer, melt water may provide the only source of water for some Alpine valley; they therefore play an important role on the river flow regimes with peaks of melting during the middle-late summer (*Hock*, 2003; *Hock et al.*, 2005; *Milner et al.*, 2009). The structure and space-time dynamic of a glacier is very complex; for this reason, representing in a rigorous manner the glacier dynamic within an hydrological model requires numerous input data and onerous computational time, which makes it difficult to apply to complex and extended drainage basins (*Huss et al.*, 2008).

Several approaches exist to model glacier dynamic within hydrological models, as well as different methods exist to simulate melt and accumulation of ice. Ice melt models can be grouped in two main categories: the energy balance models and the temperature-index models (*Hock*, 2003); the first type of models has a strong physical basis because each of the relevant energy fluxes at the glacier surface is computed using direct measurement of meteorological variables and thus allows to obtain melt rates with high precision and with high temporal resolution; in the second type of models melt rate is calculated from empirical formulas. However, despite the simplicity of the temperature-index models, they are commonly used because of the wide availability of temperature data and the lower computational cost; furthermore, Hock (*Hock*, 2003) highlighted the physical basis of such kind of models. In more detailed models, accumulation is modelled taking into account snow, firn, and ice and the spatial redistribution of snow due to drift and avalanches (Huss et al., 2008); in conceptual models, accumulation of ice is not often taken into account because they typically starts from an infinite volume of ice or consider glaciers area constant in time (*Klock et al.*, 2001); otherwise, they simply solve the mass balance between solid precipitation, snow melt and glacier melt (*Schaefli et al.*, 2005; *Horton et al.*, 2006; *Konz and Seibert*, 2010).

The glaciers module implemented within the *FeST* model is aimed at simulating the contribution of glacier melt to runoff for middle-size to large basins. The glaciers module is simple in structure but without losing the raster based approach of the whole model. The glacier model requires few input data (glaciers area, DEM, temperature, and precipitation) and is able to reproduce melting, with a simple temperature index melt model, accumulation and propagation of melt water into ice, in a way similar to snow simulation (see Chapter 4).

The module assumes that glaciers form a layer between the ground, below, and snowpack, above. When a snowpack layer is present above glacier, it protects ice from ablation and intercepts rainfall. When glacier is free from snow, the ice melt rate in m/s, M_{ice}, is proportional to the difference between air temperature, T_a , and a predefined threshold temperature, $T_{b,ice}$:

$$M_{ice} = \begin{cases} C_{m,ice}(T_a - T_{b,ice}) & if \quad T_a > T_{b,ice} \\ 0 & if \quad T_a \leq T_{b,ice} \end{cases} \qquad 5\text{-}1$$

where $C_{m,ice}$(m °C^{-1} s^{-1}) is an empirical coefficient depending on ice conditions and geographic location. The values of $C_{m,ice}$ vary from a minimum of $5.79 \cdot 10^{-8}$ m/°C·s to a maximum of $2.31 \cdot 10^{-7}$ m/°C·s. (*Shaefli et al.*, 2005).

The accumulation model for the glaciers is based on annual mass balance (*Huss et al.*, 2008; *Horton et al.*, 2006): it is determined by comparing the solid precipitation accumulated and the amount of snow melted by the end of the hydrological year. So, the volume of snow that has not melted by a given date, is converted into ice. The date when snow to ice conversion takes place can be set by the user, and it is usually set to September 1st.

The melted ice is stored as liquid fraction within the ice pack, R_{ice}. Liquid precipitation, P_l contributes to R_{ice} when glacier is not covered with snow.

R_{ice} is supposed to flow cell by cell through the snow pack with the *Darcy* equation, following the flow direction derived from digital elevation model, even when glacier is covered with snow.

$$Q_{ice} = k_{ice} \ R_{ice} \, \Delta x \, i \qquad 5\text{-}2$$

where Q_{ice} is the flux of R_{ice} flowing from cell to cell, k_{ice} is the ice conductivity, Δx is the cell size, and i is the local topographic slope. When R_{ice} reaches a cell not covered by glacier, it is treated as an input term in the soil balance of that cell.

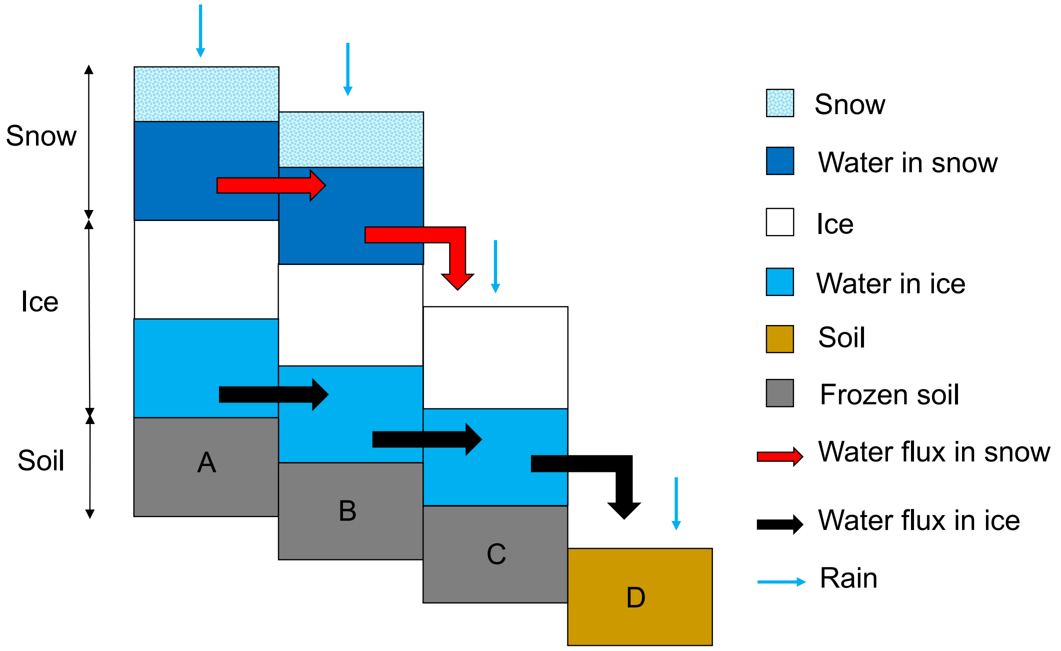

Figure 5.1 Vertical and lateral fluxes interconnection scheme on cells covered by snow and ice (A,B), only covered by ice (C), and free from snow and ice (D).

Box 5.A Glaciers initial conditions

Initial conditions require two information: the glaciers area and the ice (water equivalent) thickness in each cell.

For the first request, the *GLIMS* project (www.glims.org) allows to obtain the most recent mapping of glaciers around the world.

The best way to have information about glaciers thickness is to do direct measurements, as radio-echo soundings, but this kind of measures are very difficult and unusual over large areas. In literature several approaches to estimate glaciers thickness have been developed. One method use volume-area scale relations for glaciers (*Chen and Ohmura*, 1990), this allows to obtain the mean ice thickness over the entire glacier. Other methods involve principles of ice flow mechanics and require knowledge of surface velocity field, as the one developed by *Farinotti et al.*, 2009; despite the accuracy of this method, such a physical modelling approach requires an onerous input data set and can only be applied to well-monitored glacier system.

Another class of methods employs the perfect plasticity assumption coming from *Nye's* (1952) theory for the flow mechanics of an infinitely wide glacier (*Aleynikov et al.*, 2002; *Wallinga and van de Wal*, 1998; *Hoelzle et al.*, 2003; *Li et al.*, 2012). The Nye's theory revised by *Aleynikov et al.* (2002) is simple, it doesn't involve onerous calculation and data request, but allows to maintain the raster based approach, characterizing each iced cell with the correspondent ice thickness. The ice thickness is calculated with Equation (5-3), knowing the local slope α , the average density of ice, ρ (equal to 840 kg/m3), the gravity acceleration , g, and the maximum possible shear stress, τ_P (equal to 0.10 MPa).

$$h = \frac{\tau_P}{\rho\, g\, \sin\alpha} \tag{5-3}$$

However, this formulation is valid only for plane areas with $l > 5h$; for the remaining areas, where approximation of a glacier by a plane-parallel plate is inappropriate, the maximum thickness of the glacier would be higher in comparison with calculation made with Equation (5-3). The corrected thickness, h_c, is obtained by inserting a coefficient depending on the glacier width, b:

$$h_c = \frac{1+h}{b}\frac{\tau_P}{\rho\, g\, \sin\alpha} \tag{5-4}$$

where h represents the results of the calculation according to Equation (5-3).

CHAPTER 6

INFILTRATION AND RUNOFF

Infiltration is the process by which water on the ground surface enters the soil. It is commonly used in both hydrology and soil sciences (*Haghaibi et al.*, 2011).

Infiltration is caused by multiple factors including; gravity, capillary forces, adsorption, and osmosis. Many soil characteristics can also play a role in determining the rate at which infiltration occurs.

Infiltration takes place in the vadose zone, also termed the unsaturated zone. It is the part of Earth between the land surface and the top of the phreatic zone, the position at which the groundwater (the water in the soil's pores) is at atmospheric pressure ("vadose" is from the Latin word for "shallow"). Hence, the vadose zone extends from the top of the ground surface to the water table.

Water in the vadose zone has a pressure head less than atmospheric pressure and is retained by capillary action. If the vadose zone envelops soil, the water contained therein is termed soil moisture. In fine grained soils, capillary action can cause the pores of the soil to be fully saturated above the water table at a pressure less than atmospheric. The vadose zone does not include the area that is still saturated above the water table, often referred to as the capillary fringe.

The description of water flow in the vadose zone is quite complicated as compared to the saturated zone (*Merdun*, 2012). An accurate description of soil hydraulic properties is the main limitation for a good description of water processes under unsaturated flow conditions in particular when implemented for large study areas. This led many researchers to simplify the description of water movement as one dimensional vertical process though it is a three dimensional.

Several infiltration models exist in the literature that exhibit different levels of accuracy. These models are usually based on Richards equation (*Richards*, 1931; *Lassabatere et al.*, 2009). Richards equation provides an appropriate tool to describe the infiltration process with a detailed description of the flow and water distribution within the soil profile (*Tinet et al.*, 2015). Numerical solutions based on finite difference, finite element or boundary element techniqueshave been used to solve Richards equation (*Feddes et al.*, 1988). Due to the non-linearity of the described process as well as the high detail of soil hydraulic parameters requirements, the use of numerical solutions is considered as time consuming and facing some stability problems (*Tinet et al.*, 2015). Despite the progress made for developing efficient numerical schemes joined with faster computers, the use of such numerical methods is still time consuming when implemented for large study areas (*Ross*, 2003).

Several simplifications have been suggested to model the infiltration process. These models are commonly categorized into *empirical*, *semi-empirical* and *physically based* (*Mishra et al.*, 2003). Empirical models are formulated as simple equation, derived from actual field measured infiltration data through curve fitting *(Ravi and Williams*, 1998). Examples of these models are: SCS-CN (*SCS*, 1985), *Kostiatov* (1932), *Collis-George* (1977), *Huggins and Monke* (1966), etc. Many existing hydrological models in the literature are based on these empirical models, in particular the SCS-CN such as: *ANSWERS* (*Beasely and Huggins*, 1980), *EPIC* (*Sharplay and Williams*, 1990), *SWAT* (*Arnold et al.*, 2012), Etc. Many semi-empirical or approximations models exist for example: *Green and Ampt* (1911), *Philip* (1957), *Smith and Parlange* (1978), etc. These models allow a simplification of this process through some assumptions made either for soil hydraulic properties or for the boundary conditions (*Lassabatère et al.*, 2009).

Box 6.A The ponding time

According to *Brutsaert* (2005), *ponding time* is a term used in hydrology for a saturated soil surface (from rain) and occurs water puddle. When it rains, the water will be puddling if the intensity of the rain exceeds the value of the infiltration capacity of the soil that receives rain. Ponding time (t_p) is the time from the beginning of rainwater infiltration until surface runoff occurs, starting from the beginning of the rain occurs until the water begins to puddle on the soil surface. Time before ponding occurs ($t < t_p$), the intensity of rain is less than the potential rate of soil infiltration and the soil surface in unsaturated conditions. Ponding begins to occur when the intensity of rain exceeds the infiltration rate. At this time($t = t_p$), the soil surface begins to saturate with water. As the rain continues($t > t_p$), the soil saturated zone will deepen and the surface runoff begins to occur from the puddle.

Box 6.B The *Brooks and Corey* water retention curve

Water retention curve is the relationship between the water content, θ, and the soil water potential (suction), ψ. This curve is characteristic for different types of soil, and is also called the soil moisture characteristic. At potentials close to zero, a soil is close to saturation, and water is held in the soil primarily by capillary forces. As θ decreases, binding of the water becomes stronger, and at small potentials (more negative, approaching wilting point) water is strongly bound in the smallest of pores, at contact points between grains and as films bound by adsorptive forces around particles.

The shape of water retention curves can be characterized by several models, one of them known as the *Brooks and Corey* (1964):

$$\frac{\theta-\theta_r}{\theta_s-\theta_r} = \left(\frac{\psi}{\psi_a}\right)^B \qquad \text{6-1}$$

where θ_r and θ_s represent the residual and saturated soil moisture, respectively, (m^3/m^3), ψ represents the soil suction (m), ψ_a represents the air-entry pressure (m), and B is the pore size distribution index (-).

Equation for hydraulic conductivity of partially saturated soil, $K(\psi)$ (m/s), is:

$$K(\psi) = \begin{cases} K_s\left(\frac{\psi_a}{\psi}\right)^{2+3B} & \psi \le \psi_a \\ K_s & \psi > \psi_a \end{cases} \qquad \text{6-2}$$

where K_s (m/s) is hydraulic conductivity of saturated soil.

6.1 The SCS Curve Number

The SCS Curve Number (*SCS-CN*) (*SCS*, 1985) is one of widely implemented models for the calculation of surface runoff. According to this method, the infiltration is calculated as the difference between the precipitation and the runoff. *SCS-CN* method does not consider the rainfall intensity or duration; it only considers the total precipitation.

$$I = P_{tot} - R \qquad \text{6-3}$$

$$\mathrm{R} = \frac{(\mathrm{P}-\mathrm{I_a})^2}{\mathrm{P}-\mathrm{I_a}+\mathrm{S}} \qquad 6\text{-}4$$

with

$$I_a = 0.2\,S \qquad 6\text{-}5$$

where ***I*** is the total infiltration [L], P is the precipitation [L], R is the runoff [L], S is the maximum retention capacity [L], and I_a is the initial abstraction. S and CN are related.

$$S = S_0\left(\frac{100}{\mathrm{CN}} - 1\right) \qquad 6\text{-}6$$

with $S_0 = 254$ mm. The fraction of precipitation that is not converted to runoff is accounted for as infiltration.

The CN parameter values were derived from the curves of the plotted relationship between the rainfall and the runoff. The CN is mainly related to the land use. The CN value is adjusted according to the antecedent moisture conditions. CN_{II} stands for average soil moisture conditions (AMC II) of the previous 5 days, CN_I stands for dry soil moisture conditions AMC I and CN_{III} stands for wet soil moisture conditions AMC III. The *SCS-CN* approach has been subjected to several modifications in order to be adopted for various land uses and climatic conditions (*Soulis and Valiantzas*, 2012). Many researchers have proposed a modified version of the *SCS-CN* for continuous simulations (*Adornado and Yoshida*, 2010). The method proposed by *Ravazzani et al.* (2007) has been implemented within the *FeST* model. According to this method at each time step, S is calculated depending on the soil degree of saturation, ε_t

$$S = S_1 - \varepsilon(S_1 - S_3) \qquad 6\text{-}7$$

with

$$S_1 = S(CN_I) \qquad 6\text{-}8$$

$$\mathrm{S}_{\,3} = \mathrm{S}(CN_{III}) \qquad 6\text{-}9$$

$$CN_I = CN_{II} - \left(20\,\frac{100 - CN_{II}}{100 - CN_{II} + EXP\big(2.533 - 0.0636\,(100 - CN_{II})\big)}\right) \qquad 6\text{-}10$$

$$CN_{III} = CN_{II}\,EXP\,\big(0.00673\,(100 - CN_{II})\big) \qquad 6\text{-}11$$

$$\varepsilon_t = \frac{\theta_t - \theta_r}{\theta_s - \theta_r} \qquad 6\text{-}12$$

where θ_t is the actual water content at time t [L^3/L^3], θ_s is the saturated water content [L^3/L^3] and θ_r is the residual water content [L^3/L^3].

S in equation 6-7 is updated in each cell at the beginning of a storm event, ant it is kept constant till the end of the storm. The CN_{II} parameters values, function of CORINE land cover class (https://land.copernicus.eu/user-corner/technical-library/clc-product-user-manual), and hydrological class are reported in Table 6.1.

Table 6.1 The CN_{II} parameter values as a function of CORINE land cover class and hydrological class (A, B, C, and D)

CORINE code	***Description***	CN_{II}			
		A	B	C	D
111	Continuous urban fabric	77	85	90	92
112	Discontinuous urban fabric	57	72	81	86
121	Industrial or commercial units	89	90	94	94
122	Road and rail networks and associated land	98	98	98	98
123	Port areas	89	92	94	94
124	Airports	81	88	91	93
131	Mineral extraction sites	46	69	79	84
132	Dump sites	46	69	79	84
133	Construction sites	46	69	79	84
141	Green urban areas	39	61	74	80
142	Sport and leisure facilities	39	61	74	80
211	Non-irrigated arable land	70	80	86	90
212	Permanently irrigated land	85	90	92	94
213	Rice fields	100	100	100	100
221	Vineyards	45	66	77	83
222	Fruit trees and berry plantations	45	66	77	83
223	Olive groves	45	66	77	83
231	Pastures	30	58	71	78
241	Annual crops associated with permanent crops	58	73	82	87
242	Complex cultivation patterns	58	73	82	87
243	Land principally occupied by agriculture, with significant areas of natural vegetation	52	70	80	84
244	Agro-forestry areas	58	73	82	87
311	Broad-leaved forest	36	60	73	79
312	Coniferous forest	36	60	73	79
313	Mixed forest	36	60	73	79
321	Natural grassland	49	69	79	84
322	Moors and heathland	49	69	79	84
323	Sclerophyllous vegetation	49	69	79	84
324	Transitional woodland/shrub	36	60	73	79
331	Beaches, dunes, sands	76	85	89	91
332	Bare rock	77	86	91	94
333	Sparsely vegetated areas	49	69	79	84
334	Burnt areas	77	86	91	94

335	Glaciers and perpetual snow	100	100	100	100
411	Inland marshes	100	100	100	100
412	Peatbogs	100	100	100	100
421	Salt marshes	100	100	100	100
422	Salines	100	100	100	100
423	Intertidal flats	100	100	100	100
511	Water courses	100	100	100	100
512	Water bodies	100	100	100	100
521	Coastal lagoons	100	100	100	100
522	Estuaries	100	100	100	100
523	Sea and ocean	100	100	100	100

6.2 Philip

Philip proposed a semi analytical solution (*Philip*, 1957) to solve the non-linear partial differential Richards equation (*Richards*, 1931). The infiltration capacity, i^*, as expressed by Philip's equation is approximated by

$$i^*(t) = \frac{1}{2} S_i \cdot t^{-\frac{1}{2}} + C_{S,3} \cdot K_s \tag{6-13}$$

where S_i is a parameter called sorptivity (m/s^2), which is a function of the soil suction potential, t is the time from the beginning of infiltration process (s), K_s is the hydraulic conductivity (m/s), and $C_{S,3}$ is a constant. The sorptivity is considered as capacity of the soil to uptake or release water.

An analytic expression of S_i and $C_{S,3}$ is given by *Sivapalan et al.* (1987):

$$C_{S,3} = \frac{1}{2} \left(1 + \theta_{rs,i}^{\eta}\right) \tag{6-14}$$

where

$$\eta = \frac{2 + 3 \cdot B}{B} \tag{6-15}$$

$$\theta_{rs,i} = \frac{\theta_i - \theta_r}{\theta_s - \theta_r} \tag{6-16}$$

where B is the Brooks and Corey (1964) pore size distribution index, θ_i is the soil water content at the beginning of the infiltration, θ_s and θ_r are the water content at saturation and residual, respectively.

$$S_i = \left[\frac{2 \cdot K_S(\theta_s-\theta_i)^2\psi_c}{(\theta_s-\theta_r)}\left(\frac{1}{\eta+\frac{1}{2}B-1}+\frac{\theta_s-\theta_r}{\theta_s-\theta_i}\right)\right]^{\frac{1}{2}} \qquad 6\text{-}17$$

where ψ_c is the soil suction head (bubbling pressure) (m).

According to *Milly* (1986), under the assumption of time compression approximation, infiltration capacity can be expressed as a function of cumulative infiltration:

$$i^*(i_c) = C_{S,3} \cdot K_S\left(1+\left[\left(1+\frac{4 \cdot C_{S,3} \cdot K_S \cdot i_c}{S_i^2}\right)^{\frac{1}{2}}-1\right]^{-1}\right) \qquad 6\text{-}18$$

where i_c is the cumulative infiltration computed by integrating the infiltration amount from the beginning of the precipitation event.

The actual infiltration rate, i, is computed as the minimum between infiltration capacity and rainfall rate, $Rain$:

$$i = min[i^*(i_c), Rain] \qquad 6\text{-}19$$

When rain rate exceeds infiltration capacity, the rainfall excess is transformed to runoff.

Box 6.C The time compression approximation

Infiltration capacity is the maximum infiltration rate that results when rainfall intensity is so large that the surface is saturated (i.e., ponded) instantaneously. Actual infiltration rate is typically lower due to the limited water supply to the soil surface, especially during early times during typical rainfall events. Indeed, infiltration capacity starts out large during early times, and as more and more rainfall infiltrates, infiltration capacity decreases with time. The decreasing infiltration capacity eventually becomes equal to the rainfall intensity, and surface runoff (and ponding) is initiated. Ponding time is defined as the time after the beginning of rainfall at which ponding or surface runoff occurs (*Diskin and Nazimov*, 1996). From that time onward, with continued rainfall, the surface remains ponded, and so actual infiltration rate remains equal to infiltration capacity but continues to decrease with time until (in the long term) it reaches a constant rate asymptotically, provided the soil is sufficiently deep. The infiltration theory suggests the early-time infiltration behavior is governed by absorption (due to capillary action of soil), while late-time behavior is governed by gravitational action, and that the final constant infiltration rate after a long time is approximately equal to the saturated hydraulic conductivity of the soil (*Brutsaert*, 2005).

However, rainfall intensity is seldom larger than infiltration capacity at early times (*Assouline*, 2013), and therefore, initially, all rainfall infiltrates. To account for this discrepancy, the time compression approximation (*TCA*), also referred to as time condensation approximation, was introduced to estimate both ponding time and the postponding infiltration rate. The essential concept behind *TCA* is the assumption of a unique, invariant relationship between infiltration capacity and the cumulative infiltration volume, regardless of the rainfall (or infiltration) history. The infiltration rate and cumulative infiltration volume after ponding could be obtained by shifting the time of infiltration capacity and cumulative potential infiltration over a compression reference time, respectively (Brutsaert, 2005); this explains the name “time condensation approximation”.

6.3 Green and Ampt

Green and Ampt (1911) derived an approximate mechanistic model for infiltration under ponded condition into a deep homogeneous soil with uniform initial moisture content which assumes a piston-type water content profile with a well-defined wetting front. This model is based on the hypothesis that there is the existence of sharp wetting front having a constant matric potential and the wetting zone is uniformly wetted with a constant hydraulic conductivity (Figure 6.1). The model can be derived by combining the *Darcy*'s law with the continuity principle. The resulting *Green-Ampt* equations is given as

$$f(t) = K\,\left(1 + \frac{h_0 + h_s}{L}\right) \qquad \text{6-20}$$

$$F(t) \,-\, (h_0 - h_s)\,\Delta\theta\,\ln\left(1 + \frac{F(t)}{(h_0 - h_s)\,\Delta\theta}\right) = K\,t \qquad \text{6-21}$$

where $f(t) = dF(t)/dt$ is the infiltration rate; K is the effective hydraulic conductivity; h_0 is the depth of ponding water over the soil surface; h_s is the capillary suction head at the wetting front; L is the depth of wetting front below the bottom of pond; $F(t)$ is the cumulative infiltration depth; and $\Delta\theta = \phi_e - \theta_i$ is the soil moisture deficit; ϕ_e is the effective porosity; and θ_i is initial (antecedent) moisture content.

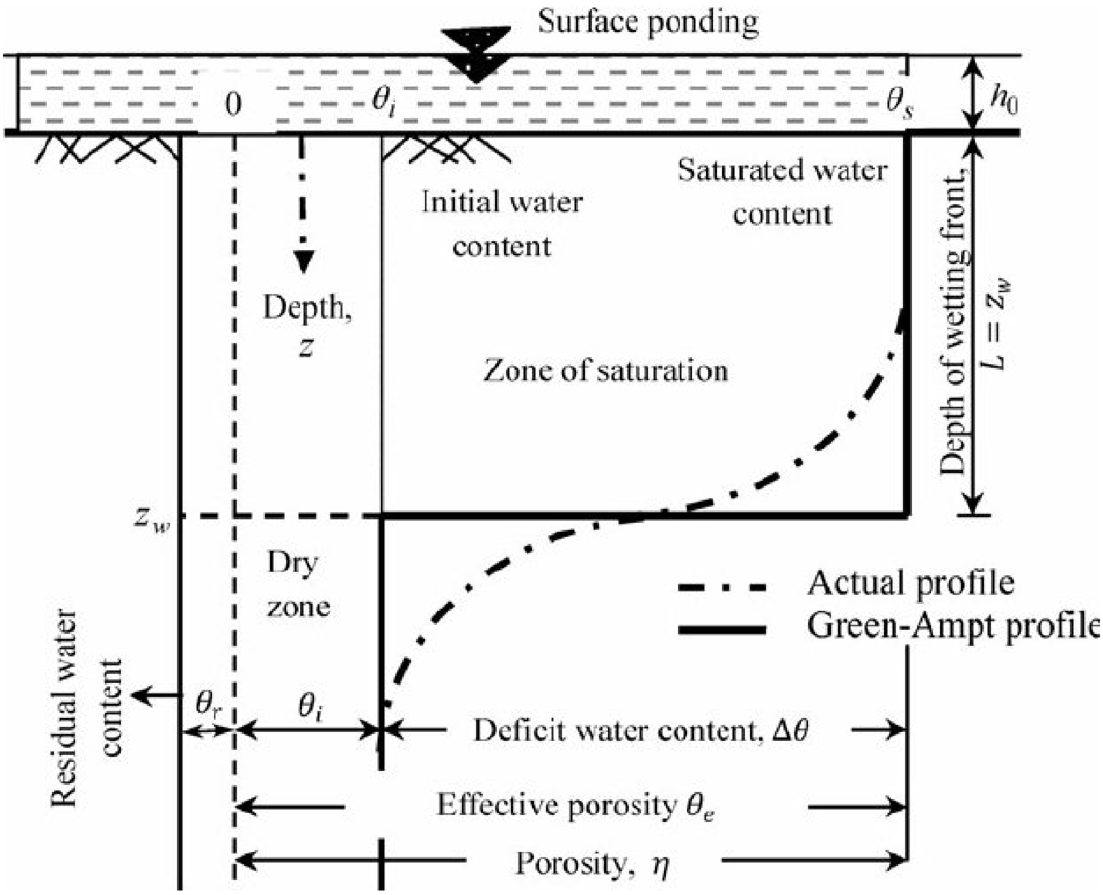
Surface ponding
0
θ_i
θ_s
h_0
Initial water content
Saturated water content
Depth, z
Zone of saturation
Depth of wetting front, $L = z_w$
z_w
Dry zone
Actual profile
Green-Ampt profile
Residual water content
θ_r
θ_i
Deficit water content, $\Delta\theta$
Effective porosity θ_e
Porosity, η

Figure 6.1 Infiltration profile for the Green-Ampt model. Adapted from *Kale and Sahoo*, 2011.

Equation 6-20 is applicable only when water starts ponding on the soil surface from the beginning of the rainfall event. Therefore, to use this equation considering the condition of ponding some time after the start of rainfall, *Mein and Larson* (1973) developed a two-stage model for infiltration (under a constant-intensity rainfall) into a homogeneous soil with uniform initial moisture content. The first stage predicted the volume of infiltration at the moment when surface ponding begins. The second stage, which is used for prediction of infiltration after the occurrence of the ponding, described the subsequent infiltration behavior, wherein they provided the equations for the calculation of ponding time and accumulated infiltration depth. This variant of the *Green-Ampt* model of *Mein and Larson* (1973) can also be found in the referred textbooks (*Chow et al.* 1988).

The basic principles of the method are: in the absence of ponding, cumulative infiltration is calculated from cumulative rainfall; the potential infiltration rate at a given time is calculated from the cumulative infiltration at that time; and ponding has occurred when the potential infiltration rate is less than or equal to the rainfall intensity.

Consider a time interval from t to Δt. The rainfall intensity during this interval is denoted i_t and is constant throughout the interval. The potential infiltration rate and cumulative infiltration at the beginning of the interval are $f(t)$ and $F(t)$, respectively, and the corresponding values at the end of the interval are $f(t+\ \Delta t)$, and $F(t+\ \Delta t)$. It is assumed that $f(t+\ \Delta t)$ is known from given initial conditions or previous computation.

A flow chart for determining ponding time is presented in Figure 6.2. There are three cases to be considered: (1) ponding occurs throughout the interval; (2) there is no ponding throughout the interval; and (3) ponding begins part-way through the interval. The infiltration rate is always either decreasing or constant with time, so once ponding is established under a given rainfall intensity, it will continue. Hence, ponding cannot cease in the middle of an interval, but only at its end point, when the value of the rainfall intensity changes.

The first step is to calculate the current potential infiltration rate $f(t)$, from the known value of cumulative infiltration $F(t)$:

$$f(t) = K\left(\frac{h_s\,\Delta\theta}{F(t)} + 1\right) \qquad 6\text{-}22$$

The result $f(t)$ is compared to the rainfall intensity i_t. If $f(t)$ is less than or equal to i_t, case (1) arises and there is ponding throughout the interval. In this case the cumulative infiltration at the end of the interval, $F(t+\ \Delta t)$ is calculated from

$$F(t+\ \Delta t)\ -\ F(t)-\ h_s\,\Delta\theta \ln\left(\frac{F(t+\Delta t)+\ h_s\,\Delta\theta}{F(t)+\ h_s\,\Delta\theta} + 1\right) = K\,\Delta t \qquad 6\text{-}23$$

Both cases (2) and (3) have $f(t)\ >\ i_t$ and no ponding at the beginning of the interval. Assume that this remains so throughout the interval; then, the infiltration rate is i_t and a tentative value for cumulative infiltration at the end of the time interval is

$$F'(t+\ \Delta t)\ =\ F(t) + i_t\ \Delta t \qquad 6\text{-}24$$

Next, a corresponding infiltration rate $f'(t+\ \Delta t)$ is calculated from $F'(t+\ \Delta t)$. If $f'(t+\ \Delta t)$ is greater than i_t , case (2) occurs and there is no ponding throughout the interval.

Thus $F(t+\ \Delta t)\ =\ F'(t+\ \Delta t)$ and the problem is solved for this interval.

If $f'(t + \Delta t)$ is is less than or equal to i_t, ponding occurs during the interval (case (3)). The cumulative infiltration $F(p)$ at ponding time is found by setting $f(t) = i_t$ and $F(t) = F(p)$ in (6-20) and solving for $F(p)$ to give

$$F(p) = \frac{K\, h_s\, \Delta\theta}{i_t - K} \tag{6-25}$$

The ponding time is then $t + \Delta t'$, where

$$\Delta t' = \frac{F(p) - (t)}{i_t} \tag{6-26}$$

and the cumulative infiltration $F(t + \Delta t)$ is found by substituting $F(t) = F(p)$ and $\Delta t = \Delta t - \Delta t'$ in (6-23). The excess rainfall values are calculated by subtracting cumulative infiltration from cumulative rainfall, then taking successive differences of the resulting values. When rain rate exceeds infiltration capacity, the rainfall excess is transformed to runoff.

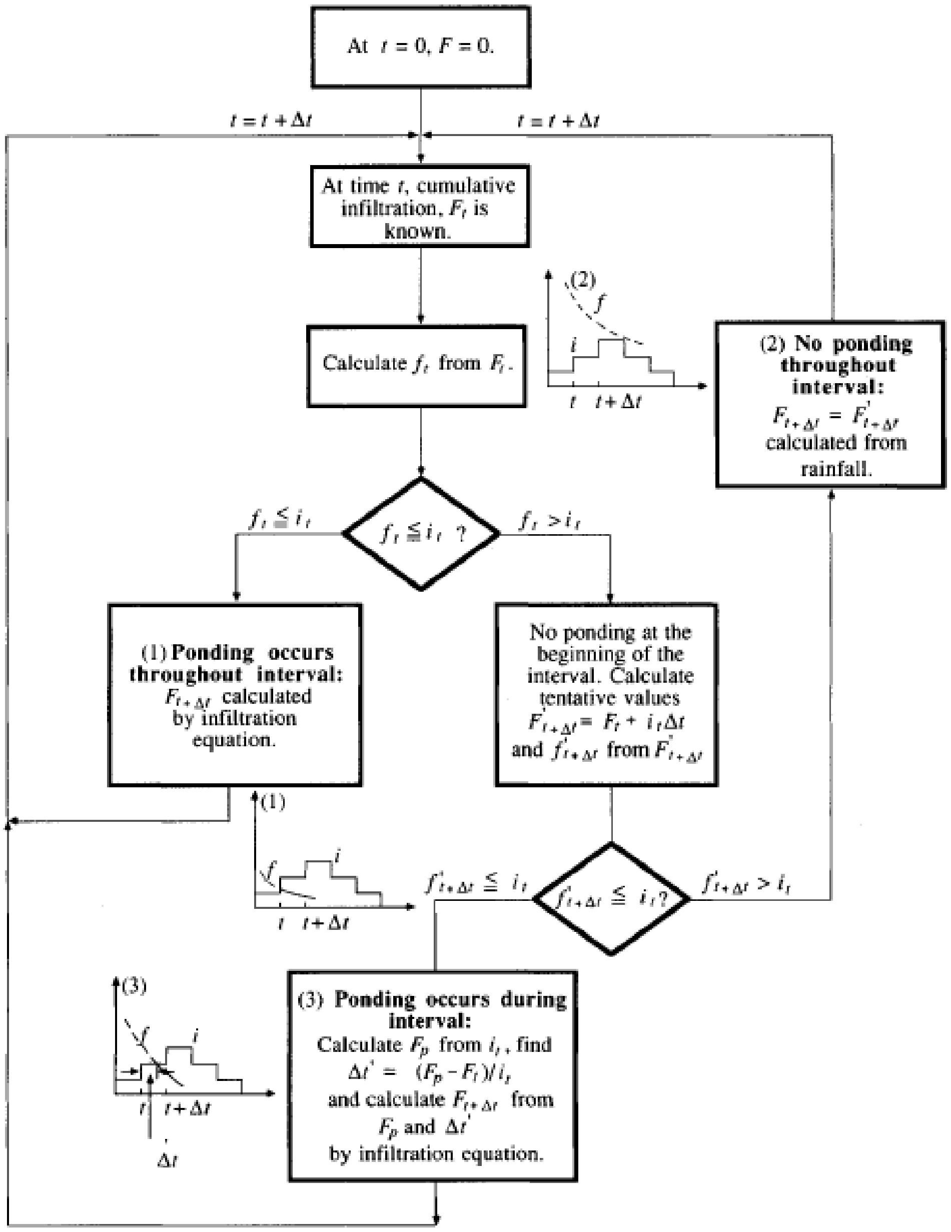
At $t = 0$, $F = 0$.
$t = t + \Delta t$
$t = t + \Delta t$
At time t, cumulative infiltration, F_t is known.
Calculate f_t from F_t.
(2)
f
i
t $t+\Delta t$
(2) No ponding throughout interval:
$F_{t+\Delta t} = F'_{t+\Delta t}$ calculated from rainfall.
$f_t \leqq i_t$
$f_t \leqq i_t$?
$f_t > i_t$
(1) Ponding occurs throughout interval:
$F_{t+\Delta t}$ calculated by infiltration equation.
No ponding at the beginning of the interval. Calculate tentative values $F'_{t+\Delta t} = F_t + i_t \Delta t$ and $f'_{t+\Delta t}$ from $F'_{t+\Delta t}$
(1)
f
i
t $t+\Delta t$
$f'_{t+\Delta t} \leqq i_t$
$f'_{t+\Delta t} \leqq i_t$?
$f'_{t+\Delta t} > i_t$
(3)
f
i
t $t+\Delta t$
$\Delta t'$
(3) Ponding occurs during interval:
Calculate F_p from i_t, find $\Delta t' = (F_p - F_t)/i_t$ and calculate $F_{t+\Delta t}$ from F_p and $\Delta t'$ by infiltration equation.

Figure 6.2 Flow chart for determining infiltration and ponding time under variable rainfall intensity. (*Chow et al.*, 1988)

Box 6.D Soil hydrological parameter estimates based on soil texture.

The following table reports soil hydrological parameter estimates (from *Gowdish and Muñoz-Carpena*, 2009; *Rawls and Brakensiek*, 1982, and *Rawls et al.*, 1982).

USDA texture	K_s	θ_s	θ_r	B	θ_{wp}	θ_{fc}	h_s	ψ_c
Clay	1.66E-07	0.475	0.090	0.165	0.272	0.296	0.623	0.373
Silty Clay	2.50E-07	0.479	0.056	0.150	0.250	0.317	0.578	0.342
Silty Clay-Loam	4.16E-07	0.432	0.040	0.177	0.208	0.300	0.538	0.326
Sandy Clay	3.33E-07	0.430	0.109	0.223	0.239	0.232	0.467	0.292
Sandy Clay-Loam	1.19E-06	0.330	0.068	0.177	0.148	0.187	0.424	0.281
Clay-Loam	6.38E-07	0.390	0.075	0.242	0.197	0.245	0.409	0.259
Silt	1.55E-06	0.450	0.020	0.200	0.140	0.240	0.350	0.210
Silt-Loam	1.88E-06	0.486	0.015	0.234	0.133	0.261	0.330	0.208
Loam	6.60E-07	0.434	0.027	0.252	0.117	0.200	0.175	0.112
Sand	5.83E-05	0.417	0.020	0.694	0.033	0.048	0.096	0.073
Loamy Sand	1.69E-05	0.401	0.035	0.553	0.055	0.084	0.120	0.087
Sandy Loam	7.19E-06	0.412	0.041	0.378	0.095	0.155	0.215	0.147

K_s hydraulic conductivity (m/s)
θ_s saturated volumetric water content (m^3/m^3)
θ_r residual volumetric water content (m^3/m^3)
B pore size distribution index
θ_{wp} volumetric water contenta at the wilting point (m^3/m^3)
θ_{wp} volumetric water contenta at the field capacity (m^3/m^3)
h_s suction at the wetting front (m)
ψ_c bubbling pressure (m)

CHAPTER 7
EVAPOTRANSPIRATION

Evapotranspiration is a key process of water balance and also an important element of energy balance (*Zhao et al.*, 2013). It covers both water evaporation (movement of water to the air directly from soil, canopies, and water bodies) and transpiration (movement of water from the soil, through roots and bodies of vegetation, on leaves and then into the air). Its precise estimation is not only of vital importance for the study of climate change and evaluation of water resources, but also has much application value in crop water requirement management, drought forecasting and monitoring, effective water resources development and utilization etc.

There are many methods to estimate evapotranspiration, from those taking into account evaporation from water surface to a variety of potential evapotranspiration and actual evapotranspiration estimations. In the *FeST* model two methods are implemented to compute actual evapotranspiration: one first estimates potential evapotranspiration (ET_p) and then converts it into actual evapotranspiration (ET_a) applying a *stress coefficient*; the other one computes directly ET_a by solving the system of mass and energy balance equations. Methods to estimate ET_p can be classified into one of the following four categories:

- temperature-based (e.g., *Hargreaves and Samani*, 1985);
- radiation based (e.g., *Makkink*, 1957);
- mass-based (e.g., *Mahring*, 1970);
- methods combining energy and mass balance (e.g., *Penman*, 1948).

Box 7.A Potential and actual evapotranspiration

The term potential evapotranspiration (ET_p), due to *Thornthwaite* (1948), stands for the maximum rate of water loss by evaporation from the land surface under given atmospheric conditions, given abundant supply of soil moisture, that means assuming no control on water supply. Actual evapotranspiration (ET_a) is the quantity of water that is actually removed from a surface due to the processes of evaporation and transpiration and is limited by the amount of water that is available.

7.1 Potential evapotranspiration

Five methods are implemented in the FeST model to estimate ET_p :

- *Hargreaves-Samani*
- *Hargreaves-Samani-Ravazzani*
- *Priestley-Taylor*
- *Penman-Monteith*
- *FAO Penman-Monteith*

Box 7.B Reference evapotranspiration and the crop coefficient

The term reference evapotranspiration, denoted as ET_0, stands for the evapotranspiration from the reference surface, the so-called reference crop evapotranspiration, as defined by the Food and Agriculture Organization of the United Nations (FAO). The reference surface is a hypothetical grass reference crop with an assumed crop height of 0.12 m, a fixed surface resistance of 70 s m^{-1} and an albedo of 0.23. The only factors affecting ET_0 are climatic parameters. Consequently, ET_0 is a climatic parameter and can be computed from weather data. ET_0 expresses the evaporating power of the atmosphere at a specific location and time of the year and does not consider the crop characteristics and soil factors. Typical ranges for ET_0 values for different agroclimatic regions are given in the following Table.

Average ET_0 for different agroclimatic regions in mm/day

	Cool ~10°C	Moderate 20°C	Warm > 30°C
Tropics and subtropics			
- humid and sub-humid	2 - 3	3 - 5	5 - 7
-arid and semi-arid	2 - 4	4 - 6	6 - 8
Temperate region			
- humid and sub-humid	1 - 2	2 - 4	4 - 7
-arid and semi-arid	1 - 3	4 - 7	6 - 9

Reference evapotranspiration intends to avoid ambiguities that existed in the definition of potential evapotranspiration. By adopting a reference crop (grass), consistent crop coefficient selection has become easier and more practical (*Djaman*, 2013). The introduction of the reference evapotranspiration concept also helped transfer crop coefficients from one location to another. Reference evapotranspiration allows more consistent crop coefficient selection and evapotranspiration equation calibration for a given local climate.

Historically, two main crops have been used as the reference crop, grass, and alfalfa. It is generally accepted that the grass reference crop is the type of grass with physiological and structural characteristics similar to perennial ryegrass (*Lolium perenne* L.) or alta fescue (*Festuca arundinacea Schreb*. Alta). Although alfalfa has the physical characteristics (leaf area index, roughness, etc.) closer to many agronomic crops than the grass, researchers generally agree that a clipped grass provides a better representation of reference evapotranspiration than does alfalfa. This is mainly because of the two reasons: (*FAO*, 1998) the characteristics of the grass are better known and defined, (*McMahon*, 2013) the grass crop has more planting areas than alfalfa throughout the world, and the measured evapotranspiration rates of the grass are more readily available and accessible as compared to the measured alfalfa evapotranspiration rates.

To compute the evapotranspiration of the specific crop, ET_C , a crop coefficient, K_c, is used.

$$ET_C = K_c \; ET_0 \tag{7-1}$$

Changes in vegetation and ground cover mean that the crop coefficient K_c varies during the growing period. The trends in K_c during the growing period are represented in the crop coefficient curve.

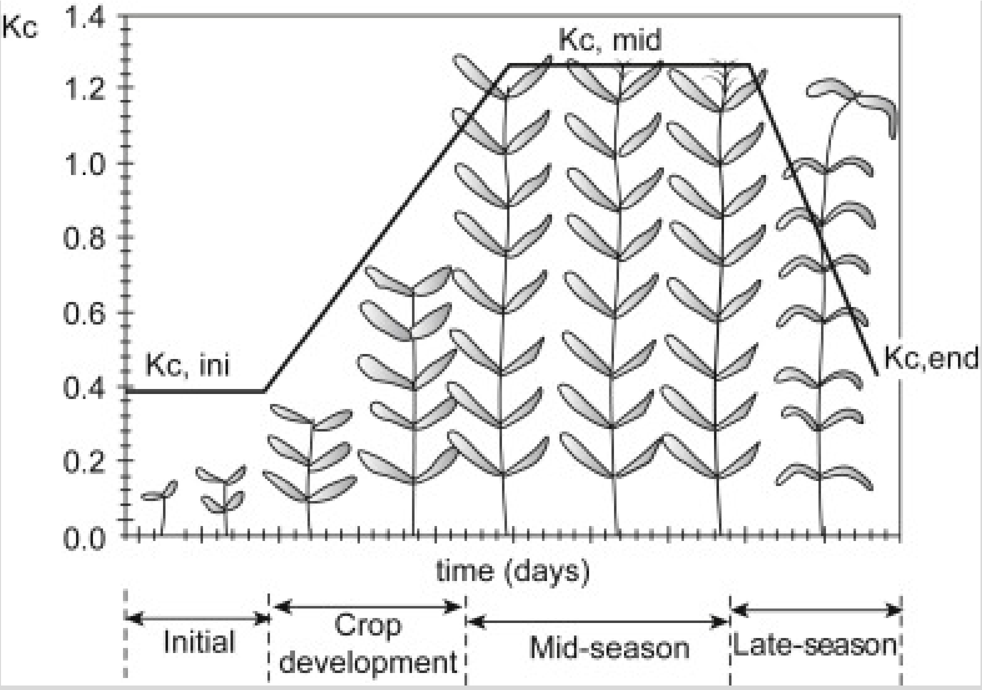

Generalized crop coefficient curves (*FAO*, 1998).

7.1.1 Hargreaves-Samani

The *Hargreaves and Samani* (1985) equation for calculating daily potential evapotranspiration is:

$$ET_{P-HS} = HC\ R_a\ (T_{max} - T_{min}\ )^{HE}\ \left(\frac{T_{max}+T_{min}}{2} + HT\right) \tag{7-2}$$

where ET_{P-HS} is the potential evapotranspiration estimated by the *Hargreaves-Samani* equation (mm day^{-1}), R_a extraterrestrial radiation (mm day^{-1}), T_{max} daily maximum air temperature (°C), T_{min} daily minimum air temperature (°C), HC empirial coefficient ($HC =$ 0.0023), HE empirical exponent ($HE = 0.5$), and HT is needed to convert units of Fahrenheit to Celsius ($HT = 32/1.8 = 17.8$) (*Hargreaves*, 1994). Equation 7-2 uses the average daily air temperature in combination with extraterrestrial radiation as an indicator of the incoming global radiation. Moreover, the daily temperature range is related to relative humidity and cloudiness (*Hargreaves and Samani,* 1982; *Samani and Pessarakli*, 1986; *Shuttleworth*, 1993; *Di Stefano and Ferro*, 1997).

7.1.2 Hargreaves-Samani-Ravazzani

Ravazzani et al. (2012) introduced a correction factor based on two calibrating coefficients, c_0 and c_1, to fix the general tendency of *Hargreaves-Samani* to overestimate evapotranspiration at low elevation and underestimate it at higher elevations in the italian Alps:

$$ET_{P-HSR} = (c_0 + c_1 z)ET_{HS} \qquad 7\text{-}3$$

where ET_{P-HSR} is the reference evapotranspiration computed with the modified equation and z is station elevation (m a.s.l.). Coefficients in equation 7-3 were determined by choosing c_0 and c_1 to minimize the mean bias error on stations belonging to upper Po river basin, Italy. The algorithm adopted for optimization was the generalized reduced gradient, a nonlinear extension of the simplex method for linear programming (*Lasdon et al.*, 1978). The values of the best fit calibrating parameters are 0.817 for c_0 and 0.00022 for c_1. The final modified equation to compute potential evapotranspiration can then be rewritten:

$$ET_{P-HSR} = (0.817 + 0.00022\, z) \cdot HC \cdot R_a \cdot (T_{max} - T_{min})^{HE} \cdot \left(\frac{T_{max}+T_{min}}{2} + HT\right) \qquad 7\text{-}4$$

7.1.3 Penman and Penman-Monteith

The *Penman* equation describes potential evaporation from an open water surface, and was developed by *Howard Penman* in 1948. Penman's equation requires air temperature, wind speed, air relative humidity, and solar radiation to predict potential evaporation.

$$E_{P-P} = \frac{\Delta(R_n - G) + \frac{\rho_a c_p (e^* - e_a)}{r_a}}{\lambda(\Delta + \gamma)} \qquad 7\text{-}5$$

where

E_{P-P} potential evapotranspiration estimated by the *Penman* equation (mm s^{-1})

Δ slope of the relationship between saturation vapour pressure and temperature (kPa°C^{-1}) computed as:

$$\Delta = \frac{4098\left[0.6108\, exp\left(\frac{17.27\, T}{T+237.3}\right)\right]}{(T+237.3)^2} \qquad \text{7-6}$$

T air temperature (°C)
R_n net radiation (MJ m^{-2} s^{-1})
G ground heat flux (MJ m^{-2} s^{-1}) computed as

$$G = 0.1\, R_n \qquad \text{7-7}$$

ρ_a air density (kg m^{-3}) computed as

$$\rho_a = \frac{P}{T_{kv}\, R} \qquad \text{7-8}$$

R specific gas constant = 0.287 (kJ kg^{-1} K^{-1})
T_{kv} virtual air temperature (K) computed as

$$T_{kv} = 1.01\,(T + 273) \qquad \text{7-9}$$

P air pressure (kPa) computed as

$$P = 101.3\,\left(\frac{293-0.0065\, z}{293}\right)^{5.26} \qquad \text{7-10}$$

z ground elevation (m asl)
c_p humid air specific heat (MJ kg^{-1} °C^{-1}) computed as

$$c_p = \frac{\gamma\, \varepsilon\, \lambda}{P} \qquad \text{7-11}$$

γ psychrometric constant (kPa °C^{-1}) computed as

$$\gamma = 0.665 \cdot 0.001 \cdot P \qquad 7\text{-}12$$

$\varepsilon = 0.622$ ratio molecular weight of water vapour/dry air

$\lambda = 2.453$ latent heat of vaporization (MJ / kg)
e^* saturation vapor pressure (Pa) computed as

$$e^* = 0.6108\, exp\left(\frac{17.27\, T}{T+237.3}\right) \qquad 7\text{-}13$$

e_a actual vapor pressure (Pa) computed as

$$e_a = e^* \left(\frac{RH}{100}\right) \qquad 7\text{-}14$$

RH air relative humidity (0-100).
r_a aerodynamic resistance of bare soil (s m^{-1}) computed as

$$r_a = \frac{ln\left(\frac{z_m+h-d}{z_{om}}\right) ln\left(\frac{z_h+h-d}{z_{oh}}\right)}{k^2\, u_z} \qquad 7\text{-}15$$

z_m wind speed measurement heigth (m)
$h = 0.1$ bare soil heigth (m)
$d = 2/3\ h$ bare soil zero plane displacement height (m)
z_{om} $0.123\ h$ roughness length governing momentum transfer (m)
z_h relative humidity measurement height (m)
$z_{oh} = 0.1\ z_{om}$ roughness length governing transfer of heat and vapor (m)
$k = 0.41$ von Karman’s constant
u_z wind speed (m/s)

When vegetation is present, plant transpiration that is the vaporization of liquid water and subsequent loss of water as vapor through leaf stomata, must be included as a component of the evapotranspiration. For this purpose, the *Penman* equation was further developed by *Monteith* (1965) and extended to cropped surfaces by introducing resistance factors, giving origin to the *Penman-Monteith* equation.

$$T_{P-PM} = \frac{\Delta\, R_n + \frac{\rho_a c_p (e^* - e_a)}{r_a}}{\lambda\left[\Delta + \gamma\left(1 + \frac{r_c}{r_a}\right)\right]} \qquad 7\text{-}16$$

where

T_{P-PM} potential transpiration estimated by the *Penman-Monteith* equation (mm s-1)

r_c canopy resistance (s m-1) conputed as

$$r_c = \frac{r_{s\,min}}{LAI} \qquad 7\text{-}17$$

$r_{s\,min}$ minimum stomatal resistance (s m-1)

LAI leaf area index (m^2/m^2)

Aerodynamic resistance of vegetated soil in *Penman-Monteith* equation is computed considering the crop height.

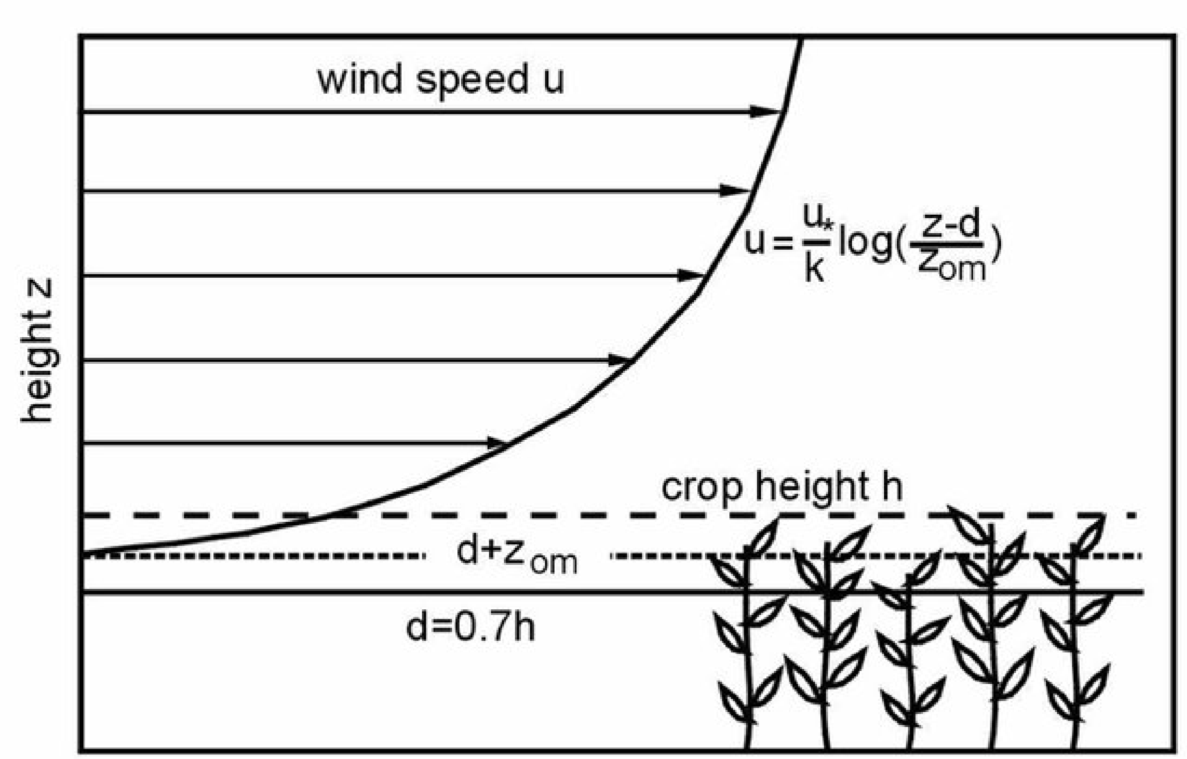

Figure 7.1 Vertical distribution of wind speed over a vegetated surface of height h. The profile follows the logarithmic distribution. The zero plane displacement d is about 0.7 h. The wind speed becomes zero at $d + z_{om}$ (*Immerzeel et al.*, 2006)

7.1.4 FAO Penman-Monteith

The *FAO-56 Penman-Monteith* equation for calculating reference evapotranspiration (*Allen et al.*, 1998) is:

$$ET_{0-PM} = \frac{0.408\mathit{\Delta}(R_n - G) + \gamma\frac{900}{T+273}U_2(e_s - e_a)}{\mathit{\Delta} + \gamma(1 + 0.34U_2)} \tag{7-18}$$

where: ET_{0-PM} is the reference evapotranspiration estimated by the *FAO-56 Penman-Monteith* equation (mm day^{-1}), R_n net radiation (MJ m^{-2} day^{-1}), G soil heat flux (MJ m^{-2} day^{-1}), T average daily air temperature at 2 m height (°C), U_2 wind speed at 2 m height (m s^{-1}), e_s saturation vapour pressure (kPa), e_a actual vapour pressure (kPa), $\mathit{\Delta}$ slope of the saturated water-vapor-pressure curve (kPa °C^{-1}), γ the psychrometric constant (kPa °C^{-1}). The computation of all data required for the calculation of the reference evapotranspiration followed the method given in Chapter 3 of the FAO paper 56 (*Allen et al.*, 1998).

7.1.5 Priestley-Taylor

The *Priestley-Taylor* equation (*Priestley and Taylor*, 1972) is similar to the *Penman-Monteith* method, but simplified. That is, vapor deficit and convection terms are reduced to a single empirical constant, α. The *Priestley-Taylor* model can be represented as follows:

$$E_{P-PT} = \alpha \cdot \frac{\Delta \cdot (R_n - G)}{\lambda \cdot (\Delta + \gamma)} \tag{7-19}$$

where

E_{P-PT} potential evaporation estimated by the *Priestley-Taylor* equation (mm s^{-1}).

α 0 1.26 an empirical constant accounting for the vapor pressure deficit and resistance values (-).

Transpiration from vegetated surface has the same expression but the soil heat flux is negligible:

$$T_{P-PT} = \alpha \cdot \frac{\Delta \cdot R_n}{\lambda \cdot (\Delta + \gamma)} \tag{7-20}$$

where

T_{P-PT} potential transpiration estimated by the *Priestley-Taylor* equation (mm s^{-1}).

The terms in Equations 7-19 and 7-20 are computed in the same way explained for *Penman-Monteith* equation.

Priestley-Taylor equation requires air temperature, air relative humidity, and solar radiation to predict potential evapotranspiration.

7.2 Actual evapotranspiration from potential one

The actual evapotranspiration, ET_a, is computed as a fraction of the potential rate tuned by a function that, in turn, depends on soil moisture content, and weighted according to the vegetation fraction coverage.

The global actual evapotranspiration rate is given by:

$$ET_a = (1 - f_v) \cdot E_a + f_v \cdot T_a \tag{7-21}$$

where E_a is the actual rate of bare soil evaporation, T_a is the actual rate of transpiration, and f_v is the fraction of vegetation area. The actual rates of the bare soil evaporation and transpiration are computed as a fraction of the potential evaporation, E_P, and potential transpiration, T_P (*Parlange et al.*, 1999):

$$E_a = \alpha(\theta) \cdot E_P \tag{7-22}$$

$$T_a = \beta(\theta) \cdot T_P \tag{7-23}$$

Where $\alpha(\theta)$ and $\beta(\theta)$ are *stress coefficient* computed as:

$$\alpha(\theta) = 0.082\theta + 9.173\theta^2 - 9.815\theta^3 \tag{7-24}$$

$$\beta(\theta) = \begin{cases} 0 & if \quad \theta \le \theta_{wp} \\ 1 & if \quad \theta \ge \theta_{fc} \\ \frac{\theta - \theta_{wp}}{\theta_{fc} - \theta_{wp}} & if \quad \theta_{wp} < \theta < \theta_{fc} \end{cases} \tag{7-25}$$

and where θ (-), θ_{fc} (-), and θ_{wp} (-) are current water content, field capacity, and wilting point, respectively.

7.3 Actual evapotranspiration from the energy balance

CHAPTER 8
SOIL WATER BALANCE

The soil water balance solution is the core of the *FeST* model, and hydrological modelling as a rule. The goal of the water balance is to update the water content of the unsaturated surficial layer of soil starting from initial or previous conditions, and taking into account the input and output water fluxes, by solving the continuity equation (Figure 8.1).

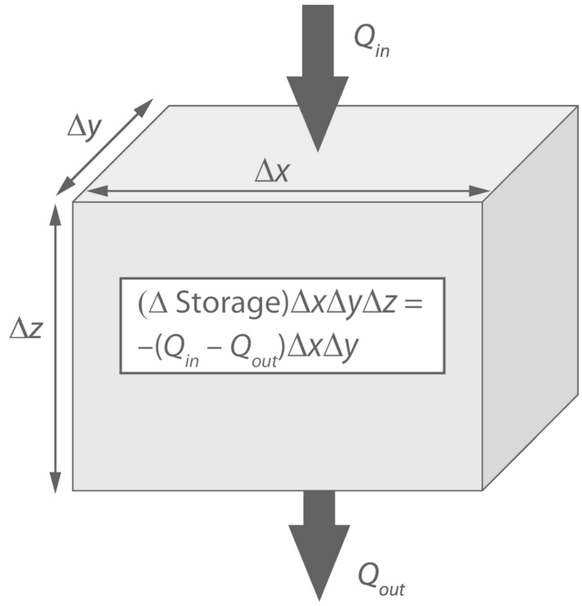
Q_{in}
Δy
Δx
Δz
$(\Delta \text{ Storage})\Delta x\Delta y\Delta z =$
$-(Q_{in} - Q_{out})\Delta x\Delta y$
Q_{out}

Figure 8.1 Water balance for a soil volume with the fluxes Q_{in} entering the volume and Q_{out} exiting the volume. (*https://www.cambridge.org/core/books/climate-change-and-terrestrial-ecosystem-modeling/soil-moisture/94367F1E2A95F1B991C333BB0637409C*)

The water content of unsaturated soil surface layer (also termed vadose zone, see Chapter 6) is a particularly important determinant of land–atmosphere coupling. A dry surface layer develops in the absence of rainfall, and this dry layer impedes soil evaporation. Conversely, plant roots can extend deep in the soil to sustain transpiration during dry periods. Below the vadose zone lies saturated groundwater, and soil moisture also controls the fluxes of water between the vadose zone and groundwater (Figure 8.2).

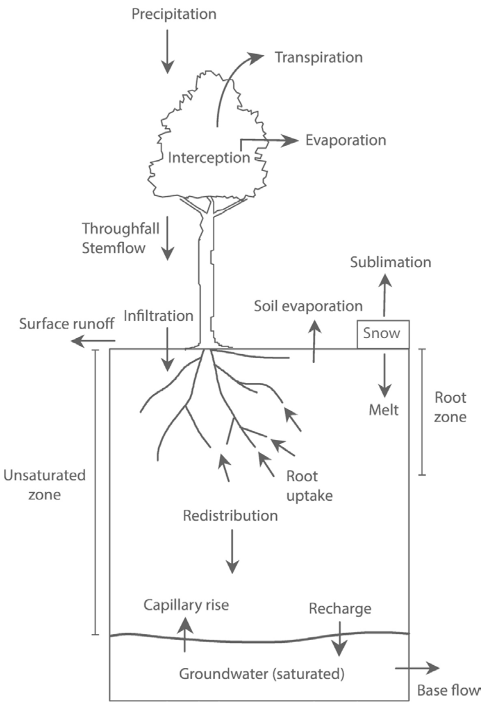
Precipitation
Transpiration
Evaporation
Interception
Throughfall
Stemflow
Sublimation
Surface runoff
Infiltration
Soil evaporation
Snow
Melt
Root zone
Unsaturated zone
Root uptake
Redistribution
Capillary rise
Recharge
Groundwater (saturated)
Base flow

Figure 8.2 Water flows in a soil column extending from the ground surface to the water table. (*https://www.cambridge.org/core/books/climate-change-and-terrestrial-ecosystem-modeling/soil-moisture/94367F1E2A95F1B991C333BB0637409C*)

The scheme of water balance implemented in the *FeST* model is articulated in three cases, according to whether the cell is located on hillslope, on a land plain where aquifer takes place, or in a lake.

8.1 Cell on hillslope

Cell on hillslope is supposed to be divided in two layers: the root zone where vegetation roots develop and water can be exchanged with atmosphere, the transmission zone where water can be stored as perched water table and migrate downward (Figure 8.3).
Water balance for root zone and transmission zone, for unit area, is computed as:

$$\vartheta_{t+1}^{rz} = \vartheta_t^{rz} + \frac{I-ET-P+TSE-RSE}{RZD}\,\Delta t \tag{8-1}$$

$$\vartheta_{t+1}^{tz} = \vartheta_t^{tz} + \frac{P-TSE-DP+LF_{in}-LF_{out}}{TZD}\,\Delta t \tag{8-2}$$

where ϑ_{t+1}^{rz}, ϑ_{t+1}^{tz}, ϑ_t^{rz}, and ϑ_t^{tz} are root and transmission zone soil moisture at time $t+1$, and t, respectively; I infiltration (m/s) (see Chapter 6); ET actual evapotranspiration (m/s) (see

Chapter 7); P is the percolation from root zone computed as actual hydraulic conductivity (Equation 6-2); DP is the percolation out of transmission zone, computed as hydraulic conductivity at saturation, multiplied by a coefficient that accounts for the degree of bedrock fracturation (0 for impermeable bedrock, 1 for fully permeable bedrock); TSE and RSE are saturation excess from transmission and root zone, respectively; RZD and TZD are root and transmission zone depth (m), respectively; Δt is time step duration from t to $t+1$. RSE is summed to runoff to account for the saturation excess runoff formation mechanism. LF_{out} is the lateral subsurface intercell flux. It is assumed that saturated subsurface flow in soils along the hillslope profile is described by Darcy's law (Swenson et al., 2019). Volumetric discharge in m3/s is computed as:

$$LF_{out} = w\,D_s\,\overline{K_{sub}}\,i \qquad 8\text{-}3$$

where w is the cell width (m), D_s is the thickness of the saturated zone (m), i is the topographic gradient (m/m) assuming a kinematic wave approximation. $\overline{K_{sub}}$ is the subsurface soil hydraulic conductivity at saturation computed as the harmonic mean between the values of the current, K_{sub} , and downstream cell, $K_{sub,d}$:

$$\overline{K_{sub}} = \frac{K_{sub} \cdot K_{sub,d}}{K_{sub} + K_{sub,d}} \qquad 8\text{-}4$$

LF_{out} becomes LF_{in} for the downstream cell following the topological cell interconnections defined for surface routing.

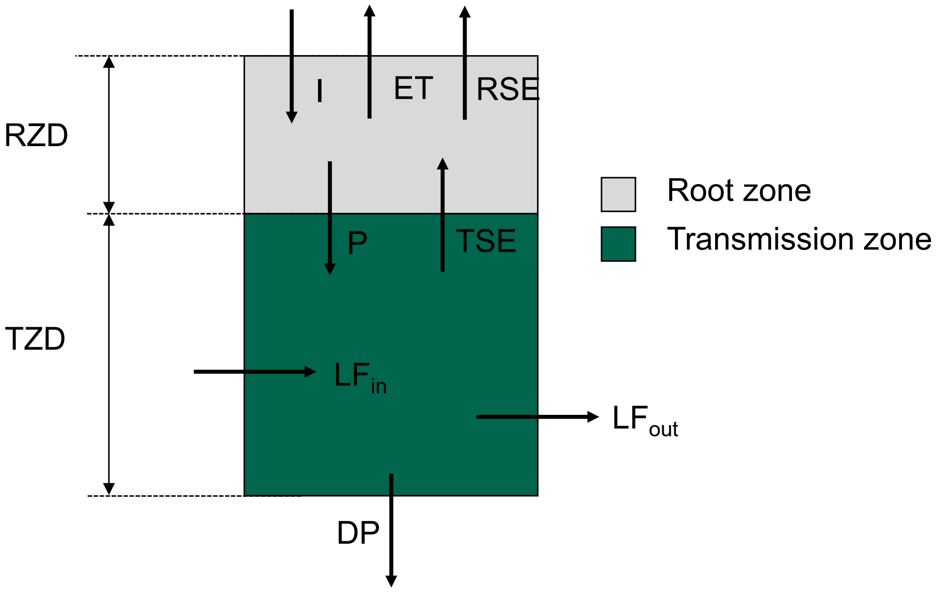

Figure 8.3 Soil balance scheme of cell on hillslope. RZD = root zone depth, TZD = transmission zone depth, I = infiltration, ET = evapotranspiration, RSE = saturation excess from root zone, P = percolation, TSE = saturation excess from transmission zone, LF$_{in}$ = input lateral flux, LF$_{out}$ = output lateral flux, DP = deep percolation.

8.2 Cell in land plain

This cell type characterizes the land plain area where vertical fluxes are dominant respect to lateral ones due to the mild or absent topographic slope. When land plain cell lays on top of aquifer, the deep percolation contributes to groundwater recharge. A vertical flux from the bottom is assumed in the opposite direction due to capillary rise from saturated soil. Capillary flux reduces groundwater recharge and is included as inlet to root zone balance. (Figure 8.4).

Water balance for root zone and transmission zone, for unit area, is computed as:

$$\vartheta_{t+1}^{rz} = \vartheta_t^{rz} + \frac{I-ET-P+CR+TSE-RSE}{RZD}\,\Delta t \qquad 8\text{-}5$$

$$\vartheta_{t+1}^{tz} = \vartheta_t^{tz} + \frac{P-TSE-DP}{TZD}\,\Delta t \qquad 8\text{-}6$$

where ϑ_{t+1}^{rz}, ϑ_{t+1}^{tz}, ϑ_{t}^{rz}, and ϑ_{t}^{tz} are root and transmission zone soil moisture at time $t+1$, and t, respectively; I infiltration (m/s) (see Chapter 6); ET actual evapotranspiration (m/s) (see Chapter 7); P is the percolation from root zone computed as actual hydraulic conductivity (Equation 6-2); DP is the percolation out of transmission zone, computed as hydraulic conductivity at saturation, multiplied by a coefficient that accounts for the degree of bedrock fracturation (0 for impermeable bedrock, 1 for fully permeable bedrock); CR is capillary rise flux; TSE and RSE are saturation excess from transmission and root zone, respectively; RZD and TZD are root and transmission zone depth (m), respectively; Δt is time step duration from t to $t+1$. RSE is summed to runoff to account for the saturation excess runoff formation mechanism.

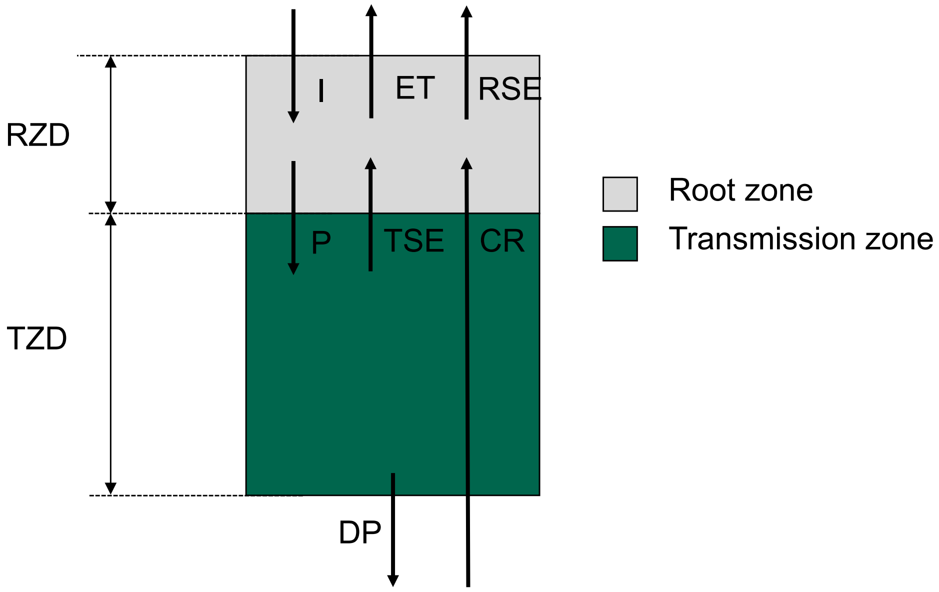

Figure 8.4 Soil balance scheme of cell in land plain. RZD = root zone depth, TZD = transmission zone depth, I = infiltration, ET = evapotranspiration, RSE = saturation excess from root zone, P = percolation, TSE = saturation excess from transmission zone, CR = capillary rise flux, DP = deep percolation

Capillary rise flux is assumed to come from the saturated soil of the underlying groundwater and reaching the root zone. It is computed with Darcy law according to the following equation:

$$CR = \frac{\bar{K}\ \psi_{rz}}{d} \tag{8-7}$$

where $\bar{K}$ is the hydraulic conductivity (m/s) at the interface with groundwater table computed as the harmonic mean between the saturated conductivity, K_s, and the unsaturated conductivity of root zone, K_{rz}:

$$\bar{K} = \frac{2\ K_s\ K_{rz}}{K_s + K_{rz}} \tag{8-8}$$

ψ_{rz} is root zone soil suction (m) computed from Equation 6-1 according to the root zone actual soil water content; d is the water table depth (m). When water table depth lies within the root zone or it is above ground elevation, root zone and transmission zone are assumed to reach soil saturation, vertical fluxes are set to zero except capillary rise that is set equal to potential evapotranspiration rate (this becomes a negative source term for groundwater head update), and runoff that is set equal to rainfall rate.

8.3 Cell in a lake

Cell in a lake is subjected to a simplified balance: soil water content is set to saturation, evapotranspiration is set to potential value, runoff is computed as precipitation less evapotranspiration rates.

CHAPTER 9
DISCHARGE ROUTING

9.1 Channel routing

Discharge routing is computed according to the variable parameter Muskingum-Cunge-Todini method (MCT; *Todini*, 2007), applied to every cell of the computation domain with length Δx.
The outflow $O_{t+\Delta t}$ from a reach segment of length Δx is given by a linear combination of variable coefficients and the inflow, I, and outflow at time t and $t+\Delta t$.

$$O_{t+\Delta t} = C_1\, I_{t+\Delta t} + C_2\, I_t + C_3\, O_t + C_4\, Q_l \qquad 9\text{-}1$$

where Q_l is lateral inflow. The coefficients expressed in terms of corrected Courant C^* and Reynolds D^* numbers are given by the following expressions:

$$C_1 = \frac{-1 + C^*_{t+\Delta t} + D^*_{t+\Delta t}}{1 + C^*_{t+\Delta t} + D^*_{t+\Delta t}} \qquad 9\text{-}2$$

$$C_2 = \frac{1 + C^*_t - D^*_t}{1 + C^*_{t+\Delta t} + D^*_{t+\Delta t}} \cdot \frac{C^*_{t+\Delta t}}{C^*_t} \qquad 9\text{-}3$$

$$C_3 = \frac{1 - C^*_t + D^*_t}{1 + C^*_{t+\Delta t} + D^*_{t+\Delta t}} \cdot \frac{C^*_{t+\Delta t}}{C^*_t} \qquad 9\text{-}4$$

$$C_4 = \frac{2\, C^*_{t+\Delta t}}{1 + C^*_{t+\Delta t} + D^*_{t+\Delta t}} \qquad 9\text{-}5$$

with

$$C^*_t = \frac{c_t}{\beta_t} \cdot \frac{\Delta t}{\Delta x} \qquad 9\text{-}6$$

$$C^*_{t+\Delta t} = \frac{c_{t+\Delta t}}{\beta_{t+\Delta t}} \cdot \frac{\Delta t}{\Delta x} \tag{9-7}$$

$$D^*_t = \frac{Q_t}{\beta_t \, B \, S_0 \, c_t \, \Delta x} \tag{9-8}$$

$$D^*_{t+\Delta t} = \frac{Q_{t+\Delta t}}{\beta_{t+\Delta t} \, B \, S_0 \, c_{t+\Delta t} \, \Delta x} \tag{9-9}$$

where c is the wave celerity, B is channel topwidth, S_0 is reach bed slope, and $\beta = \frac{c\,A}{Q}$ a dimensionless correcting factor.

A first guess estimate $\hat{O}_{t+\Delta t}$ for the outflow $O_{t+\Delta t}$ at time $t + \Delta t$ is initially computed as:

$$\hat{O}_{t+\Delta t} = O_t + (I_{t+\Delta t} - I_t) \tag{9-10}$$

where O_t is outflow a time t, $I_{t+\Delta t}$ and I_t are inflow at time $t + \Delta t$, and t, respectively.

Then the reference discharge is computed at time t, and $t + \Delta t$ as:

$$Q_t = \frac{I_t + O_t}{2} \tag{9-11}$$

$$Q_{t+\Delta t} = \frac{I_{t+\Delta t} + \hat{O}_{t+\Delta t}}{2} \tag{9-12}$$

and the reference water levels, y (normal depth), can be derived by means of a Newton-Raphson approach from the following implicit equations:

$$y_t = y\{Q_t, n, S_0\} \tag{9-13}$$

$$y_{t+\Delta t} = y\{Q_{t+\Delta t}, n, S_0\} \tag{9-14}$$

where n is Manning roughness coefficient, and S_0 is bed slope. Details of the Newton-Raphson procedure can be found in Box 9.A.

Box 9.A The Newton-Raphson algorithm to derive the normal depth

When the stage y is to be derived from a known discharge value Q^* in a channel, a non-linear implicit problem must be solved, except in the case of a very wide rectangular section for which the solution becomes trivial. Since a direct closed solution is not generally available, several numerical approaches to find the zeroes of a non-linear function can be used, such as the bisection or the Newton-Raphson methods. In this case, given that the involved functions are continuous and differentiable (triangular, rectangular and trapezoidal cross sections), a simple Newton-Raphson algorithm can be used. The problem reduces to finding the zeroes of the following function of y :

$$f(y) = Q(y) - Q^* = 0 \qquad 9\text{-}15$$

where $Q(y)$ ($L^3 T^{-1}$) is defined as:

$$Q(y) = \frac{\sqrt{S_0}}{n} \frac{A(y)^{5/3}}{P(y)^{2/3}} \qquad 9\text{-}16$$

with S_0 (dimensionless) the bottom slope, n the Manning friction coefficient ($L^{1/3} T^{-1}$), $A(y)$ (L^2) the wetted area, and $P(y)$ (L) the wetted perimeter.
The Newton-Raphson algorithm, namely:

$$y_{i+1} = y_i - f(y_i)/f'(y_i) \qquad 9\text{-}17$$

allows one to find the solution to the problem with a limited number of iterations starting from an initial guess y_0 and can be implemented in this case by defining:

$$f(y_i) = Q(y_i) - Q^* = \frac{\sqrt{S_0}}{n} \frac{A(y_i)^{5/3}}{P(y_i)^{2/3}} - Q^* \qquad 9\text{-}18$$

And taking the first derivative

$$f'(y) = \frac{d[Q(y) - Q^*]}{dy}\Big|_{y=y_i} = \frac{dQ(y)}{dy}\Big|_{y=y_i} = \frac{5}{3} \frac{\sqrt{S_0}}{n} \left[\frac{A(y)}{P(y)}\right]^{2/3} \left[B(y) - \frac{4}{5} \frac{A(y)}{P(y)\sin\alpha}\right] = B(y)\, c(y) \qquad 9\text{-}19$$

All quantities appearing in Equation 9-19 are provided in analytical form for geometric sections in Box 9.B.

Using the reference discharge and water level it is then possible to estimate all the other quantities at times t and $t + \Delta t$.
The celerity:

$$c_t = c\,\{Q_t, y_t, n, S_0\} \qquad 9\text{-}20$$

$$c_{t+\Delta t} = c\,\{Q_{t+\Delta t}, y_{t+\Delta t}, n, S_0\} \qquad 9\text{-}21$$

the actual expressions for the celerity valid for triangular, rectangular and trapezoidal cross sections, are given in Box 9.B.

The correcting factor, β:

$$\beta_t = \frac{c_t\, A_t}{Q_t} \qquad 9\text{-}22$$

$$\beta_{t+\Delta t} = \frac{c_{t+\Delta t}\, A_{t+\Delta t}}{Q_{t+\Delta t}} \qquad 9\text{-}23$$

The corrected Courant numbers, and cell Reynolds numbers, from Equations 9-6 ÷ 9-9, and the weight coefficients, $C_1 \div C_4$, from Equations 9-2 ÷ 9-5. The outflow is finally computed with Equation 9-1.

It is advisable to repeat twice the computation of outflow starting from Equation 9-11, in order to eliminate the influence of the first guess $\hat{O}_{t+\Delta t}$ given by Equation 9-10.

Storage, S, at time $t + \Delta t$ can be estimated as:

$$S_{t+\Delta t} = \frac{(1-D^*_{t+\Delta t})\,\Delta t}{2\; C^*_{t+\Delta t}}\, I_{t+\Delta t} + \frac{(1+D^*_{t+\Delta t})\,\Delta t}{2\; C^*_{t+\Delta t}}\, O_{t+\Delta t} \qquad 9\text{-}24$$

Eventually, the water stage can be estimated, by taking into account that the Muskingum model is a lumped model in space, which means that the water level will represent the “average” water level in the reach.

Firstly the average wetted area in the river reach is estimated as:

$$\bar{A}_{t+\Delta t} = \frac{S_{t+\Delta t}}{\Delta x} \qquad 9\text{-}25$$

from which, knowing the shape of the cross section, the water stage can be evaluated:

$$y_{t+\Delta t} = y\,\{\bar{A}_{t+\Delta t}\} \qquad 9\text{-}26$$

Equation 9-26 represents the average water stage in the reach and, on the basis of the Muskingum wedge assumption can be interpreted as the water stage more or less in the centre of the reach.

Box 9.B Hydraulic properties for triangular, rectangular and trapezoidal cross sections

Given the cross-sections in the Figure below, the following equations can be used to represent a generic triangular, rectangular or trapezoidal cross section.

$$A(y) = (B_0 + y\ \cot\alpha)\ y \tag{9-27}$$

the wetted area (L^2)

$$B(y) = B_0 + 2\,y\ \cot\alpha \tag{9-28}$$

the surface width (L)

$$P(y) = B_0 + 2\,y/\sin\alpha \tag{9-29}$$

the wetted perimeter (L) with B_0 the bottom width (L) ($B_0 = 0$ for the triangular cross section) and y the water stage (L).

The velocity ($L\,T^{-1}$) is computed as:

$$v(y) = \frac{Q(y)}{A(y)} = \frac{\sqrt{S_0}}{n}\,\frac{A\,(y)^{2/3}}{P\,(y)^{2/3}} \tag{9-30}$$

celerity ($L\,T^{-1}$) is calculated as:

$$c(y) = \frac{dQ(y)}{dA(y)} = \frac{1}{B(y)}\,\frac{dQ(y)}{dy} = \frac{5}{3}\frac{\sqrt{S_0}}{n}\,\frac{A\,(y)^{2/3}}{P\,(y)^{2/3}}\left(1 - \frac{4}{5}\,\frac{A(y)}{B(y)\,P(y)\ \sin\alpha}\right) \tag{9-31}$$

The correction factor is calculated as:

$$\beta(y) = \frac{c(y)}{v(y)} = \frac{5}{3}\left(1 - \frac{4}{5}\,\frac{A(y)}{B(y)\,P(y)\ \sin\alpha}\right) \tag{9-32}$$

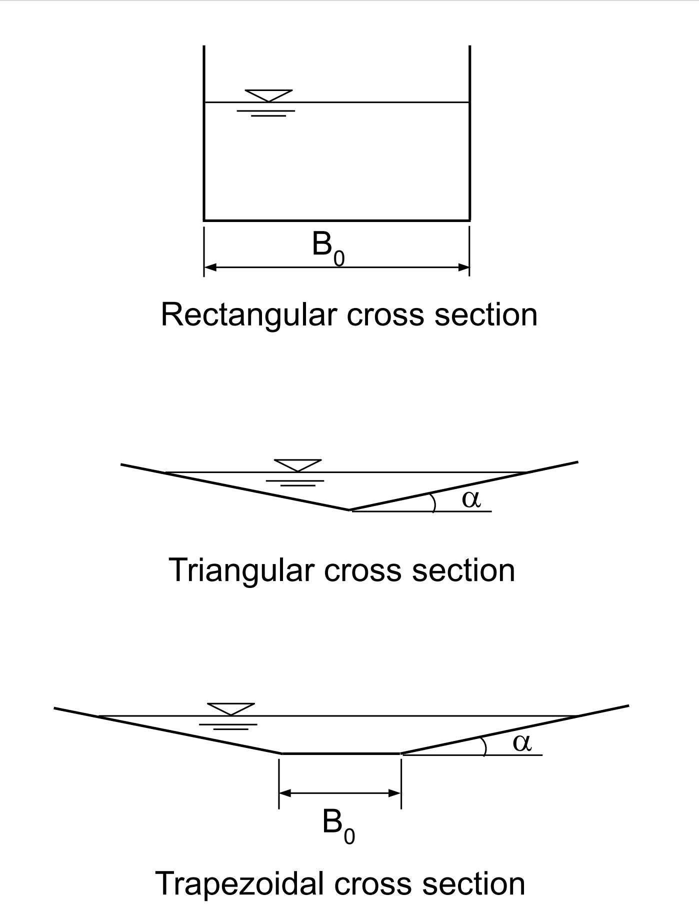
B0
Rectangular cross section
α
Triangular cross section
α
B0
Trapezoidal cross section

The three cross sections shapes (rectangular, triangular andtrapezoidal).

9.2 Level pool routing

Reservoirs and lakes can be modeled as a pool. Level pool routing is a procedure for calculating the outflow hydrograph from a reservoir with a horizontal water surface, given its inflow hydrograph and storage-outflow characteristics (*Fiorentini and Orlandini*, 2013).
The equations governing reservoir dynamics can be combined to yield the nonlinear first-order ordinary differential equation

$$\frac{dS}{dt} = I(t) - Q(t,S) \qquad 9\text{-}33$$

where S is the volume of water stored in the reservoir, t is the time, I is the inflow discharge, and Q is the outflow discharge, or the equivalent differential equation

$$\frac{dH}{dt} = \frac{I(t) - Q(t,H)}{A(H)} \qquad 9\text{-}34$$

where H is the water surface level and $A = dS/dh$ is the water surface area at elevation H.

The storage function $S = S(h)$ relating water surface level H and reservoir storage S can be determined by using topographic maps or by processing digital elevation models. The outflow function $Q = Q(t, H)$ can be derived from hydraulic equations relating the head H to the outflow discharge Q. Physical modeling may be necessary in all those cases in which the (gated) bottom outlets (sluice gates) and/or spillways involved cannot be (entirely) characterized in a conceptual manner.

Equation 9-33 can be solved analytically under the assumptions that the storage-outflow discharge relationship can be expressed in the form of a power function and input discharge is represented by simple functions. In most of the cases of practical relevance, however, Equation 9-33 and Equation 9-34 need to be solved numerically. Runge-Kutta method is numerical method often employed for this purpose (*Carnahan et al.*, 1969; *Chow et al.*, 1988).

Box 9.C Idro lake simulation

Lake Idro, or Eridio, is a lake of glacial origin located in the province of Brescia on the border with Trentino, in Northern Italy. Situated at 368 meter above sea level, it is formed by the waters of the Chiese river which is also its outlet. Its surface is 10.9 km² and reaches a maximum depth of 122 meter.

Lake Idro is the first natural Italian lake, to have been subjected to artificial regulation. The original idea of constructing a dam dates back to 1855, but the concession was given jointly to Società Elettrica Bresciana (SEB) and the University of Naviglio Grande Bresciano in 1917 to reduce Lake Idro to a regulated reservoir, in order to produce electricity and have greater volumes of water for the summer irrigation of the Brescia and Mantua areas. The regulation work was built in the 1920s and came into operation in 1933.

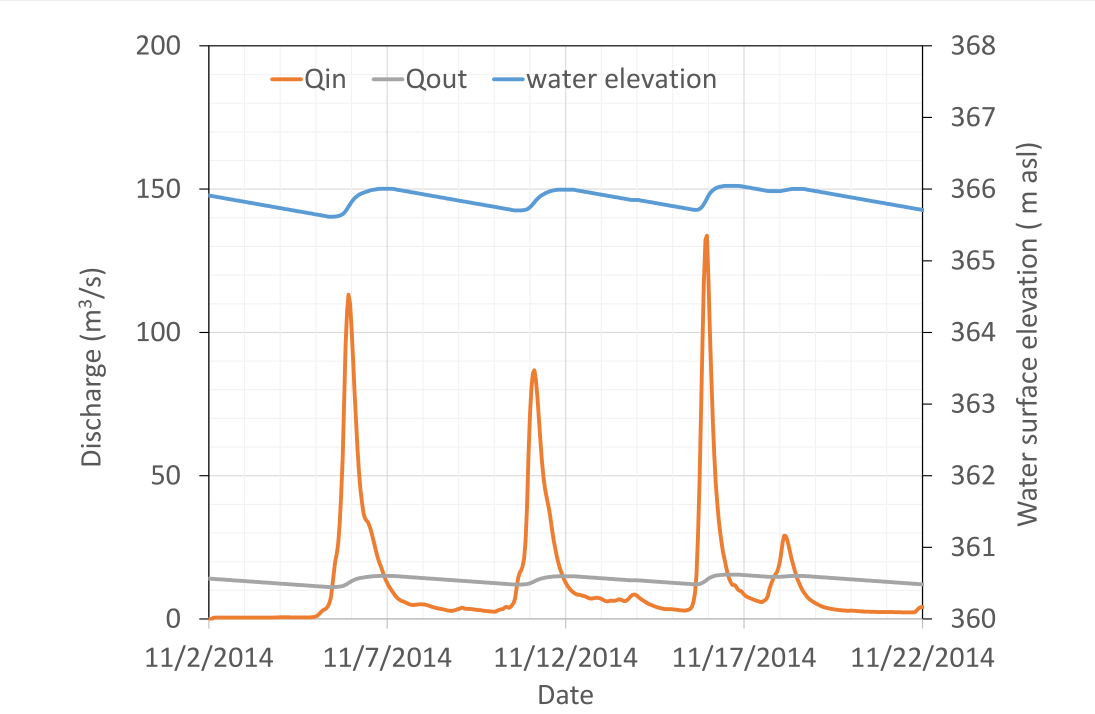

Input and output discharge and water elevation of the Idro lake simulated by the *FeST* model.

9.2.1 Third order Runge-Kutta method

To solve Equation 9-34 using a third-order integration scheme, three small increments of the independent variable, time, using known values of the dependent variable H are made. The water elevation H at the (j + 1)th time step is expressed as

$$H_{j+1} = H_j + \frac{1}{4}(\Delta H_1 + 3\Delta H_3) \quad 9\text{-}35$$

where the three successive approximations are estimated as

$$\Delta H_1 = \frac{I(t_j) - Q(H_j)}{A_r(H_j)} \Delta t \quad 9\text{-}36$$

$$\Delta H_2 = \frac{I\left(t_j + \frac{\Delta t}{3}\right) - Q\left(H_j + \frac{\Delta H}{3}\right)}{A_r\left(H_j + \frac{\Delta H}{3}\right)} \Delta t \quad 9\text{-}37$$

$$\Delta H_3 = \frac{I\left(t_j+2\frac{\Delta t}{3}\right)-Q\left(H_j+2\frac{\Delta H}{3}\right)}{A_r\left(H_j+2\frac{\Delta H}{3}\right)}\Delta t \qquad \text{9-38}$$

9.2.2 Fourth order Runge-Kutta method

To solve Equation 9-34 using a fourth-order integration scheme, four small increments of the independent variable, time, using known values of the dependent variable H are made. The water elevation H at the (j + 1)th time step is expressed as

$$H_{j+1} = H_j + \frac{1}{6}\left(\Delta H_1 + 2\cdot\Delta H_2 + 2\cdot\Delta H_3 + \Delta H_4\right) \qquad \text{9-39}$$

where the four successive approximations are estimated as

$$\Delta H_1 = \frac{I(t_j)-Q(H_j)}{A_r(H_j)}\cdot\Delta t \qquad \text{9-40}$$

$$\Delta H_2 = \frac{I\left(t_j+\frac{1}{2}\Delta t\right)-Q\left(H_j+\frac{1}{2}\Delta H_1\right)}{A_r\left(H_j+\frac{1}{2}\Delta H_1\right)}\cdot\Delta t \qquad \text{9-41}$$

$$\Delta H_3 = \frac{I\left(t_j+\frac{1}{2}\Delta t\right)-Q\left(H_j+\frac{1}{2}\Delta H_2\right)}{A_r\left(H_j+\frac{1}{2}\Delta H_2\right)}\cdot\Delta t \qquad \text{9-42}$$

$$\Delta H_4 = \frac{I(t_j+\Delta t)-Q(H_j+\Delta H_3)}{A_r(H_j+\Delta H_3)}\cdot\Delta t \qquad \text{9-43}$$

CHAPTER 10
HYDRAULIC STRUCTURES

10.1 Dams and reservoirs

Sustainable management of a river as a resource requires that water is delivered at the time of need for human use and that the supply is reliable. At the same time, water should be available for the survival of the riverine ecosystems. Dams are constructed across valleys or rivers to store, regulate and divert water for various purposes such as agricultural production, hydropower generation, human and industrial use and flood peak attenuation. Most dams serve multiple purposes.

10.2 On-stream flood detention basin

A detention basin is an excavated area to protect against flooding by storing water for a limited period of time. These basins are also called dry ponds, holding ponds or dry detention basins if no permanent pool of water exists. An on-stream detention basin acts as a constriction in a stream, only allowing a certain amount of water through at a time. When the capacity of the outlet structure is exceeded, a portion of the stream's flow is temporarily stored. The stored water is released over an extended period of time, thus preventing flooding downstream by delaying discharge of runoff.

Simulation of on-stream flood detention basin in *FeST* model is performed by solving the level pool routing equation (Section 9.2)

Box 10.A The Gurone detention basin on the Olona river

The Gurone reservoir is an example of on stream detention basin that was put into operation in 2010 to mitigate flood risk on the Olona river, in northern Italy. The basin stores a total volume of 1.79 Mm^3. Two gates regulate the basin outflow to keep the maximum discharge below 36 m^3/s. When the water elevation inside the basin exceeds 289.3 m asl, water is evacuated from a 114 m length spillway with a maximum capacity of 175 m^3/s at the maximum water elevation of 290.57 m asl. The minimum water level in the basin is 278.9 m asl.

The Gurone on-stream flood detention basin on the Olona river. (image credit: PIANO EMERGENZA DIGA – PED DIGA DI OLONA (VA)..

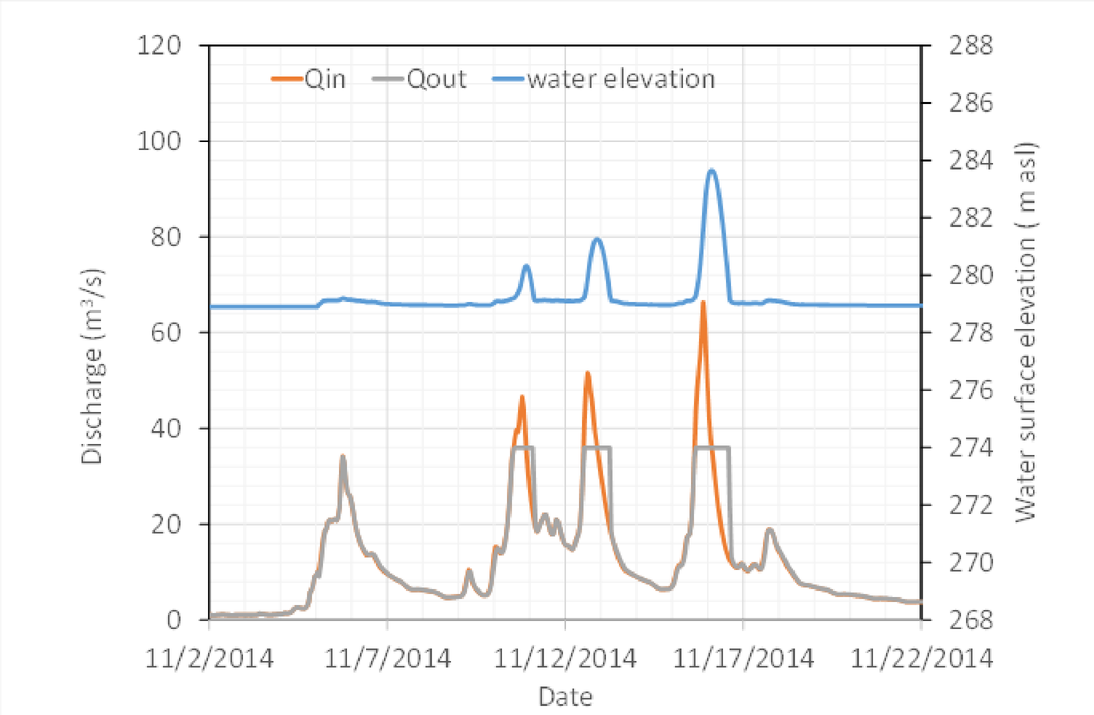

Input and output discharge and water elevation inside the Gurone on-stream detention basin simulated by the *FeST* model.

10.3 Off-stream flood detention basin

10.4 Bypass and diversion channels

Bypass channels divert river flows from a point upstream of an area requiring protection. These diverted flows can be discharged back to the same river, herein referred to as a bypass channel or into another natural drainage system nearby, herein referred to as a diversion channel (Figure 10.1). Functioning of a bypass channel depends mainly on its location, length, carrying capacity and inlet characteristics. While a bypass channel reduces flood magnitude in the bypassed area, it may increase flooding farther downstream, as floodwaters are rushed through the bypass channel. A diversion channel can increase the possibility of flooding in the receiving drainage system downstream if the diverted flows are larger than its carrying capacity.

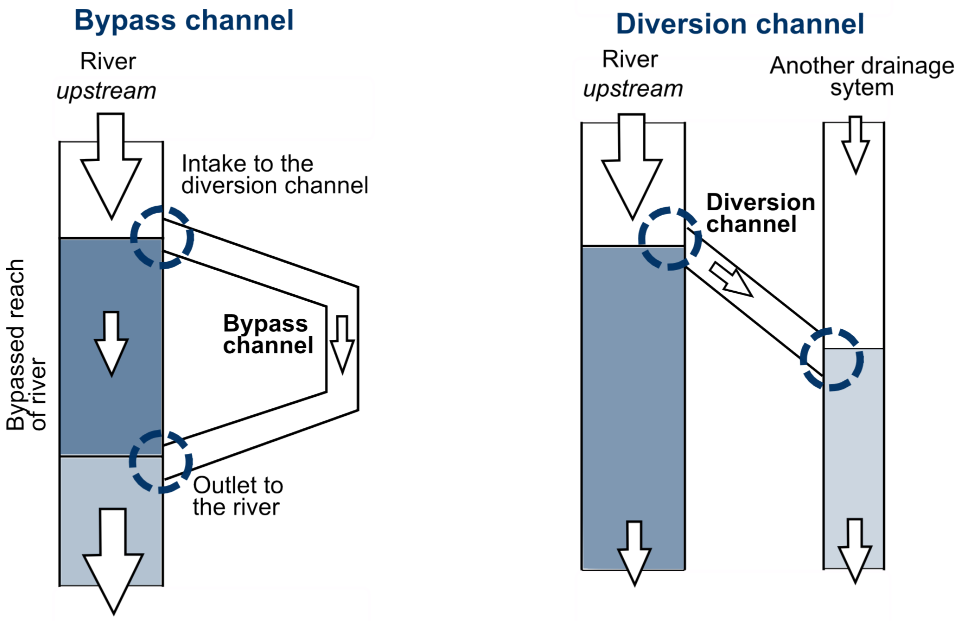
Bypass channel
River
upstream
Intake to the
diversion channel
Bypassed reach
of river
Bypass
channel
Outlet to
the river
Diversion channel
River
upstream
Another drainage
sytem
Diversion
channel

Figure 10.1 Bypass and diversion channel. Image Credit: *Schulte et al.*, 2018.

Diversions and by-pass channels are simulated by the *FeST* model by defining a look-up table with the diverted discharge respect to the river discharge and a cell where the discharge is subtracted from the river. Diverted water is discharged back to a given cell, belonging to the same river or to another drainage system, by routing the discharge with the Muskingum-Cunge-Todini approach (Section 9.1).

Box 10.B The diversion channel on the Seveso river

The Seveso river, in Northern Italy, is a small river that flows into Milan. This area is frequently hit by high rainfall intensity events that cause severe floods. The urban development after the second World War, has reduced the river basin soil infiltration capacity and exacerbated the flood occurrences. In 1980 the *canale scolmatore di nord ovest* (CSNO) diversion channel was put into operation to mitigate the flood risk in Milan. It is a 34 km length channel that deviates a maximum discharge of 30 m^3/s from the Seveso river to convey it into the Ticino river.

The *CSNO* diversion channel on the Seveso river. Image credit: Stefano Stabile, CC BY-SA 3.0, via Wikimedia Commons.

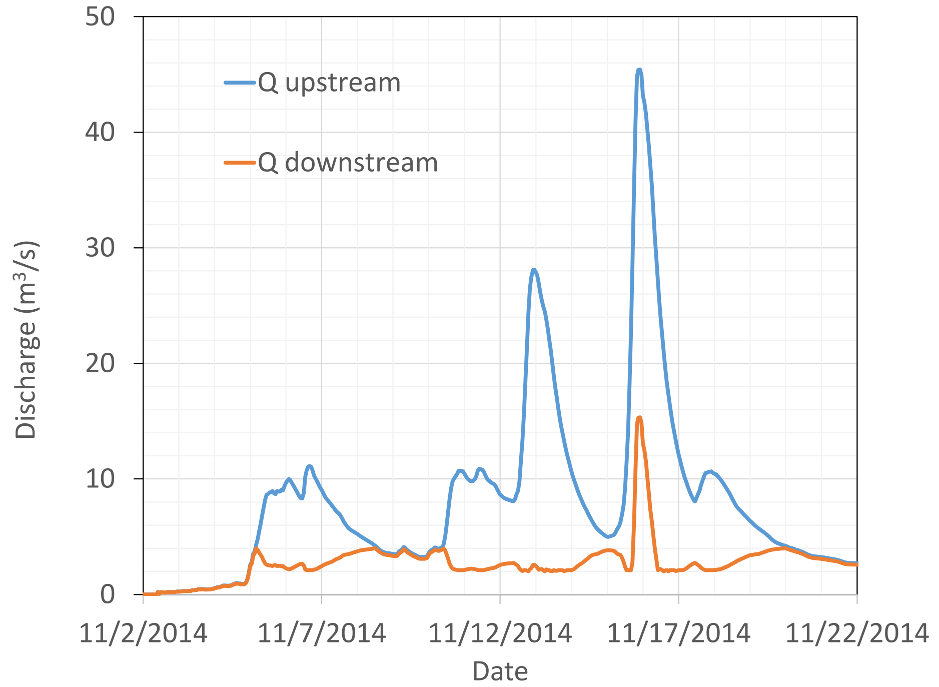

Discharge in the Seveso river upstream and downstream the *CSNO* intake section.

CHAPTER 11
GROUNDWATER

The *FeST* model can simulate groundwater flow with a quasi 3D scheme based on macroscopic Cellular Automata (CA) (*Ravazzani et al.*, 2011). CA represents a simple, attractive and alternative modelling technique respect to traditional numerical models that solve differential equations to describe complex phenomena (*Toffoli*, 1984). Cellular Automata are dynamical systems which are discrete in space and time, operate on a uniform, regular lattice and are characterised by local interactions. They were introduced by *von Neumann* (1966) to study self-reproducing systems and have been later used for modelling disparate complex physical phenomena (*Di Gregorio, et al.*, 1999; *Jimenez-Hornero et al.*, 2003; *Parsons and Fonstad*, 2007; *Marshall and Randhir*, 2008).

Many complex macroscopic fluid dynamical phenomena seem difficult to be modelled in these CA frames, because they take place on a large space scale and require a macroscopic level of description. Empirical CA methods were developed on the macroscopic scale in order to overcome this problem, dealing directly with the macroscopic variables (*Di Gregorio and Serra*, 1999; *D'Ambrosio et al.*, 2001). These CA make use of local laws that are ruled by empirical parameters. As these latter can have no direct link with classical physical parameters, an accurate calibration phase is generally required (*Iovine et al.*, 2005). At the contrary, physically based Macroscopic Cellular Automata (MCA), in which local rules derive directly by physical laws and depend on physical parameters, do not require a similar calibration (*Bates and De Roo*, 2000; *Horritt and Bates*, 2001; *Mendicino et al.*, 2006).

11.1 Groundwater flow

Models based on CA paradigm consist of four primary components: a lattice of cells, the definition of a local neighbourhood area, transition rules determining the changes in cell properties, and boundary conditions (*Parsons and Fonstad*, 2007). To simulate water flux in unconfined aquifer, a two-dimensional lattice of cells is created. A value of saturated hydraulic conductivity, K_s [L T^{-1}], a value of specific yield, S_y [-], elevation of the bottom of the aquifer [L], and initial head [L] are assigned to each cell. The cell size must be small enough so that physical properties can be considered homogeneous in the cell space, but large enough to achieve macroscopic description of the physical processes. The cell size is set as $\Delta s = \Delta x = \Delta y$.

The neighbourhood in CA models defines the area of process influence. Among those proposed in literature for two-dimensional CA with square tessellation, as that here presented, the *von Neumann* and *Moore* ones are the most adopted: the *von Neumann* neighbourhood considers the group of four cells in the four cardinal directions from the central one, while the *Moore* neighbourhood also includes the adjacent cells along diagonals (Figure 11.1). The *Von Neumann* neighbourhood has been chosen as the basis of the CA model implemented in the *FeST* groundwater module.

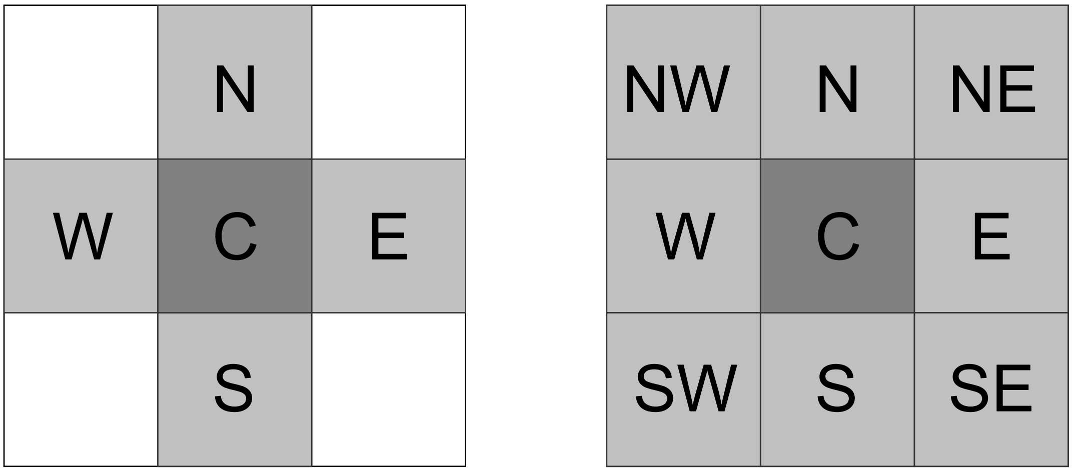

Figure 11.1 *Von Neumann* neighbourhood definition (left) that considers the group of four cells in the four cardinal directions from the central one, and (right) the *Moore* method that includes the adjacent cells along diagonals.

To give physical meaning to the rule defining water interaction between two adjacent cells, the *Darcy's* law is assumed. According to this, the water flux between central cell and, for example, northern cell, Q_{NC} [L^3 T^{-1}], is calculated as:

$$Q_{NC} = \frac{2T_N T_C}{T_N + T_C}\left(h_N^t - h_C^t\right) \qquad 11\text{-}1$$

where T_N and T_C represent, respectively, the transmissivity [L^2 T^{-1}] of northern cell and central cell, h_N^t and h_C^t represent, respectively, hydraulic head [L] of northern cell and central cell at previous time step, t. The term $\frac{2T_N T_C}{T_N + T_C}$ is the harmonic mean of transmissivity. It has been chosen because of its property to remove the impacts of large outliers by limiting the flux to the lower value of transmissivity. The flux is positive if entering the central cell.

The total flux entering the central cell is (Figure 11.2):

$$Q_C = Q_{NC} + Q_{EC} + Q_{SC} + Q_{WC} + W_C \qquad \text{11-2}$$

where W_C [L^3 T^{-1}] is the volumetric flux representing sources (+) or sinks (-).

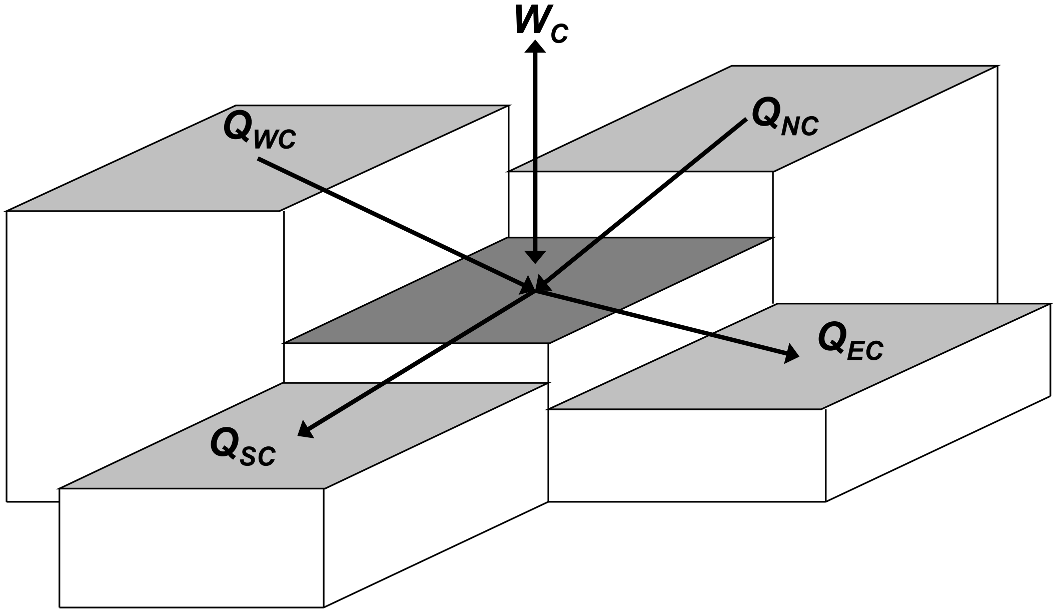

Figure 11.2 Scheme for the calculation of water fluxes between the central cell and the four adjacent cells. W_C is the volumetric flux representing source (entering the cell) or sink (exiting the cell).

Hydraulic head at central cell is updated for the subsequent time, $t + 1$, applying the discrete mass balance equation:

$$h_C^{t+1} = h_C^t + \frac{1}{S_y}\frac{Q_C}{\Delta s^2}\Delta t \qquad \text{11-3}$$

where Δt [T] is the time step.

Box 11.A Drawdown due to a constant pumping rate from a well

The numerical model was validated with respect to transient solution of head drawdown due to a constant pumping rate from a well. The first mathematical analysis was obtained by *Theis* (1935), under the assumptions that: (a) the aquifer is confined and compressible; (b) there is no source of recharge to aquifer; (c) water is released instantaneously from the aquifer as the head is lowered; (d) the well is fully penetrating.

The solution of unsteady distribution of drawdown is expressed by:

$$s(r,t) = \frac{Q}{4\pi T} \cdot W(u) \quad \text{11-4}$$

with

$$u = \frac{r^2 \cdot S_y}{4tT} \quad \text{11-5}$$

and

$$W(u) = \cdot \int_u^{\infty} \frac{e^{-z}}{z} \quad \text{11-6}$$

where s, is drawdown [L]; Q, is the constant pumping rate [L^3T^{-1}]; t, time since pumping began [T]; r, radial distance from the pumping well [L]. The integral expression is termed the well function. It is generally evaluated with analytical approximation. *Barry et al.* (2000) proposed a solution valid for all values of the argument of exponential integral. The *Theis* equation can be extended to describe flow in unconfined aquifers if the drawdown is small relative to the saturated thickness of the aquifer (*Jacob*, 1950).

The domain was setup applying Dirichlet condition on the entire boundary with hydraulic head h = 50 m, as well as initial condition. A well with a constant pumping rate of 0.001 m^3/s was placed in the central cell. The time step was set to 4000 s. Monitoring wells were placed along cardinal directions at a distance of 150, 200, 300 m from the pumping well. Two monitoring wells were placed on the 45 degrees direction at a distance of 127 and 170 m to investigate the eventuality that von Neumann neighbourhood could generate privileged directions. A further monitoring well was positioned at the cell adjacent to the boundary to verify if boundary condition could have influence on the cone of depression.

The following figure illustrates the depletion computed by the FeST model and MODFLOW-2000 compared to analytical solution for a 12 days duration after the beginning of the pumping. A very good fit can be observed in both monitoring wells along cardinal and diagonal direction.

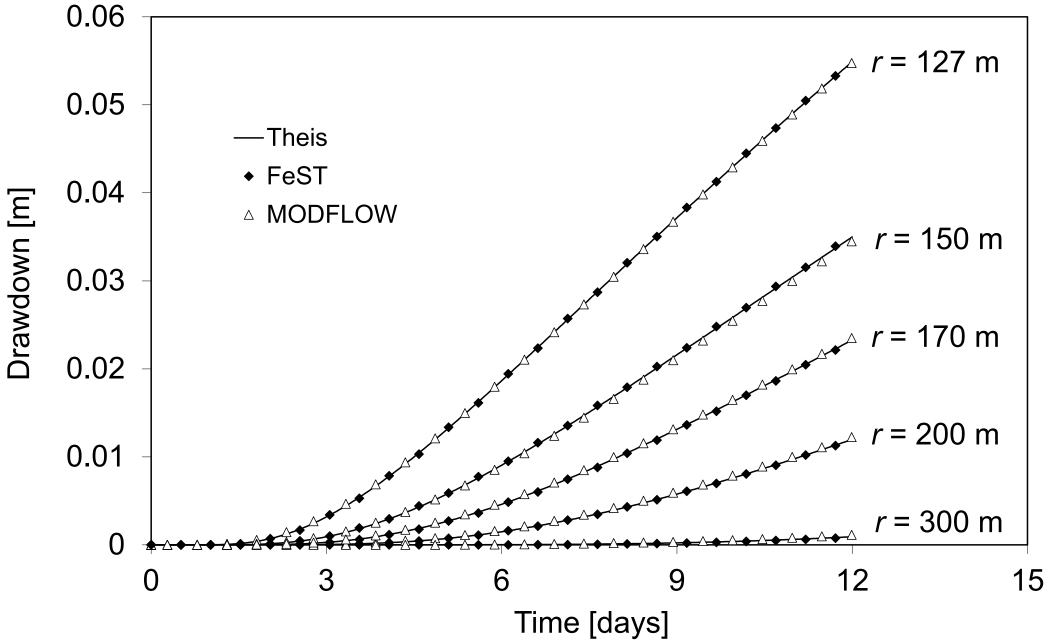

Comparison between analytical (*Theis*) and numerical solution (FeST and MODFLOW) for head drawdown due to a constant pumping rate of 0.001 m³/s at distance r = 150, 200 and 300 m from the well along cardinal direction, and r = 127 and 170 m on the 45° direction.

11.2 River-aquifer interaction

Rivers contribute water to or drain water from the ground-water system, depending on the head gradient between the river and the ground-water regime. Quantification of stream/aquifer hydraulics is an important problem in the study of alluvial aquifers, and river base flow assessment.

In all cells adjacent to river network, river interconnection is simulated, which allows stream to gain or lose water. The stream stage is used to calculate the flux between the stream and the aquifer system, proportional to the head gradient between the river and the aquifer and a streambed conductance parameter. When the aquifer head is above the bottom of the streambed, model assumes that the discharge through the streambed is proportional to the difference in hydraulic head between the stream and the aquifer:

$$Q = \frac{K_{sb} L\,W}{M}(h_w - h) \qquad 11\text{-}7$$

where Q is the discharge [L^3T^{-1}] with a downward flux assumed positive, K_{sb} is the streambed hydraulic conductivity [LT^{-1}], L is the stream length [L], W is the stream width [L], M is the streambed thickness [L], h_w is the hydraulic head in the stream [L], and h is the hydraulic head in the aquifer [L]. If the aquifer head drops below the bottom of the streambed, the model assumes that the seepage flow is no longer proportional to the aquifer head and becomes dependent on the water level in the stream and the streambed thickness:

$$Q = \frac{K_{sb}LW}{M}(H_w + M) \qquad 11\text{-}8$$

where H_w is the water level in the stream above the surface of the streambed [L]. At the beginning of each iteration, terms representing river seepage are added to the groundwater flow equation for each cell containing a river reach. Negative seepage occurs when river stage drops below aquifer head. Groundwater seepage is added to or subtracted from river flow accordingly.

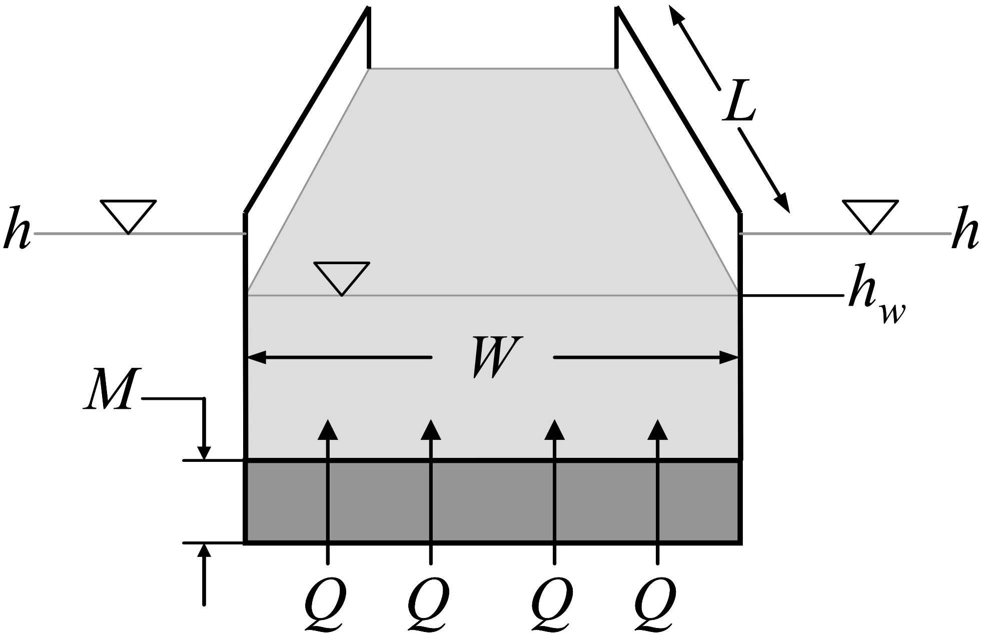

Figure 11.3 Conceptual representation of river-aquifer interconnection: Q is the discharge, L is the stream length, W is the stream width, M is the streambed thickness, h_w is the hydraulic head in the stream, and h is the hydraulic head in the aquifer.

Box 11.B Aquifer response to stream-stage variation

FeST capability to simulate the aquifer response to stream-stage variation is compared to the solution obtained by MODFLOW-2000.

The river interconnection was simulated using the RIVER package in MODFLOW-2000, which allows stream to gain or lose water. The stream stage is used to calculate the flux between the stream and the aquifer system, proportional to the head gradient between the river and the aquifer and a streambed conductance parameter, according to Equations 11-7 and 11-8, as represented in (Figure 11.3).

The domain was set up applying a constant head h = 50 m on the west and east boundaries, a Neumann type B condition on north and south boundaries, and an initial condition to perform the test. The time step was set to 4000 s. A river was placed with north-south direction at a distance of 250 m from the west boundary. River bottom was set at 46.5 m. Riverbed conductivity and thickness were $1 \cdot 10^{-5}$ m/s and 0.5 m, respectively, and the width of the river was equal to 5 m. Monitoring wells were placed at a distance of 100, 350, 450, 550, and 650 m from the west boundary.

The simulation time was 30 days and the river stage was supposed to increase with a sinusoidal variation to a maximum of 50 m as reported in Figure 14 where the comparison between *FeST* and MODFLOW-2000 results is performed. A good agreement can be observed.

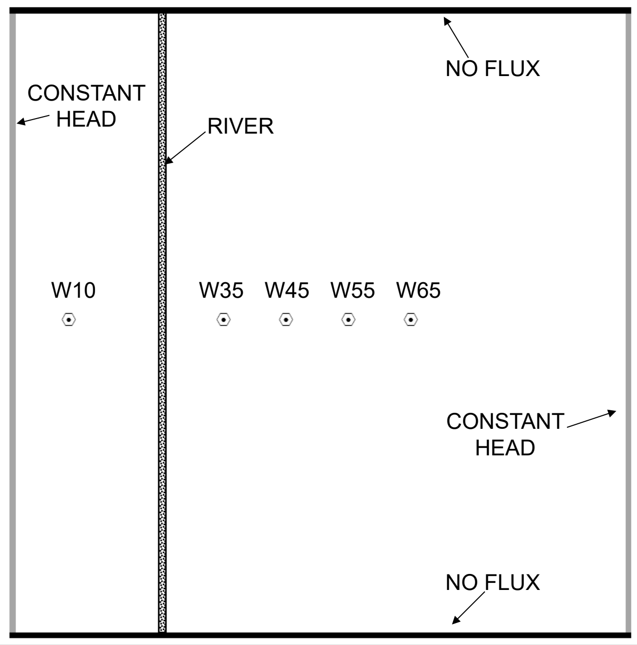

Scheme of the domain setup to perform the simulation of the aquifer response to stream-stage variation: location of river, boundary conditions and monitoring wells (W10, W35, W45, W55, and W65) is shown.

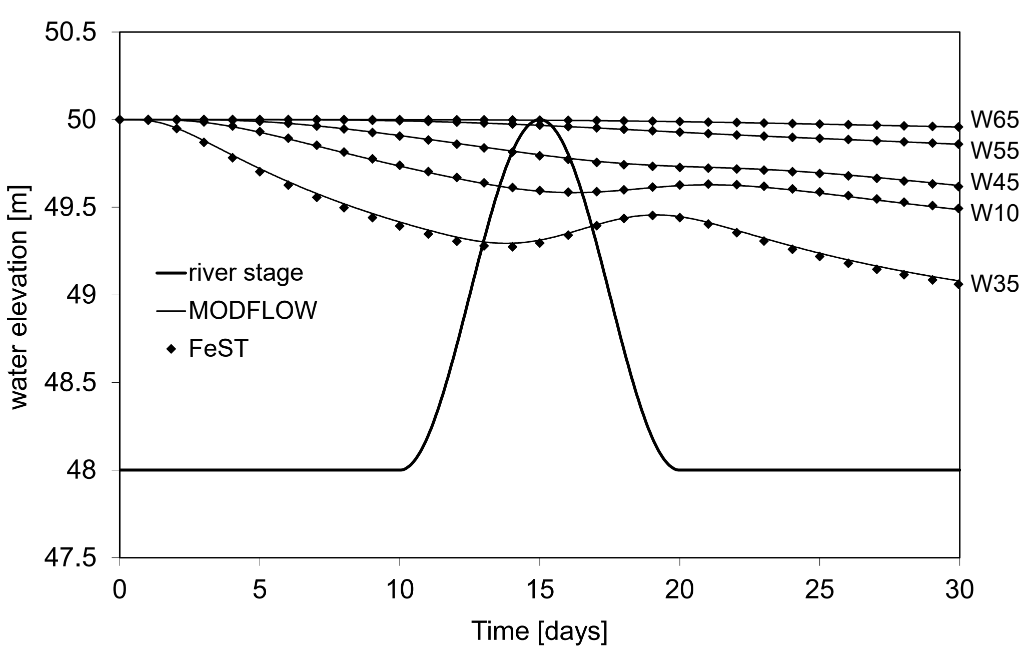

River stage variation and response of the water table at the five monitoringwells simulated by MODFLOW-2000 and FeST.

11.3 Boundary conditions

The final component of a CA model is the boundary condition that describes what happens at the outer cells of the lattice. The boundary conditions can be of *Dirichlet* or *Neumann* type (*Kinzelbach*, 1986). Dirichlet conditions specify the head h; *Neumann* conditions specify the flux, i.e., the head gradient $\partial h/\partial x$ orthogonal to the boundary (Figure 11.4).

In Neumann type boundary cells, the subsurface flow coming from hydrological simulation is transformed into a flux entering unconfined aquifer along the border. Dirichlet type boundary condition cells are set along the border of the aquifer where piezometric head is considered constant in time.

In groundwater domain, percolation depurated from capillary rise computed by hydrological model is transformed into net recharge to groundwater storage.

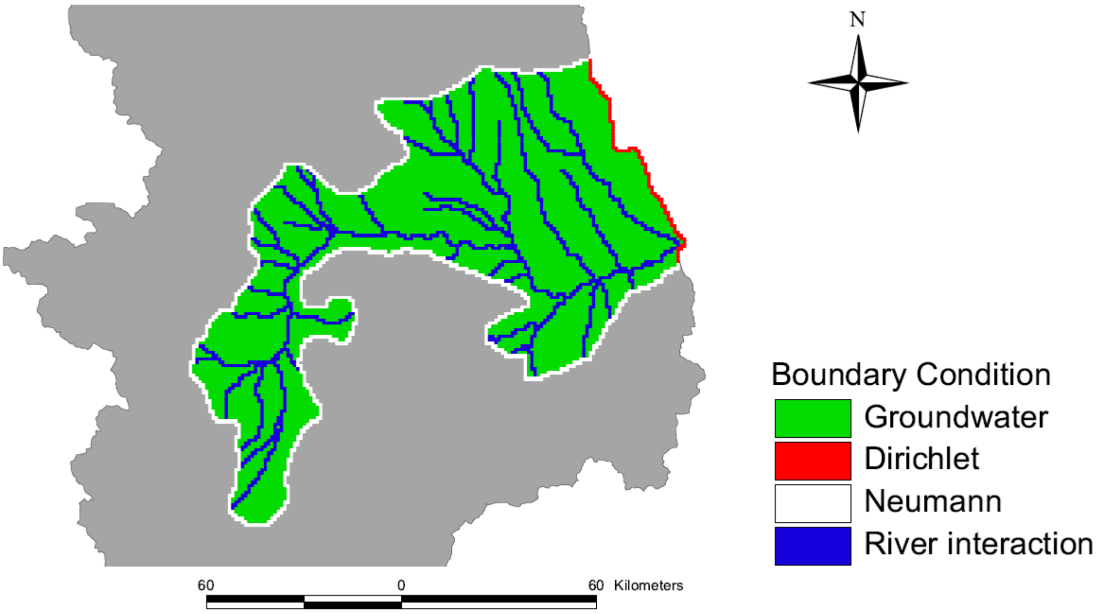
N
Boundary Condition
Groundwater
Dirichlet
Neumann
River interaction
60
0
60 Kilometers

Figure 11.4 Aquifer conceptual model: scheme of boundary conditions. In Neumann type boundary cells, the subsurface flow coming from hydrological simulation is transformed into a flux entering unconfined aquifer along the border. Dirichlet type boundary condition cells are set along the eastern border of the aquifer that continues downward into the Po valley.

CHAPTER 12

IRRIGATION MANAGEMENT

BOX 12.A Irrigation management in Italy (tesi Mouna chapter 1)

About 75% of irrigated areas in Europe are located in Greece, Italy, Portugal and Spain (EU-27). Irrigation in Italy is considered as an old tradition. The first constructed channel to divert water for irrigation was constructed in 1179 (The great channel that connects Milan to Lago Maggiore) and in 1225 for the “Muzza” and “Fozza di Pazzolo” (Martucelli, 1997). In Italy the irrigation is managed by consortiums. In 2009-2010 the water used for irrigation was about 11.618MCUM (Million Cubic Meters). About 59% of water devoted for irrigation is used in northern Italy (ISTAT, 2014). Lombardy region has the highest irrigated area with 600.000 ha that corresponds to 23.6% of the total irrigated surface in Italy. About 62% of irrigation is applied through low efficiency irrigation techniques (Surface irrigation). The sprinkler and drip irrigated area presents consequently 33.8% and 9.6% of the total irrigated area. Water in Italy and particularly in the north is considered an abundant resource (ISTAT, 2014). Within the Po basin the total available water was estimated to 20.586 Thousand cubic meters (IRSA, 1999). According to the ISTAT (2014), the highest percentage of irrigation water is used for rise cultivation with 39.8% of the total irrigation water. The second main irrigated crop is the maize consuming around 21.4% of total irrigation water. This implies an adequate use of water resources to produce more with less water. Irrigation management policies aims at reducing non-beneficial water uses (Pereira et al., 2002).

Proper irrigation management requires that growers’ decision should be taken based on some indicators based on monitoring of soil water status. Irrigation scheduling aims at determining how much water to apply and when to irrigate (Rhenals and Bras, 1981).The proper amount of irrigation and timing are based on several factors: soil characteristics, plant characteristics and climatic conditions. Many methods to schedule the irrigation have been suggested in the literature based on evapotranspiration or soil moisture. Soil moisture based irrigation scheduling has been widely implemented. A combined use of monitoring and modeling allowed the use of such simulations coupled with meteorological forecasts for irrigation management purposes (Ceppi et al., 2014).

The models accuracy when implemented for this aim is very important. Main limitation of these models depends on implemented input parameters. Right decisions are taken based on right data while uncertain climatic and soil data leads to unreliable results and thus inadequate decisions. A required knowledge of the soil is highly recommended to define the thresholds based on which the decision to irrigate is taken.

The limitation of these decision support tools for irrigation scheduling in northern Italy is constrained by the non-flexibility of water delivery system that is a rotation irrigation scheme. Water is delivered to farms through collective irrigation canal. Irrigation turns, discharge, duration are fixed by the consortium. In such case due to the rigidity of the delivery systems, farmers irrigate whenever the water is available and end up by over irrigating their farms (Pereira et al., 2002). Both farmers and irrigation schemes managers should be aware about the negative impacts of such practices (lack of oxygen for plants, leachate of fertilizers, water losses...etc.). Allowing more flexibility in the delivery system will allow implementation of better irrigation schedules thus reducing miss-use of resources.

CHAPTER 13

PLANTS GROWTH

REFERENCES

Adornado, H.A.; Yoshida, M. GIS-based watershed analysis and surface run-off estimation using curve number (CN) value. J. Environ. Hydrol. 2010, 18, 1–10.

Aleynikov A A, Popovnin V V, Voytkovskiy K F, Zolotaryov Y A. 2002. Indirect estimation of the Djankuat Glacier volume based on surface topography. Nordic Hydrology 33(1): 95-110.

Allen, R.G., Pereira, L.S., Raes, D., Smith, M. (1998). "Crop evapotranspiration – guidelines for computing crop water requirements – FAO Irrigation and Drainage Paper 56." FAO, 1998. ISBN 92-5-104219-5.

Amengual,A., Carrió, D.S., Ravazzani, G., and Homar, V.. A comparison of ensemble strategies for flash flood forecasting: the 12 october 2007 case study in valencia, spain. Journal of Hydrometeorology, 18(4):1143–1166, 2017.

Arnold, J.G.; Moriasi, D.N.; Gassman, P.; Abbaspour, K.C.; White, M.J.; Srinivasan, R.; Santhi, C.; Harmel, R.D.; van Griensven, A.; Van Liew, M.W.; et al. SWAT: Model use, calibration, and validation. Trans. ASABE 2012, 14, 533–538.

Assouline, S. (2013). Infiltration into soils: Conceptual approaches and solutions. Water Resources Research, 49, 1755– 1772. https://doi.org/10.1002/wrcr.20155

Avanzi, F., Ercolani, G., Gabellani, S., Cremonese, E., Pogliotti, P., Filippa, G., Morra di Cella, U., Ratto, S., Stevenin, H., Cauduro, M., and Juglair, S.: Learning about precipitation lapse rates from snow course data improves water balance modeling, Hydrol. Earth Syst. Sci., 25, 2109–2131, https://doi.org/10.5194/hess-25-2109-2021, 2021.

Barry RG, Chorley RJ (1987) Atmosphere, weather and climate, 5th edn. Routledge, London.

Barry, D.A., Parlange, J.-Y., and Li, L, 2000. Approximation for the exponential integral (Theis well function). Journal of Hydrology, 227, 287-591.

Bates, P.D., and De Roo, A.P.J., 2000. A simple raster-based model for flood inundation simulation. Journal of Hydrology, 236, 54-77.

Beasley, D.B.; Huggins, L.F.; Monke, E.J. ANSWERS: A model for watershed planning. Trans. ASAE 1980, 23, 938–944.

Boscarello, L., Ravazzani, G., Rabuffetti, D., & Mancini, M.. (2014). Integrating glaciers raster-based modelling in large catchments hydrological balance: the Rhone case study. Hydrological processes, 28, 496–508.

Brooks, R.H., and Corey A.T., Properties of porous media affecting fluid flow, J. Irrig. Drainage Div. A.S.C.E. IR2; 61-88, 1966.

Brutsaert, W. (2005). Hydrology: An introduction (pp. 305– 365). Cambridge, New York: Cambridge University Press. https://doi.org/10.1017/CBO9780511808470

Carnahan, B., Luther, H. A., and Wilkes, J. O. (1969). Applied Numerical Methods. John Wiley & Sons: New York; 604.

Ceppi, A., Gambini, E., Lombardi, G., Ravazzani, G., & Mancini, M.. (2022). Sol40: forty years of simulations under climate and land use change. Water, 14(6).

Ceppi, A., Ravazzani, G., Corbari, C., Salerno, R., Meucci, S., & Mancini, M.. (2014). Real-time drought forecasting system for irrigation management. Hydrology and earth system sciences, 18(9), 3353–3366.

Chen J, Ohmura A. 1990. Estimation of Alpine glacier water resources and their change since the 1870s. Hydrology in Mountain Regions. I – Hydrological Measurement; the Water Cycle. Proceedings of two Lausanne Symposia. IAHS Publ. 193: 127-135.

Cheng, F.-Y., Georgakakos, K.P. (2011), Wind speed interpolation in the vicinity of the Panama Canal, Meteorol. Appl., 18, 459–466.

Chow, V. T., Maidment, D. R., and Mays, L. W. (1988). Applied Hydrology. McGraw-Hill, New York.

Collis-George, N. Infiltration equations for simple soil systems. Water Resour. Res. 1977, 13, 395–403.

Corbari, C., & Mancini, M. (2014). Calibration and validation of a distributed energy–water balance model using satellite data of land surface temperature and ground discharge measurements. Journal of hydrometeorology, 15(1), 376-392.

Corbari, C., Ravazzani, G., & Mancini, M. (2011). A distributed thermodynamic model for energy and mass balance computation: FEST–EWB. Hydrological Processes, 25(9), 1443-1452.

Corbari, C., Ravazzani, G., Perotto, A., Lanzingher, G., Lombardi, G., Quadrio, M., Mancini, M., & Salerno, R.. (2022). Weekly monitoring and forecasting of hydropower production coupling meteo-hydrological modeling with ground and satellite data in the italian alps. Hydrology, 9(2).

Cressie, N., 1985. Fitting variogram models by weighted least squares. Mathematical Geology 17 (5), 563±586.

D'Ambrosio, D., Di Gregorio, S., Gabriele, S., and Gaudio, R., 2001. A Cellular Automata Model for Soil Erosion by Water. Physics and Chemistry of the Earth - Part B, 26, 33-40.

Di Gregorio, S., and Serra, R., 1999. An empirical method for modelling and simulating some complex macroscopic phenomena by cellular automata. Future Generation Computer Systems, 16, 259-271.

Di Gregorio, S., Serra, R., and Villani, M., 1999. Applying cellular automata to complex environmental problems: The simulation of the bioremediation of contaminated soil. Theoretical Computer Science, 217, 131-156.

Di Stefano, C., and V. Ferro (1997). “Estimation of evapotranspiration by Hargreaves formula and remote sensed data in semi-arid Mediterranean areas.” J. Agric. Eng. Res., 68, 189–199.

Diskin, M. H., & Nazimov, N. (1996). Ponding time and infiltration capacity variation during steady rainfall. Journal of Hydrology, 178(1–4), 369– 380. https://doi.org/10.1016/0022-1694(95)02798-X

Dodson, R. and Marks, D.. (1997). Daily air temperature interpolated at high spatial resolution over a large mountainous region, Climate Research, 8 (1), 1-20.

Ercolani, G., Gorlé, C., García-Sánchez, C., Corbari, C., Mancini, M. (2015) RAMS and WRF sensitivity to grid spacing in large eddy simulations of the dry convective boundary layer, Computers and Fluids, 123, 54–71.

Famiglietti, J.S., & Wood, E.F. (1994). Multiscale modeling of spatially variable water and energy balanceprocess. Water Resour. Res., 30, 3061–3078, https://doi.org/10.1029/94WR01498.

FAO. (1998). Chapter 1 - Introduction to evapotranspiration. http://www.fao.org/3/X0490E/x0490e04.htm

Farinotti D, Huss M, Bauder A, Funk M, Truffer M. 2009. A method to estimate the ice volume and ice-thickness distribution of alpine glaciers. Journal of Glaciology 55(191): 422-430

Feddes, R.A.; Kabat, P.; Van Bakel, P.J.T.; Bronswijk, J.J.B.; Halbertsma, J. Modeling soil water dynamics in the saturated zone—State of the art. J. Hydrol. 1988, 100, 69–111.

Feki, M., Ravazzani, G., Ceppi, A., Pellicone, G., & Caloiero, T.. (2021). Integration of forest growth component in the fest-wb distributed hydrological model: the bonis catchment case study. Forests, 12(12).

Fiorentini M, Orlandini S. Robust numerical solution of the reservoir routing equation. Adv Water Resour 2013;59:123–32.

Forthofer, J.M., Butler, B.W., Wagenbrenner, N.S. (2014) A comparison of three approaches for simulating fine-scale surface winds in support of wildland fire management. Part I. Model formulation and comparison against measurements. Int. J. Wildland Fire, 23, 969-931. doi:10.1071/WF12089.

Gassman, P.W., M. R. Reyes, C. H. Green, J. G. Arnold. 2007. The Soil and Water Assessment Tool: Historical Development, Applications, and Future Research Directions. Transactions of the ASABE. Vol. 50(4): 1211-1250.

Gates DM (1980) Biophysical ecology. Springer, New York, page 101, eq. 6.6

Gaudard, L., Romerio, F., Valle, D. F., Gorret, R., Maran, S., Ravazzani, G., Stoffel, M., & Volonterio, M.. (2014). Climate change impacts on hydropower in the Swiss and Italian Alps. Science of the total environment, 493, 1211–1221.

González-Longatt, F., Medina, H., Serrano González, J. (2015) Spatial interpolation and orographic correction to estimate wind energy resource in Venezuela, Renewable and Sustainable Energy Reviews, 48, 1-16.

Gotway, C.A., 1991. Fitting semivariogram models by weighted least squares. Computers & Geosciences 17 (1), 171±172.

Gowdish, L. and Muñoz-Carpena, R. (2009), An Improved Green–Ampt Infiltration and Redistribution Method for Uneven Multistorm Series. Vadose Zone Journal, 8: 470-479. https://doi.org/10.2136/vzj2008.0049

Green,W.H.; Ampt, G.A. Studies on soil physics I. Flow of air and water through soils. J. Agric. Sci. 1911, 4, 1–24

Haghiabi, A. H., Heidarpourand M. and Habili, J. (2011).A new method for estimating the parameters of Kostiakov and modified Kostiakov infiltration equations.World Applied Sciences Journal. 15(1): 129 –135

Hargreaves G.H., Samani Z.A., 1985. Reference crop evapotranspiration from temperature: Applied Engineering in Agriculture, 1: 96-99.

Hargreaves, G. H. (1994). "Defining and using reference evapotranspiration." J. Irrig. Drain. Eng., 120(6), 1132–1139.

Hargreaves, G.H., and Z.A. Samani (1982). "Estimating potential evapotranspiration." J. Irrig. Drain. Eng., ASCE, 108(3), 223-230.

Hartkamp, A.D., K. De Beurs, A. Stein, e J.W. White. Interpolation techniques for climate variables. Mexico, DF (Mexico), CIMMYT, 1999.

Helbig, N., Mott, R., van Herwijnen, A., Winstral, A., Jonas, T. (2017) Parameterizing surface wind speed over complex topography, Journal of Geophysical Research: Atmospheres, J. Geophys. Res. Atmos., 122, 651–667, doi:10.1002/2016JD025593.

Hock R, Jansson P, Braun L N. 2005. Modelling the response of mountain glacier discharge to climate warming. Global Change and Mountain Region. 243-252

Hock R. 2003. Temperature index melt modelling in mountain areas. Journal of Hydrology 282: 104-115.

Hoel, P.G., 1984. Introduction to Mathematical Statistics, 5th ed. John Wiley & Sons, Singapore, 435 pp.

Hoelzle M, Haeberli W, Dischl M, Peschke W. 2003. Secular glacier mass balance derived from cumulative glacier length changes. Global and Planetary Change 36: 295-306

Horritt, M.S., and Bates, P.D., 2001. Predicting floodplain inundation: raster-based modelling versus the finite element approach. Hydrological Processes, 15, 825-842.

Horton P, Schaefli B, Mezghani A, Hingray B, Musy A. 2006. Assessment of climate-change impacts on alpine discharge regimes with climate model uncertainty. Hydrological Processes 20: 2091-2109.

Huggins, L.F.; Monke, E.I. The Mathematical Simulation of the Hydrology of Small Watersheds; Technical Report No. 1; PurdueWater Resources Centre: West Lafayette, Indiana, 1966.

Huss M, Farinotti D, Bauder A, Funk M. 2008. Modelling runoff from highly glacierized alpine drainage basins in a changing climate. Hydrological Processes 22: 3888-3902.

Immerzeel, W. W., Droogers, P., & Gieske, A. S. M. (2006). Remote sensing and evapotranspiration mapping : state of the art. FutureWater.

http://ezproxy.utwente.nl:2048/login?url=https://webapps.itc.utwente.nl/library/2006/tech_rep/gieske_rem.pdf

Iovine, G., D'Ambrosio, D., and Di Gregorio, S., 2005. Applying genetic algorithms for calibrating a hexagonal cellular automata model for the simulation of debris flows characterised by strong inertial effects. Geomorphology, 66, 287-303.

Iqbal, M.: An introduction to solar radiation, Academis Press, Canada, Ontario, 1983.

Jacob, C. E., 1950. Flow of groundwater, in H. Rouse Ed. Engineering Hydraulics, Wiley, New York.

Jian, X., Olea, R.A., Yu, Y., 1996. Semivariogram modelling by weighted least squares. Computers & Geosciences 22 (3), 387±397.

Jiménez-Hornero, F.J., Giráldez, J.V., and Laguna, A., 2003. A description of water and sediment flow in the presence of obstacles with a two-dimensional, lattice BGK-cellular automata model. Water Resources Research, 39(12), 1369, doi:10.1029/2003WR002302.

Kale, R.V., Sahoo, B. Green-Ampt Infiltration Models for Varied Field Conditions: A Revisit. Water Resour Manage 25, 3505–3536 (2011). https://doi.org/10.1007/s11269-011-9868-0

Kilzenbach, W., 1986. Groundwater modelling: an introduction with sample programs in BASIC. Developments in Water Science No. 25, Elsevier, Amsterdam, The Netherlands.

Klok E J, Jasper K, Roelofsma P, Gurtz J, Badoux A. 2001. Distributed hydrological modelling of a heavily glaciated Alpine river basin. Hydrological Sciences 46(4): 553-570.

Konz M, Seibert J. 2010. On the value of glacier mass balances for hydrological model calibration. Journal of Hydrology 385: 238-246.

Kostiakov, A. N. (1932). On the dynamics of the coefficient of water-percolation in soils and on the necessity for studying it from a dynamic point of view for purposes of amelioration.Transactions Congress International Society for Soil Science, 6th, Moscow, Part A: 17-21.

Kreith, F., and Kreider, J. F., 1978, Principles of Solar Engineering, New York: McGraw-Hill

Lasdon, L.S., Waren, A.D., Jain, A., and Ratner, M. (1978). "Design and Testing of a Generalized Reduced Gradient Code for Nonlinear Programming." ACM Transactions on Mathematical Software, 4(1), 34-50.

Lassabatere, L.; Angulo-Jaramillo, R.; Soria-Ugalde, J.M.; Simunek, J.; Haverkamp, R. Numerical evaluation of a set of analytical infiltration equations. Water Resour. Res. 2009, 45.

Li H, Ng F, Li Z, Qin D, Cheng G. 2012. An extended "perfect plasticity" method for estimating ice thickness along the flow line of mountain glaciers. Journal of Geophysical Research 117: F01020

Liston, G. E. and Elder, K. (2006) A meteorological distribution system for high-resolution terrestrial modeling (MicroMet), J. Hydrometeorol.,7, 217–234.

Liston, G.E., Sturm, M. (1998) A snow-transport model for complex terrain, Journal of Glaciology, 44(148), 498-516.

Liu B.Y.H., Jordan R.C. (1960) The interrelationship and characteristic distribution of direct, diffuse, and total solar radiation. Solar Energy,4 (1), 1–19

Mahring W., 1970. Verdunstungsstudien am neusiedler See. Theor. Appl. Clim., 18: 1-20.

Makkink G.F., 1957. Testing the Penman formula by means of lysimeters. J. Inst. Water Eng., 11: 277-288

Male DH, Granger RJ. 1981. Snow surface energy exchange. Water Resources Research 17(3): 609–627.

Malguzzi, P., Grossi, G., Buzzi, A., Ranzi, R., Buizza, R. (2006) The 1966 "century" flood in Italy: A meteorological and hydrological revisitation. J. Geophys. Res., 111, D24106, doi:10.1029/2006JD007111.

Mancini, M.. (1990). La modellazione distribuita della risposta idrologica: effetti della variabilità spaziale e della scala di rappresentazione del fenomeno dell'assorbimento. PhD thesis. Politecnico di Milano, Istituto di idraulica

Marshall, E., and Randhir, T.O., 2008. Spatial modelling of land cover change and watershed response using Markovian cellular automata and simulation. Water Resources Research, 44, W04423, doi:10.1029/2006WR005514.

Martinec, J. & Rango, A.: Parameter values for snowmelt runoff modelling, J. Hydrol. 84 3/4, 197–219, 1986.

Martinec, J.: The degree-day factor for snowmelt runoff forecasting, proceedings of general assembly of Helsinki commission on surface waters, IAHS Publ. 51, 1960.

Matheron, G., et al. (1965) Les variables régionalisées et leur estimation: Une application de la théorie des fonctions aléatoires aux sciences de la nature. Masson, Paris, 305 pp.

McMahon, T. A., Peel, M. C., Lowe, L., Srikanthan, R., & McVicar, T. R. (2013). Estimating actual, potential, reference crop and pan evaporation using standard meteorological data: A pragmatic synthesis. Hydrology and Earth System Sciences, 17(4), 1331–1363. https://doi.org/10.5194/hess-17-1331-2013

Mein RG, Larson CL (1973) Modeling infiltration during a steady rain. Water Resour Res 9(2):384–394

Mendicino, G., Senatore, A., Spezzano, G., and Straface, S., 2006. Three-dimensional unsaturated flow modeling using cellular automata. Water Resources Research, 42, W11419, doi:10.1029/2005WR004472.

Merdun, H., 2012. Effects of Different Factors on Water Flow and Solute Transport Investigated by Time Domain Reflectometry in Sandy Clay Loam Field Soil.Water, Air and Soil Pollution, 223: 4905. Doi: 10.1007/s11270-012-1246-x

Milly, P. C. D. (1986). An event-based simulation model of moisture and energy fluxes at a bare soil surface. Water Resources Research, 22(12), 1680– 1692. https://doi.org/10.1029/WR022i012p01680

Milly, P. C. D. (1986). An event-based simulation model of moisture and energy fluxes at a bare soil surface. Water Resources Research, 22(12), 1680– 1692. https://doi.org/10.1029/WR022i012p01680.

Milner A M, Brown L E, Hannah D M. 2009. Hydroecological response of river systems to shrinking glaciers. Hydrological Processes 23: 62-77.

Mishra, S.K. , Tyagi,J.V., Singh, V.P., 2003 Comparison of infiltration models Hydrolog. Processes, 17: 2629–2652.

Montaldo, N., Ravazzani, G., & Mancini, M.. (2007). On the prediction of the toce alpine basin floods with distributed hydrologic models. Hydrological processes, 21, 608–621

Monteith, J. L. (1965). "Evaporation and environment". Symposia of the Society for Experimental Biology. 19: 205–234. PMID 5321565

Moretti, G.; Montanari, A. Inferring the flood frequency distribution for an ungauged basin using a spatially distributed rainfall-runoff model. Hydrol. Earth Syst. Sci. 2008, 12, 1141–1152.

Nelder, J.A., Mead, R., 1965. A simplex method for function minimization. Computer Journal 7, 308±313.

Nye J F. 1952. The mechanics of glaciers flow. Journal of Glaciology 2(12): 82-93

Oke, T.R., Boundary layer climates, Second edition, Routledge, 1987. Appendix A1, eq. A1.2

Pardo-Iguzquiza, E. VARFIT: a fortran-77 program for fitting variogram models by weighted least squares. Computers & Geosciences, 25, 251-261, 1999.

Pari H. and Nofziger, D. (1987). Analytical solution for punctual kriging in one dimension1. Soil Science Society of America Journal - SSSAJ, 51, 01.

Parlange, M.B., J.D. Albertson, W.E. Eichinger, A.T. Cahill and T.J.Jackson, Evaporation: Use of fast response turbulence sensors, raman lidar and passive microwave remote sensing, in Vadose Zone Hydrology: Cutting Across Disciplines, M.B. Parlange and JW Hopmans (eds.), Oxford UniversityPress, 260-278, 1999.

Parsons, J.A., and Fonstad, A., 2007. A cellular automata model of surface water flow, Hydrological Processes, 21, 2189-2195.

Pellicone, G, Caloiero, T, Modica, G, Guagliardi, I. Application of several spatial interpolation techniques to monthly rainfall data in the Calabria region (southern Italy). Int J Climatol. 2018; 38: 3651– 3666. https://doi.org/10.1002/joc.5525

Penman H.L., 1948. Natural evaporation from open water, bare soil and grass. Proc. R. Soc. Lond. A, 193: 120-145.

Philip, J.R. Numerical solution of equations of the diffusion type with diffusivity concentration-dependent II. Aust. J. Phys. 1957, 10, 29–42.

Priestley, C. H. B. and Taylor, R. J.: 1972, ‘On the Assessment of Surface Heat Flux and Evaporation Using Large-Scale Parameters’, Mon. Wea. Rev. 100, 81–92.

Rabuffetti, D., Ravazzani, G., Corbari, C., & Mancini, M.. (2008). Verification of operational quantitative discharge forecast (QDF) for a regional warning system – the AMPHORE case studies in the upper Po river. Natural hazards and earth system sciences, 8, 161–173.

Ranzi R., Rosso R., Un modello idrologico distribuito, su base fisica, dello scioglimento nivale, Master thesis (in italian), Politecnico di Milano,1989.

Ravazzani, G., Barbero, S., Salandin, A., Senatore, A., & Mancini, M.. (2015). An integrated hydrological model for assessing climate change impacts on water resources of the upper po river basin. Water resources management, 29(4), 1193-1215.

Ravazzani, G., Ceppi, A., & Davolio, S.. (2020). Wind speed interpolation for evapotranspiration assessment in complex topography area. Bulletin of atmospheric science and technology, 1, 13–22.

Ravazzani, G., Corbari, C., Ceppi, A., Feki Mouna, Mancini, M., Ferrari, F., Gianfreda, R., Colombo, R., Ginocchi, M., Meucci, S., De Vecchi, D., Dell'Acqua, F., & Ober, G.. (2017). From (cyber)space to ground: new technologies for smart farming. Hydrology research, 48(3), 656-672.

Ravazzani, G., Corbari, C., Morella, S., Gianoli, P., & Mancini, M.. (2012). Modified Hargreaves-Samani equation for the assessment of reference evapotranspiration in Alpine river basins. Journal of irrigation and drainage engineering, 138(7), 592–599.

Ravazzani, G., Corbari, C., Morella, S., Gianoli, P., and Mancini, M. (2012), Modified Hargreaves-Samani equation for the assessment of reference evapotranspiration in Alpine river basins, Journal of Irrigation and Drainage Engineering, 138, 592- 599.

Ravazzani, G., Ghilardi, M., Mendlik, T., Gobiet, A., Corbari, C., Mancini, M. (2014), Investigation of Climate Change Impact on Water Resources for an Alpine Basin in Northern Italy: Implications for Evapotranspiration Modeling Complexity. PLoS ONE, 9(10): e109053. doi:10.1371/journal.pone.0109053.

Ravazzani, G., Ghilardi, M., Mendlik, T., Gobiet, A., Corbari, C., & Mancini, M.. (2014). Investigation of climate change impact on water resources for an alpine basin in northern Italy: implications for evapotranspiration modeling complexity. Plos one, 9(10), e109053.

Ravazzani, G., Gianoli, P., Meucci, S., & Mancini, M.. (2014). Indirect estimation of design flood in urbanized river basins using a distributed hydrological model. Journal of hydrologic engineering, 19(1), 235–242.

Ravazzani, G., Rametta, D., & Mancini, M.. (2011). Macroscopic cellular automata for groundwater modelling: a first approach. Environmental modelling & software, 26(5), 634–643.

Ravazzani, G., Rametta, D., & Mancini, M.. (2011). Macroscopic cellular automata for groundwater modelling: a first approach. Environmental modelling & software, 26(5), 634–643.

Ravazzani, G.. (2013). Mosaico, a library for raster based hydrological applications. Computers & geosciences, 51, 1–6.

Ravazzani, G.; Mancini, M.; Giudici, I.; Amadio, P. Effects of soil moisture parameterization on a real- time flood forecasting system based on rainfall thresholds. In Quantification and Reduction of Predictive Uncertainty for Sustainable Water Resources Management (Proceedings of Symposium HS2004 at IUGG2007, Perugia, July 2007); IAHS Press: Wallingford, UK, 2007; pp. 407–416

Ravi, V., and Williams, J.R., 1998. Estimation of infiltration rate in the vadose zone: compilation of simple mathematical models, Vol. I. US Environmental Protection Agency, EPA/600/R-97/128a, 26 pp.

Rawls, W.J., Brakensiek, D.L. and Saxton, K.E. 1982. Estimation of soil water properties. Trans. ASAE 25, 1316–1330.

Rawls, W.J., Brakensiek, D.L., and Miller, N. 1983. Green–Ampt infiltration parameters from soils data. J. Hydraul. Eng. 109, 62–70.

Richards, L.A. Capillary conduction of liquids in porous mediums. Physics 1931, 1, 318–333.

Richards, L.A. Capillary conduction of liquids in porous mediums. Physics 1931, 1, 318–333.

Robeson, S.M. (1995) Resampling of network-induced variabil- ity in estimates of terrestrial air temperature change. Clim Change 29:213-229.

Ross, P.J. Modeling soil water and solute transport—Fast simplified numerical solutions. Agron. J. 2003, 95, 1352–1361.

Rotach, M. W., A. Gohm, M. N. Lang, D. Leukauf, I. Stiperski, and J. S. Wagner (2015), On the vertical exchange of heat, mass, and momentum over complex, mountainous terrain, Front. Earth Sci., 3, 76, doi:10.3389/feart.2015.00076.

Ryan, B. C. (1977), A mathematical model for diagnosis and prediction of surface winds in mountainous terrain, J. Appl. Meteorol., 16(6), 571–584.

Salandin, A., Rabuffetti, D., Barbero, S., Cordola, M., Volontè, G. and Mancini, M.: Il lago effimero sul ghiacciaio del Belvedere: monitoraggio e simulazione numerica del fenomeno finalizzata alla previsione e gestione dell'emergenza, Neve e Valanghe 51, 58-65, 2004.

Samani, Z. A., and M. Pessarakli (1986). "Estimating potential crop evapotranspiration with minimum data in Arizona." Trans. ASAE, 29, 522–524.

Schaefli B, Hingray B, Niggli M, Musy A. 2005. A conceptual glacio-hydrological model for high mountainous catchments. Hydrology and Earth System Sciences 9: 95-109.

Schulte, A., Suthfeld, R., Vogt, B. (2018): E-Learning Project IWRM - Integrated Water Resources Management. Department of Earth Sciences, Freie Universitaet Berlin. https://www.geo.fu-berlin.de/en/v/iwrm/index.html

SCS, Soil Conservation Services. (1985) National Engineering Handbook, Section 4: Hydrology, Soil Conservation Service. USDA, Washington DC.

Sharpley, A.N.; Williams, J.R. EPIC—Erosion/Productivity Impact Calculator. I. Model Documentation; US Department of Agriculture Technical Bulletin; US Department of Agriculture: Washington, DC, USA, 1990.

Shepard, D. (1968). A two-dimensional interpolation function for irregularly-spaced data. Proceedings of the 1968 ACM National Conference. 517–524. doi:10.1145/800186.810616.

Shuttleworth, W. J. (1993). "Evaporation." in Handbook of hydrology, edited by D. R. Maidment, pp. 4.1-4.53, McGraw-Hill, New York.

Sivapalan, M.; Beven, K.; Wood, E.F. On hydrologic similarity, 2A scaled model of storm runoff production. Water Resour. Res. 1987, 23, 2266–2278.

Smith, R.E.; Parlange, J.Y. A parameter-efficient hydrologic infiltration model. Water Resour. Res. 1978, 14, 533–538. [CrossRef]

Soulis, K.X.; Valiantzas, J.D. SCS-CN parameter determination using rainfall-runoff data in heterogeneous watersheds—The two-CN system approach. Hydrol. Earth Syst. Sci. 2012, 16, 1001–1015.

Swenson, S.C., Clark, M., Fan, Y., Lawrence, D.M., and Perket, J. Representing intrahillslope lateral subsurface flow in the Community Land Model, J. Adv. Model. Earth Sy.,11, 4044–4065, https://doi.org/10.1029/2019MS001833, 2019.

Tarboton D. G., Chowdhury T. G. and Jackson Thomas H.: A Spatially Distributed Energy Balance Snowmelt Model, Utah Water Research Laboratory, 1994.

Theis, C.V., 1935. The relation between the lowering of the piezometric surface and the rate and duration of discharge of a well using groundwater storage, Transactions of the American Geophysical Union,16, 519–524.

Thiessen, A.H. (1911) Precipitation averages for large areas. Monthly Weather Review, 39(7), 1082– 1089. https://doi.org/10.1175/1520-0493(1911)39<1082b:PAFLA>2.0.CO;2

Thornthwaite, C.W.. 1948. An approach toward a rational classification of climate. Geogr. Rev. 38: 55- 94 https://doi.org/10.2307/210739

Tinet, A.-J.; Chanzy, A.; Braud, I.; Crevoisier, D.; Lafolie, F. Development and evaluation of an efficient soil-atmosphere model (FHAVeT) based on the Ross fast solution of the Richards equation for bare soil conditions. Hydrol. Earth Syst. Sci. 2015, 19, 969–980.

Todini, E., 2007. A mass conservative and water storage consistent variable parameter Muskingum-Cunge approach. Hydrol. Earth Syst. Sci. 11, 1645–1659.

Toffoli, T., 1984. Cellular automata as an alternative to (rather than an approximation of) differential equations in modeling physics, Physica D, 10 (1-2), 117-127.

Von Neumann, J., 1966. Theory of self-reproduction automata, Univ of Ill. Press, Urbana.

Wagenbrenner, N.S., Forthofer, J.M., Lamb, B.K., Shannon, K.S., Butler, B.W., (2016) Downscaling surface wind predictions from numerical weather prediction models in complex terrain with WindNinja, Atmos. Chem. Phys., 16, 5229-5241, doi:10.5194/acp-16-5229-2016.

Wales-Smith, B. G. (1980). Estimates of net radiation for evaporation calculations, Hydrological Sciences Journal, 25:3, 237-242, DOI: 10.1080/02626668009491931

Wallinga J, van de Wal S W. 1998. Sensitivity of Rhonegletscher, Switzerland, to climate change: experiments with a one-dimensional flowline model. Journal of Glaciology 44: 383-393.

Webster, R., & Oliver, M. A. (2007). Geostatistics for environmental scientists John Wiley & Sons.

Zhang, Y., Chang, X. & Liang, J. Comparison of different algorithms for calculating the shading effects of topography on solar irradiance in a mountainous area. Environ Earth Sci 76, 295 (2017). https://doi.org/10.1007/s12665-017-6618-5

Zhao, L., Xia, J., Xu, Cy. et al. Evapotranspiration estimation methods in hydrological models. J. Geogr. Sci. 23, 359–369 (2013). https://doi.org/10.1007/s11442-013-1015-9

Zimmerman, D.L., Zimmerman, M.B., 1991. A comparison of spatial semivariogram estimators and corresponding ordinary kriging predictors. Technometrics 33 (1), 77±91.